

The mantle source of the 2.7 Ga Fe-rich Qullinaaraaluk Intrusion
(NE Superior Craton) inferred through long- and short-lived Sm-Nd
systematics

by

Sarah Mount

A thesis submitted to the Faculty of Graduate and Postdoctoral Affairs in
partial fulfillment of the requirements for the degree of Master of Science

in

Earth Sciences

Carleton University
Ottawa, Ontario

© 2022, Sarah Mount

Preface

The work presented in this thesis is my own, supervised by Hanika Rizo and Jonathan O'Neil, and was funded through their NSERC grants. A study on the Neoproterozoic ferropicrites, in which they were classified into subalkaline and alkaline ferropicrites, was previously performed by Dejan Milidragovic. A detailed petrological description of the Qullinaaraaluk intrusion, including the lithological divisions, was previously performed by Dejan Milidragovic. I was the lead investigator on this project, responsible for data collection, analysis, and interpretation. This included sample collection during fieldwork, sample preparation, major and trace element geochemical analyses, and the main focus of this thesis: the Sm-Nd isotopic analyses.

Abstract

To provide insight into the Fe-enriched mantle domains that may be the source of ferropicrites, we present a coupled ^{147}Sm - ^{143}Nd and ^{146}Sm - ^{142}Nd study of the Neoproterozoic Fe-enriched Qullinaaraaluk intrusion (NESP). An isochron yields an age of 2706 ± 29 Ma, which is interpreted to be the crystallization age of the intrusion. Accounting for the effects of crustal contamination, the initial $\epsilon^{143}\text{Nd}$ values range from -0.39 to +1.26. High-precision measurements of $^{142}\text{Nd}/^{144}\text{Nd}$ ratios yield an average $\mu^{142}\text{Nd}$ of -0.4 ± 5.5 , revealing no deviation from the terrestrial standard. The absence of $\mu^{142}\text{Nd}$ anomaly indicates that the Qullinaaraaluk mantle source does not have a Hadean-formed component. Time-integrated $^{147}\text{Sm}/^{144}\text{Nd}$ ratios between 0.1944-0.2012 suggest derivation from a mantle source more enriched than the present-day depleted mantle. Similarities between the initial $\epsilon^{143}\text{Nd}$ of the Qullinaaraaluk intrusion and Superior province ferropicrites indicates that their Fe-enriched mantle source may share a similar history.

Acknowledgements

This project would not have been possible without the guidance and support of my supervisor, Hanika Rizo. Thank you for your encouragement, for introducing me to all the early-earth mysteries that have yet to be solved, and for showing me just how fun and creative research can be.

It also would not have been possible without the help of my co-supervisor, Jonathan O'Neil. Thank you for your valuable input on the petrology of the Qullinaaraaluk intrusion, teaching me the many steps of Sm-Nd column chromatography, and for your expertise in the field.

Thanks to the Pituvik Landholding Corporation of Inukjuak, as obtaining the rocks studied in this thesis would not have been possible without their logistical support. Additionally, thanks to Hanika, Jon, and Victor for going the extra mile (or two or three) hiking with backpacks full of heavy rocks under a variety of weather conditions.

Thank you to Tim Mount at Carleton University for his assistance in the rock lab and his preparation of thin sections, to Lilianne Pagé at the University of Ottawa for the XRF major element analysis, to Nimal DeSilva and Smita Mohanty at the University of Ottawa for their help with the ICP-MS, and to Shuangquan Zhang at Carleton University for his encouragement in addition to his help with the TIMS.

This endeavor would have been a lot less fun without the members, past and present, of the Ottawa-Carleton Early Earth Research Group: Daniel Peters, Victor Garcia, Alex Rouleau, Dan Stepner, Andréane Mitchell Dupuis, Chris Sole, and Ayesha Landon-Browne. Thank you. Special thanks to Daniel and Victor for all their help in the clean room, for answering my silly questions, and to Daniel for reading an early draft of this thesis. I'd also like to thank the Department of Earth Sciences at Carleton University for their support during my time here, including my friends and fellow graduate students at Carleton University, my GRAESSOC co-president Sabrina Chan, and Sharon Carr for her advice and wisdom.

To my parents, grandparents, sisters, and Sam, thank you for everything. To my science friends outside of geology: thank you for getting it whenever I needed to talk about thesis stuff. To my non-science friends: thank you for getting it whenever I needed to *not* talk about thesis stuff. To Vicki Tschirhart and Eric Potter of the GSC, thank you for encouraging me to embark on this academic journey.

Finally, thank you to my wonderful, adorable, and entertaining feline roommates, Gilbert and Fred Cosmo. While your contributions did not make it into the thesis, despite the many attempts made by walking across the keyboard, your companionship was unparalleled.

Table of Contents

Preface	ii
Abstract	iii
Acknowledgements	iv
Table of Contents	v
List of Tables.....	vi
List of Figures.....	vii
List of Appendices.....	viii
Chapter 1: Introduction	1
1.1 Previous Studies of Ferropicrites	4
1.2 Geologic Setting	14
1.3 Sm-Nd Isotope Systematics	18
Chapter 2: Methods	24
2.1 Sample Collection	24
2.2 Petrographic Sample Preparation.....	25
2.3 Sample Powder Preparation.....	25
2.4 Major Element Analyses.....	25
2.5 Trace Element Analyses	26
2.6 ¹⁴⁷ Sm- ¹⁴³ Nd Isotope Analyses	28
2.7 Sample Preparation and Analysis for High Precision Nd Isotope Measurements	31
3.0 Results	35
3.1 Petrological and Major and Trace Element Results of the Qullinaaraaluk Intrusion.....	35
3.2 ¹⁴⁷ Sm- ¹⁴³ Nd Systematics	43
3.3 ¹⁴⁶ Sm- ¹⁴² Nd Systematics	45
4.0 Discussion	49
4.1 The ¹⁴⁷ Sm- ¹⁴³ Nd Age and Source Composition of the Qullinaaraaluk Intrusion.....	49
4.2 Constraints on the Mantle Source from the Short-lived ¹⁴⁶ Sm- ¹⁴² Nd System	55
4.3 The Source of Neoproterozoic Ferropicrites vs. Other Contemporaneous Mantle-derived Rocks	58
Chapter 5: Conclusion	64
References	67
Appendix A	73
Appendix B	84

List of Tables

Table 1: Faraday cup configuration for Nd isotope measurements.....	29
Table 2: Faraday cup configuration for Sm measurements.....	30
Table 3: Faraday cup configuration for dynamic $^{142}\text{Nd}/^{144}\text{Nd}$ measurements	32
Table 4: Summary of major and trace element data.....	42
Table 5: ^{147}Sm - ^{143}Nd analysis results.....	44
Table 6: ^{142}Nd Analysis Results.....	47
Table 7: Uncontaminated ϵNd_i and time integrated $^{147}\text{Sm}/^{144}\text{Nd}$	55

List of Figures

Figure 1.1: Illustration of mechanisms for forming an Fe-rich mantle source.....	2
Figure 1.2: Neoproterozoic ferropicrite occurrences.....	10
Figure 1.3: Geochemical differences between Neoproterozoic ferropicrites.....	11
Figure 1.4: Illustration of the formation of Neoproterozoic ferropicrites.....	13
Figure 1.5: Geological map of the Qullinaaraaluk intrusion.....	15
Figure 1.6: Evolution of the ^{147}Sm - ^{143}Nd system over time.....	19
Figure 1.7: Evolution of $^{143}\text{Nd}/^{144}\text{Nd}$ of a depleted and enriched reservoir.....	22
Figure 1.8: Decay of ^{146}Sm into ^{142}Nd over time.....	23
Figure 1.9: Evolution of the $\mu^{142}\text{Nd}$ of a depleted and enriched reservoir.....	24
Figure 2.1: $^{142}\text{Nd}/^{144}\text{Nd}$ ratios of JNdi-1 standards.....	34
Figure 3.1: Normative mineralogy classification diagrams.....	36
Figure 3.2: FeO_{TOT} wt% versus MgO wt%.....	37
Figure 3.3: TiO_2 wt% versus Al_2O_3 wt%.....	38
Figure 3.4: Trace elements concentrations normalized to primitive mantle	39
Figure 3.5: Rare earth element concentrations normalized to chondrites	39
Figure 3.6: Ni versus Cr concentrations	40
Figure 3.7: La/Gd versus Gd/Yb normalized to chondritic values.....	41
Figure 3.8: $^{147}\text{Sm}/^{144}\text{Nd}$ versus $^{143}\text{Nd}/^{144}\text{Nd}$ isochron.....	45
Figure 3.9: $\mu^{142}\text{Nd}$ results.....	48
Figure 4.1: $\epsilon^{143}\text{Nd}$ calculated at 2720 Ma versus $1/\text{Nd}$	51
Figure 4.2: $^{147}\text{Sm}/^{144}\text{Nd}$ versus $^{143}\text{Nd}/^{144}\text{Nd}$ isochron excluding gabbro-norites	52
Figure 4.3: $\mu^{142}\text{Nd}$ of Qullinaaraaluk intrusion and extraterrestrial material.....	58
Figure 4.4: Time integrated $^{147}\text{Sm}/^{144}\text{Nd}$ versus age	59
Figure 4.5: $\mu^{142}\text{Nd}$ of subalkaline and alkaline ferropicrites	61
Figure 4.6: Uncontaminated $\epsilon^{143}\text{Nd}$ of Qullinaaraaluk intrusion versus time	62

List of Appendices

Appendix A.....71
Appendix B.....82

Chapter 1: Introduction

The interior of our planet is dynamic; it has been changing and evolving since its formation. Over time, the extraction of a crust enriched in incompatible trace elements has depleted sections of the Earth's mantle, and so it is expected that the modern mantle is compositionally different from the Archean mantle. However, tracing this chemical evolution through time can be challenging as the evidence is recorded in mantle-derived rocks that are effectively recycled back into the mantle by plate tectonics. By studying available Archean mafic-ultramafic rocks, we can obtain direct information about the geochemical characteristics of the mantle at the time of the rocks' emplacement.

Ferropicrites are relatively rare iron (Fe-) and magnesium (Mg-) rich rocks. Interestingly, their Fe- and Mg- enrichment is difficult to explain by derivation from a pyrolytic mantle, resulting in the suggestion that they derive from an Fe-enriched mantle source (Hanski and Smolkin, 1989; Stone et al., 1995; Francis et al., 1999; Gibson et al., 2000; Jennings, 2016). The origin of this Fe-enriched mantle source remains debated, and a variety of models have been proposed. Examples of these models include: 1) the melting of a garnet-pyroxenite source created through the reaction between mantle peridotite and eclogitic material in mantle plumes (Figure 1.1a; Gibson, 2002; Tuff et al., 2005; Jennings, 2016), 2) derivation from an mantle domain formed from the incorporation of Fe-rich extraterrestrial material into the mantle (Figure 1.1b, Milidragovic and Francis, 2016), and 3) derivation from an Fe-rich mantle domain formed by silicate differentiation caused by the crystallization of a Hadean magma ocean (Figure 1.1c, Goldstein and Francis, 2008).

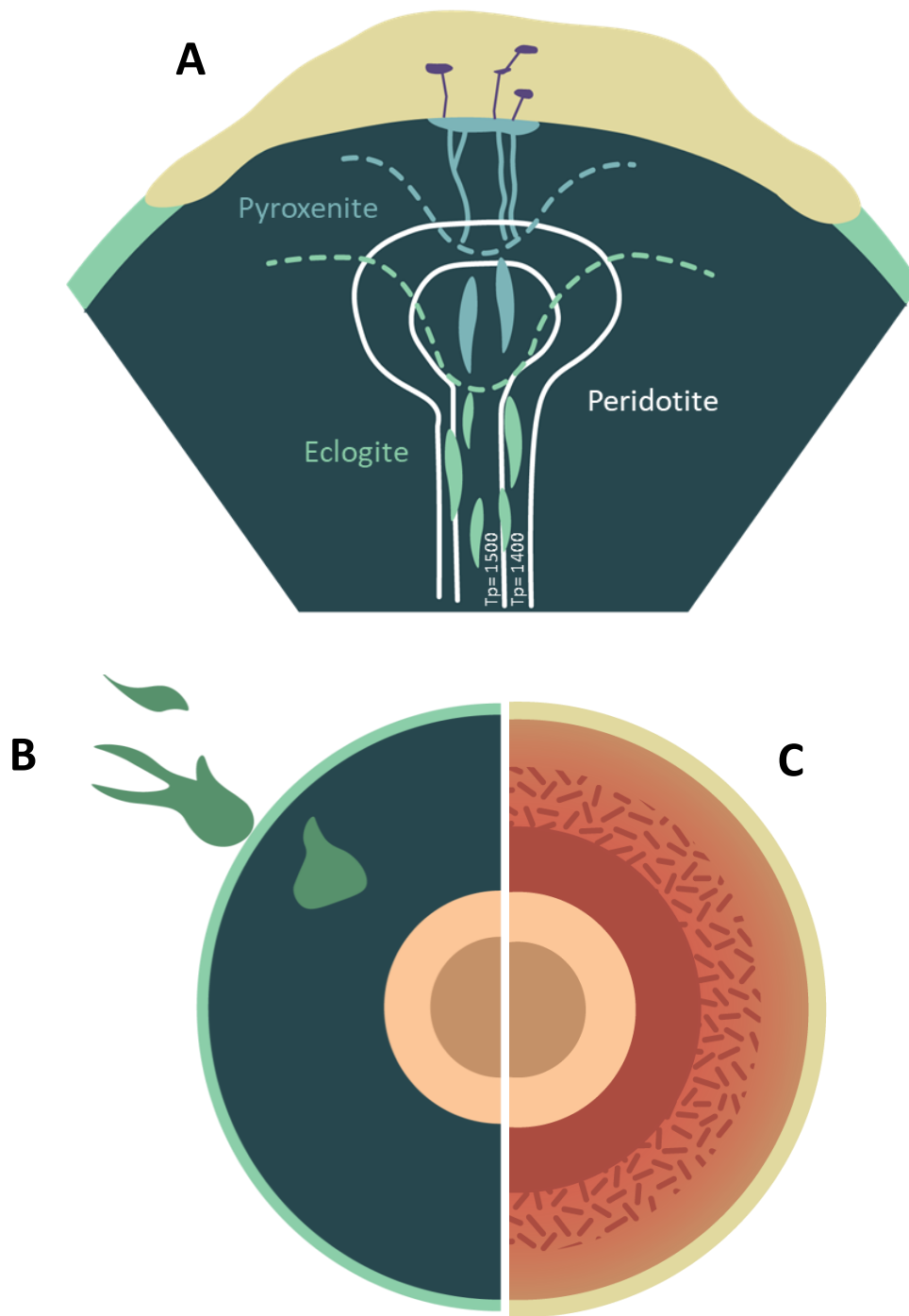


Figure 1.1: Illustrations of mechanisms for forming an Fe-rich mantle source, not to scale. In (a), eclogite converts peridotite to pyroxenite, which then melts to form the ferropicrites, after Jennings et al., 2016. In (b), Fe- rich extraterrestrial material is incorporated into the mantle, after ideas from Milidragovic and Francis, 2016. In (c), and Fe-rich source is formed during the crystallization of a Hadean magma ocean, after ideas from Goldstein and Francis, 2008.

Here we have studied Neoproterozoic ferropicrites from the Qullinaaraalik intrusion located in the North-Eastern Superior Province (NESP). We have combined the long-lived ^{147}Sm - ^{143}Nd system with the short-lived ^{146}Sm - ^{142}Nd system to investigate the intrusion's mantle source.

As Nd is more incompatible than Sm during igneous processes, the Sm/Nd of a source directly corresponds to its incompatible trace element enrichment. Because ^{147}Sm decays into ^{143}Nd , by determining the initial $^{143}\text{Nd}/^{144}\text{Nd}$ composition of a suite of rocks we can obtain information about the enrichment of the rocks' mantle source at the time of emplacement. Due to the half-life of 103 Ma of the short-lived ^{146}Sm - ^{142}Nd system, the parent (^{146}Sm) was only actively decaying into the daughter (^{142}Nd) during the first 500 Ma following our solar system's formation. Therefore, any deviations in ^{142}Nd from the terrestrial standard measured today reflect Sm/Nd fractionation that occurred while the system was active prior to 4.0 Ga.

Silicate fractionation events occurring in the Hadean, such as the solidification of a magma ocean, produce reservoirs with different Sm/Nd ratios which then evolve to $^{142}\text{Nd}/^{144}\text{Nd}$ compositions that differ from the terrestrial standard. If the mantle source of the ferropicrites formed after the solidification of a Hadean magma ocean (Goldstein and Francis, 2008), they will have $^{142}\text{Nd}/^{144}\text{Nd}$ compositions that differ from the terrestrial standard. Additionally, extraterrestrial material, such as shergottites, chondrites, and achondrites, have $^{142}\text{Nd}/^{144}\text{Nd}$ compositions that differ from that of the Earth (Borg et al., 2016; Boyet and Carlson, 2005; Burkhardt et al., 2016). Therefore, if the ferropicrite

mantle source includes extraterrestrial material (Milidragovic and Francis, 2016), this could be reflected in the $^{142}\text{Nd}/^{144}\text{Nd}$ compositions of the rocks.

We present the first high-precision long-lived ^{147}Sm - ^{143}Nd and short-lived ^{146}Sm - ^{142}Nd study on samples from the Qullinaaraaluk intrusion, providing the first direct chronological constraint for the intrusion's emplacement, and investigate the origin of its mantle source. We use these results to evaluate proposed petrogenesis models for ferropicrites and to explore the relationship between alkaline and subalkaline Neoproterozoic ferropicrites.

1.1 Previous Studies of Ferropicrites

1.11 Geochemical Characteristics and Petrogenesis Models of Ferropicrites

Ferropicrites are mantle-derived Fe-enriched picritic magmas, generally characterized by FeO_{TOT} (total Fe expressed as ferrous iron) contents higher than 14 wt.%, MgO contents between 12 and 19 wt.%, and low Al_2O_3 contents (~10%) relative to picrites. They are also characterized by Ti, Ni, high field strength elements (HFSE) and light rare earth element (LREE) enrichments, and usually have fractionated middle rare earth element (MREE) to heavy rare earth element (HREE) ratios ($[\text{Gd}/\text{Yb}]_{\text{PM}}$ between 1.7 and 3.5; Hanski and Smolkin, 1989; Stone et al., 1995; Gibson et al., 2002; Jennings et al., 2016; Milidragovic and Francis, 2016). Their $\epsilon^{143}\text{Nd}_i$ (Initial $^{143}\text{Nd}/^{144}\text{Nd}$ compositions normalized to the Chondritic Uniform Reservoir reference, CHUR, at the time of unit formation) values usually range between +1 and +4, suggesting they originate from an incompatible trace element depleted mantle source (Hanski et al., 1990; Stone et al., 1995; Francis et al., 1999; Gibson et al., 2000). Combined initial $\epsilon^{143}\text{Nd}$ and LREE enrichments suggest that the

source was enriched in trace elements shortly before emplacement (Hanski and Smolkin, 1995; Stone et al., 1995; Francis et al., 1999; Gibson et al., 2000). Initially, ferropicrites were only identified in the Archean, which lead Francis et al. (1999) to suggest that the Earth's mantle was originally more Fe-enriched and that its Fe-content decreased over time. This theory was subsequently challenged upon the discovery of younger ferropicrites. However, it has been noted that Archean ferropicrites are characterized by higher FeO_{TOT} contents than their younger counterparts (Gibson, 2002), which could be attributed to the higher mantle temperatures of the Archean (Herzberg et al., 2010). While occurrences of ferropicrites on Earth's surface are relatively rare, they have now been identified on every continent and range in age from the Archean to the Phanerozoic (Francis, 1999; Heinon and Luttinen, 2008; Gibson et al., 2000). Despite their differences in Fe- and Mg- contents, the trace element enrichments and HREE depletions observed in ferropicrites result in their frequent comparison to oceanic island basalts (OIBs). Archean ferropicrites are associated with greenstone belts, as demonstrated by occurrences in the Superior, Slave, Yilgarn, and Kaapvaal cratons (Goldstein and Francis, 2008; Kitayama and Francis, 2014; Milidragovic and Francis, 2016). Post-Archean ferropicrites tend to be associated with large igneous provinces and continental flood basalts (Gibson et al., 2000; Gibson, 2002; Heinonen and Luttinen, 2008; Jennings et al., 2016).

While ferropicrites share compositional similarities with Al-depleted komatiites, their unique geochemistry (e.g., higher $\text{FeO}_{\text{TOT}}/\text{Al}_2\text{O}_3$ at a given MgO, LREE and Ni enrichments) requires a different petrogenesis (Stone et al., 1995). Although it is generally accepted that ferropicritic magmas are produced by the partial melting of an Fe-rich

mantle source, the mechanism for the iron enrichment remains debated (Stone et al., 1995; Francis et al., 1999; Gibson et al., 2000; Kitayama and Francis, 2014; Milidragovic and Francis, 2016; Jennings 2016).

Melting of a fertile, Fe-rich lower mantle or lower mantle domain has been proposed as a source for ferropicrites (Hanski and Smolkin, 1995; Gibson et al., 2000; Francis et al., 1999). However, modelling of fertile mantle xenolith melting generates magmas that are too rich in Al_2O_3 at a given FeO_{TOT} content for Archean ferropicrites (Goldstein and Francis, 2008; Milidragovic et al., 2014). When studying Phanerozoic ferropicrites, Gibson et al. (2000) proposed that a lower mantle domain could become Fe-rich through core-mantle chemical interaction. While depletions of platinum group elements (PGE) of ferropicrites do not support a core-origin for the Fe-enrichments (Stone et al., 1995), estimating PGE contents in the source of partial melts is challenging and still the subject of active investigations (e.g., Waterton et al., 2021). Regardless, due to their density, Archean ferropicritic magmas must be produced at pressures lower than 5 GPa in order to be buoyant in the mantle (Goldstein and Francis, 2008, Milidragovic et al., 2016). Because rising under adiabatic decompression would generate melts at pressures above 5 GPa, where ferropicritic magmas would be negatively buoyant and sink, it is improbable for the Archean ferropicrite source to be a lower-mantle domain (Goldstein and Francis, 2008; Milidragovic et al., 2016).

Experimental data indicates that ferropicritic magmas cannot coexist with a mantle residue that contains both olivine and garnet (Hanski and Smolkin, 1995; Stone et al., 1995; Tuff et al., 2005). Based on these constraints, the ferropicrite source is proposed

to be either an Fe-enriched olivine-dominated peridotite or a garnet-pyroxenite. Hanski and Smolkin (1995) and Stone et al. (1995) suggested an Fe-rich peridotite source for the ferropicrites. However, given the ferropicrites' depletions in HREE, residual garnet is required in their magma's source. To accommodate the "garnet" signature, they proposed that the source of ferropicritic magmas is formed through a two-stage process. In the first stage, the peridotite is depleted through melt extractions, decreasing Al_2O_3 contents and increasing concentrations in compatible elements. In the second stage, this depleted mantle source is metasomatized by highly enriched small-degree melts that formed at depths at which garnet was stable. This results in enrichments in Fe, Ti, and highly incompatible elements, and produces the "garnet" signature with fractionated HREE. A variation of this mechanism is invoked by Goldstein and Francis (2008) to explain the ferropicrites of the Western Superior Province. Modelling of magma oceans has demonstrated that they are capable of creating Fe-rich mantle domains (Labrosse et al., 2007; Ballmer et al., 2017). Therefore, to obtain a garnet signature in a garnet-free peridotite, Goldstein and Francis (2008) proposed that the ferropicrite source was an Fe-rich peridotite formed from the crystallization of a Hadean magma ocean that had previously experienced garnet fractionation.

Garnet-pyroxenite models, first proposed by Gibson (2002), similarly employ a multi-stage process to create the Fe-rich magmas. In these models, partial melts of eclogite react with mantle peridotite to form a garnet-pyroxenite source (Gibson, 2002; Jennings, 2016). The eclogite would impart an enrichment in incompatible trace elements, and melting within the garnet-stability field accounts for the fractionated HREE

signature and low Al₂O₃ contents. This is supported by experiments by Yaxley and Green (1998), in which they show that partially melted eclogite enriches mantle peridotite to form a garnet-pyroxenite, and high-pressure supersolidus phase relations of a natural ferropicrite by Tuff et al. (2005) which suggested that the melt last equilibrated with a clinopyroxene and garnet source. However, it is noted that experiments fail to achieve high enough FeO_{TOT} at a given MgO (Goldstein and Francis, 2008, Ichiyama et al., 2006). Ichiyama et al. (2006) and Heinonen and Luttinen (2008) propose that recycling of an Fe-Ti gabbro would better explain the incompatible element and Fe-enrichment.

An alternative to the garnet-pyroxenite and Fe-peridotite models was proposed by Jakobsen et al. (2005). This model suggests that ferropicrites form from picritic magmas mixing with Fe-rich liquids produced by basaltic immiscibility (Jakobsen et al., 2005; Veksler et al., 2006). However, this mixing would not produce high enough MgO enrichment at a given FeO_{TOT}, and a complementary silicic magmatism is not observed in association with ferropicrites (Goldstein and Francis, 2008). Additionally, the temperature of ferropicritic magmas is hotter than the basalt miscibility gap (Tuff et al., 2005).

Recently, He et al. (2019) proposed that the FeO_{TOT} and MgO enrichment of ferropicrites can be generated by melting of peridotite or pyroxenite under high fO₂ conditions. They suggest these high fO₂ environments can be created by sedimentary carbonate recycling. However, not all ferropicrites seem to have been produced under oxidizing conditions, and the scarcity of carbonate rocks during the Archean suggests this model could be implausible for older ferropicrites (Milidragovic et al., 2014; Cameron and Baumann, 1972).

1.12 Neoproterozoic Ferropicrites

Neoproterozoic ferropicrites have been identified in Canada within the Superior Province (Green and Schulz, 1977; Schulz, 1982; Stone et al., 1995; Goldstein and Francis, 2008; Kitayama and Francis, 2014, Milidragovic et al., 2014), the Slave Province, and the West Churchill Province, in Western Australia's Yilgarn Craton, in South Africa's Kaapvaal Craton, and in Southeast Finland's Karelia Craton (Milidragovic et al., 2016; Figure 1.2).

Their abundance in the Neoproterozoic relative to later occurrences has been associated with the proposed thermal mantle maximum at the Archean-Proterozoic boundary and late Archean "Superevent" (Herzberg and al., 2010, Van Kranendonk et al., 2012). Such events would be marked by large volumes of mantle melting and subsequent continental growth, possibly exhausting the ferropicritic mantle source and resulting in fewer ferropicrite occurrences post-Archean. The underplating of the NESP by ferropicritic melts is considered by Milidragovic et al. (2014) to be a key event of the province's cratonization.

Milidragovic and Francis (2016) proposed to divide Neoproterozoic ferropicrites into alkaline and subalkaline suites based on their geochemical characteristics. The alkaline suite is geochemically similar to the ferropicrites described by previous studies (referred to here as "traditional" ferropicrites, described in Section 1.11), with trace element profiles that resemble modern OIB and Ti, HFSE, and Ni enrichments.

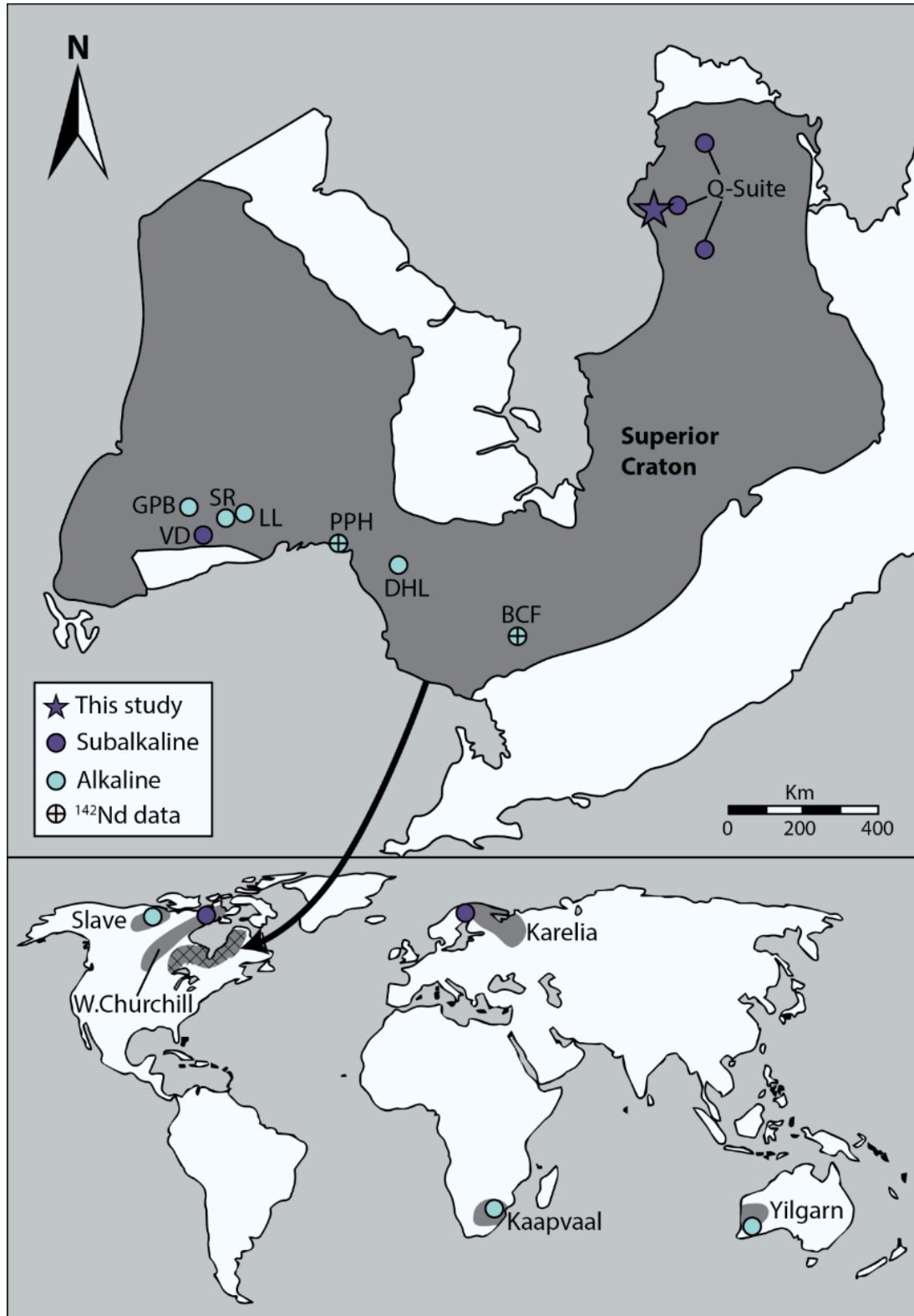


Figure 1.2: Neoproterozoic ferropicrite occurrences, after Milidragovic et al., 2016. Stars indicate intrusions that have previously been studied using the short-lived ^{146}Sm - ^{142}Nd system. Dark areas indicate Archean cratons, cross hatching shows location of upper map.

Conversely, the subalkaline suite does not resemble traditional ferropicrites. They have flat trace element profiles comparable to modern mid-oceanic ridge basalts (MORB), show depletions in Ti, HFSE, and Ni, and have higher Al_2O_3 contents than the alkaline suite. Despite the differences in major and trace element compositions between alkaline and subalkaline ferropicrites, the high Fe- and Mg-content of both suites ($\text{FeO}_{\text{TOT}} > 14\%$, $\text{MgO} > 11\%$) requires derivation from Fe-enriched mantle sources (Milidragovic et al., 2016).

The Ni-enrichment, fractionated HREE profiles, and Al_2O_3 depletion of the alkaline ferropicrites suggest they were derived from a garnet-pyroxenite source, while the Ni-depletion, flat HREE profile, and lack of Al_2O_3 depletion of the subalkaline ferropicrites suggest they were derived from an olivine-dominated peridotite source. This is further supported by low Sc/Fe in the alkaline ferropicrites and high Sc/Fe in the subalkaline ferropicrites, as Sc is compatible in garnet but incompatible in olivine (Figure 1.3; Milidragovic et al., 2016 and references therein).

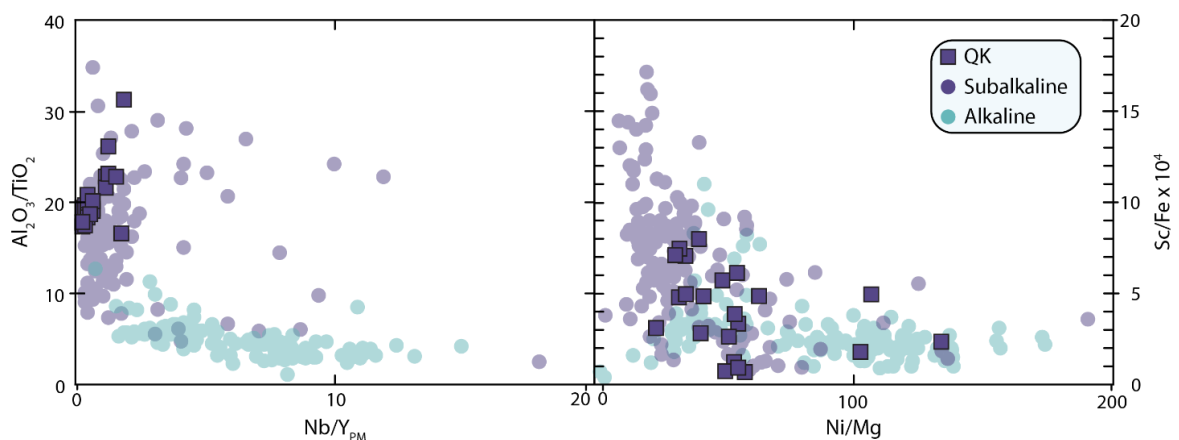


Figure 1.3: Key geochemical differences between Neoarchean subalkaline and alkaline ferropicrites. Squares are data obtained from this study. Circles represent data from Milidragovic and Francis, 2016.

As most models (described in detail in section 1.11) were developed to explain the trace element enrichment and HREE depletions observed in traditional and alkaline ferropicrites, Milidragovic and Francis (2016) find these models unsatisfactory to explain the subalkaline ferropicrites' geochemistry. Sources that do not necessitate the presence of residual garnet, such as Fe-rich "streaks" created by mantle plumes sampling Fe-enriched domains in the lower mantle (Gibson et al., 2000), do not seem to yield magmas with high enough FeO_{TOT} and MgO contents as modelled by melting of Fe-rich peridotite terrestrial xenoliths (Goldstein and Francis, 2008; Milidragovic et al., 2014). In addition, xenoliths with adequately low Mg# (0.78-0.81) have yet to be observed on Earth, and it is unlikely that an adequately FeO_{TOT} and MgO enriched melt from a deep mantle source could become buoyant in the Archean mantle (Milidragovic et al., 2014, Milidragovic and Francis, 2016; Goldstein and Francis, 2008).

Similarities between FeO_{TOT} , MgO, and Al_2O_3 contents of the subalkaline parental magmas and those of L5 ordinary chondrites, the Martian mantle, and the 4 Vesta asteroid lead Milidragovic and Francis (2016) to suggest that the mantle source of Neoproterozoic subalkaline ferropicrites formed from the late-accretion of chondritic or achondritic material. This material would form an Fe-enriched peridotitic domain in the upper mantle that would subsequently melt to produce the subalkaline ferropicrite magmas. While the metasomatism of mantle peridotite by eclogite (Gibson, 2002; Tuff et al., 2005; Jennings, 2016) does not generate high enough FeO_{TOT} at a given MgO to create Archean, the metasomatism of an Fe-enriched peridotite would create a garnet-

pyroxenite capable of producing the Ni-enrichments, HREE fractionations, and Fe- and Mg-enrichments of the alkaline ferropicrites (Figure 1.4; Milidragovic and Francis, 2016).

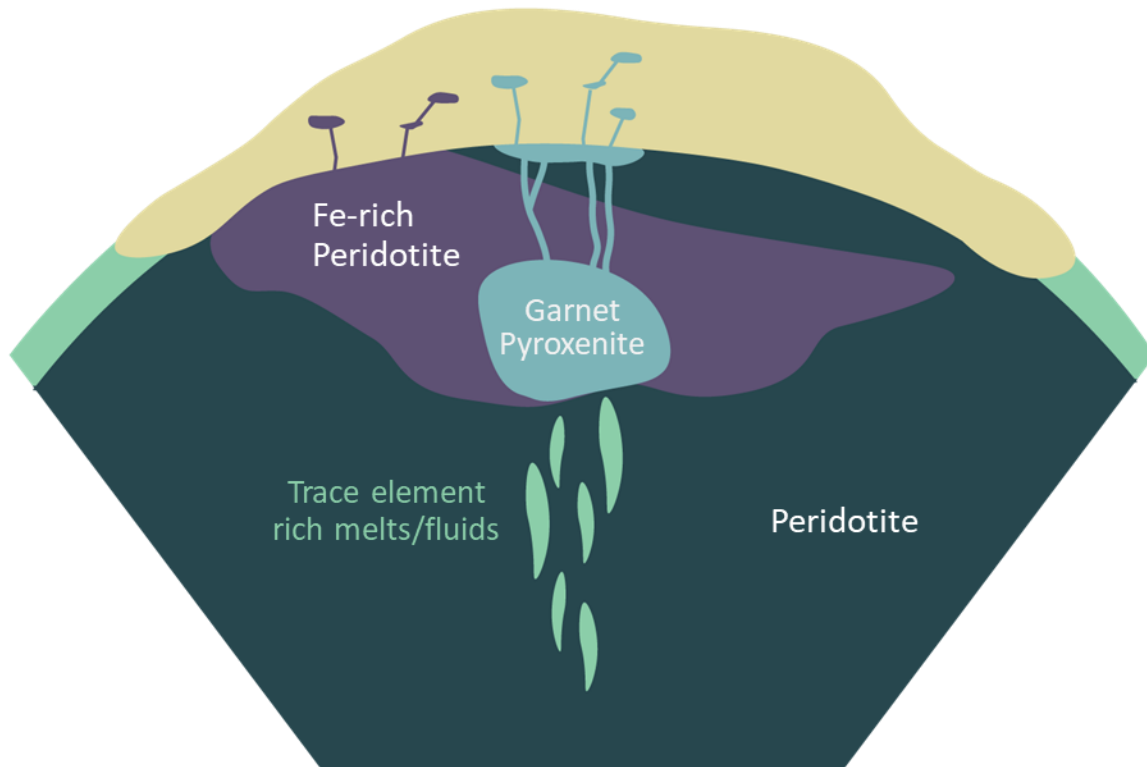


Figure 1.4: Illustration of formation of Neoproterozoic ferropicrites as proposed by Milidragovic and Francis, 2016. Blue indicates alkaline ferropicrites, purple indicates subalkaline ferropicrites. Not to scale.

Radiogenic isotope geochemistry has also been used to characterize the source of Neoproterozoic ferropicrite magmas. Alkaline ferropicrites from the southern Superior Province have $\epsilon^{176}\text{Hf} +4.2 \pm 0.9$ (Puchtel et al., 2018) and positive $\epsilon^{143}\text{Nd}$ ($\epsilon^{143}\text{Nd} = +2.5$, Stone et al., 1995; $\epsilon^{143}\text{Nd} = +2.5$, Puchtel et al., 2018; $\epsilon^{143}\text{Nd} = +2.3$, Landon-Browne, 2019), suggesting derivation from a depleted mantle source. Short-lived ^{146}Sm - ^{142}Nd and ^{182}Hf - ^{182}W investigations suggest the source of alkaline ferropicrites was characterized by slightly negative but unresolvable $\mu^{142}\text{Nd}$ anomalies (average $\mu^{142}\text{Nd} = -2.0 \pm 3.9$, Landon-

Browne, 2019; -3.8 ± 2.8 , Puchtel et al., 2018) and positive ^{182}W anomalies compared to the modern mantle. The subalkaline ferropicrites were also studied for Lu-Hf and Sm-Nd systems (Milidragovic et al., 2014) and their initial $\epsilon^{176}\text{Hf}$ resulted in variable values ranging from -6 to +6 and initial $\epsilon^{143}\text{Nd}$ ranging from -10 to +2. These analyses, however, were performed in samples that had experienced crustal contamination and are interpreted to reflect the isotopic composition of the crust rather than the mantle source of the ferropicrites (Milidragovic et al., 2014).

1.2 Geologic Setting

The Qullinaaraaluk intrusion (Figure 1.5) is a differentiated mafic to ultramafic body belonging to the Q-Suite group of Fe-enriched plutons located in northwestern Quebec, Canada. The intrusion was emplaced into ~ 2.75 Ga granitoids of the Hudson Bay Terrane of the NESP (Gosselin et al., 2002). Its exact time of emplacement is unknown, but is estimated to be between 2.72 Ga and 2.70 Ga, through U-Pb dating of zircons from gabbro-norites of contemporaneous Q-Suite intrusions (2707 ± 1 Ma, 2705 ± 1 Ma, Simard, 2008; 2718.9 ± 0.7 Ma and 2710.0 ± 0.5 Ma, Milidragovic and Francis, 2014) and U-Pb dating of a zircon in pegmatite cross-cutting a Q-Suite intrusion (2720 ± 2 Ma, Simard, 2008).

The Qullinaaraaluk intrusion is brecciated by decimeter-scale felsic veins and dykes, and while it has experienced alteration, the cumulate textures and primary mineralogy are relatively well preserved. The intrusion's core is composed of peridotite and harzburgite surrounded by a "shell" of websterite, with an outer border of

gabbronorite. The peridotite contains serpentinized olivine with oikocrysts of amphibole ± clinopyroxene.

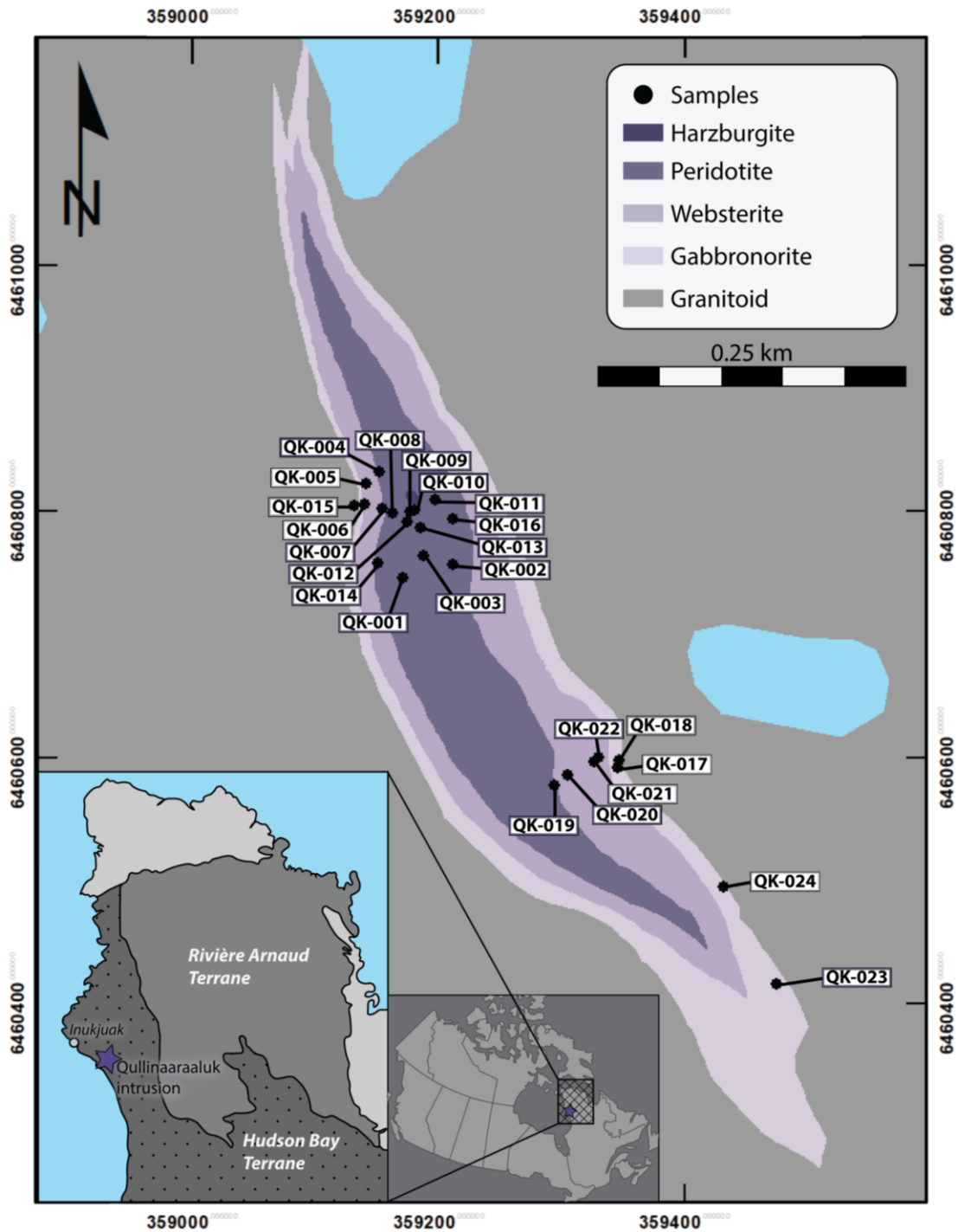


Figure 1.5: Geological map of the Qullinaaraaluk intrusion after Milidragovic et al. (2014), showing the sample locations for this study.

The websterites contain orthopyroxene and clinopyroxene with variable interstitial amphibole, biotite, and plagioclase. The amphibole is interpreted to be the product of a reaction with hydrous differentiated interstitial melt, as it is found as partial pseudomorphs of clinopyroxene (Milidragovic et al., 2014). The gabbronorites contain orthopyroxene, clinopyroxene, and plagioclase, with interstitial amphibole and biotite. The crystallization sequence proposed by Milidragovic et al. (2014) is olivine + Cr-spinel, orthopyroxene, clinopyroxene, amphibole, and plagioclase.

The Qullinaaraaluk intrusion studied here is one of several Fe-enriched mafic-ultramafic intrusions identified in the NESP and referred to as the Q-suite in Milidragovic et al. (2014). The Q-Suite is characterized by LREE enrichments, HFSE depletions, low Ni contents, and negative to chondritic initial $\epsilon^{143}\text{Nd}$ (initial $\epsilon^{143}\text{Nd} = -10$ to $+2$; Milidragovic et al., 2014). Q-Suite intrusions in the older Hudson Bay Terrane (> 2.88 Ga) have more negative $\epsilon^{143}\text{Nd}$ ($\epsilon^{143}\text{Nd} = -10$ to $+1$) than intrusions in the younger Rivière-Arnaud Terrane (< 2.88 Ga, $\epsilon^{143}\text{Nd} = -1$ to $+2$; Boily et al., 2009; Faure et al., 2008). The initial $\epsilon^{143}\text{Nd}$ that reflect the terrane in which the intrusions were emplaced, along with the enrichments in LREE and depletions in HFSE, are attributed to the simultaneous assimilation and fractional crystallization of granitoid crust during emplacement coupled with post-crystallization metasomatic contamination by anatectic felsic melts (Milidragovic et al., 2014). As such, the “calc-alkaline” signature of the Q-Suite is interpreted to be created by granitoid contamination rather than an arc setting. Contrary to Neoproterozoic alkaline ferropicrites, the Qullinaaraaluk intrusion lacks HREE depletions. Given the low abundance of HREE in the granitoids, crustal contamination would be ineffective in

modifying the HREE contents of the Qullinaaraaluk intrusion. Therefore, the lack of HREE depletion of the intrusion reflects the absence of residual garnet in the source, rather than HREE contamination by felsic magmas (Milidragovic et al., 2014). There is an absence of chilled margins between the Q-Suite intrusions and the granitoid crust, and some of the Q-Suite intrusions are flanked by pyroxene granitoids interpreted to be a mix between the Q-Suite parental magma and the granitoid crust (Milidragovic and Francis, 2014). This suggests the Q-Suite intrusions are coeval with the granitoids that surround them.

Reconstruction of the parental magma of the Q-suite by Milidragovic et al. (2014), based on harzburgite compositions, suggests a flat to depleted LREE profile, with flat HREE. The parental magma of the Qullinaaraaluk intrusion would have been an Fe- and Mg- enriched basalt (FeO ~ 14 wt%, MgO ~ 11 wt%), saturated in olivine, Cr-spinel, and orthopyroxene, with a lower Mg# (≥ 0.79) than most modern mantle-derived magmas (Milidragovic et al., 2014). Similarities between the major element composition of the subalkaline Q-Suite parental magmas and NESP Fe-tholeiites suggest they may be genetically related (Maurice et al., 2009; Milidragovic et al., 2014). The high MgO and FeO_{TOT} contents of the estimated parental magma cannot be generated through the melting of a pyrolitic mantle, and therefore require an Fe-enriched mantle source. The source is proposed to be an Fe-rich peridotite (Milidragovic et al., 2014; Milidragovic and Francis, 2016).

Twenty-four rocks were sampled from the least weathered outcrops of the Qullinaaraaluk intrusion. The samples were studied in thin section to determine their petrology and analyzed for major and trace elements. A selection of 15 samples were

analyzed for the long-lived Sm-Nd system, and 13 samples were analyzed for high precision ^{142}Nd isotope compositions. Constraining the source of the subalkaline ferropicrites using coupled ^{147}Sm - ^{143}Nd and ^{146}Sm - ^{142}Nd systems will help clarify the relationship between the sources of alkaline and subalkaline ferropicrites, as well as the origin of Fe-enriched peridotite in the Archean mantle.

1.3 Sm-Nd Isotope Systematics

This thesis employs the use of the Sm-Nd isotope systems, in which the parent (Sm) decays into the daughter (Nd) at a known rate. Two Sm-Nd isotope systems were used here: the long-lived system, in which ^{147}Sm decays into ^{143}Nd with a half-life of 106 Ga, and the short-lived system, in which ^{146}Sm decays into ^{142}Nd with a half-life of 103 Ma.

1.31 Long-lived ^{147}Sm - ^{143}Nd Radiogenic Isotope System and the Isochron Age Dating Method

The long-lived radiogenic Sm-Nd isotope system was applied to the study of ferropicrite magmas, to 1) constrain their age, and 2) to characterize the Nd isotope composition of their source.

Using radioactive decay law, the age of crystallization of a suite of cogenetic rocks or minerals within a single rock can be determined by plotting the present-day daughter (^{143}Nd , normalized to stable isotope ^{144}Nd) against the parent (^{147}Sm , normalized to ^{144}Nd) and taking the best-fit line through the data points, termed an isochron (Equation 1.1, Figure 1.6). As the slope of the isochron is equal to $e^{\lambda t}-1$, the age of crystallization can be determined by rearranging the equation to solve for t . Initial isotopic composition,

determined by the intercept of the isochron, can be used to infer information about the source of the dated suite.

$$(1.1) \quad \left(\frac{^{143}\text{Nd}}{^{144}\text{Nd}}\right) = \left(\frac{^{143}\text{Nd}}{^{144}\text{Nd}}\right)_{t=0} + \left(\frac{^{147}\text{Sm}}{^{144}\text{Nd}}\right) (e^{\lambda t} - 1)$$

Where $(^{143}\text{Nd}/^{144}\text{Nd})$ is the $^{143}\text{Nd}/^{144}\text{Nd}$ measured today, $(^{143}\text{Nd}/^{144}\text{Nd})_{t=0}$ is the $^{143}\text{Nd}/^{144}\text{Nd}$ at the time of crystallization, $(^{147}\text{Sm}/^{144}\text{Nd})$ is the $^{147}\text{Sm}/^{144}\text{Nd}$ measured today, t is the time between crystallization and the present, and λ is the ^{147}Sm decay constant ($\lambda = 6.524 \times 10^{-12}$ per year $^{-1}$).

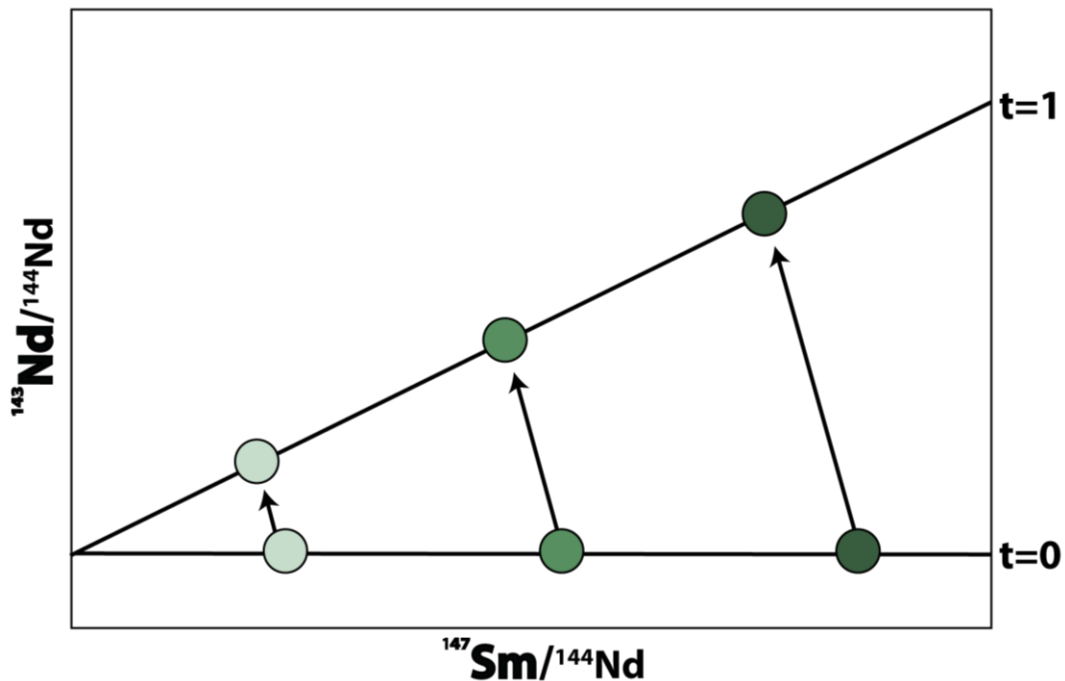


Figure 1.6: Evolution of the ^{147}Sm - ^{143}Nd system over time, with $t=0$ being the time of crystallization and $t=1$ being the time of measurement. At $t=0$, all samples have the same initial $^{143}\text{Nd}/^{144}\text{Nd}$ ratios.

The isochron age dating method can provide meaningful chronological constraints under the conditions that the isotopic system remained closed since crystallization and the rock suite analyzed had the same initial isotopic composition at the time of crystallization, meaning the rocks are cogenetic and derive from the same source. If one of these conditions is not met (e.g., the system has been reopened due to metamorphism

and there is a loss or gain of parent or daughter isotopes, or the rocks being analyzed represent mixing between two sources), the slope of the isochron will not represent the age of crystallization.

The dispersion of data along the best-fit line in an isochron diagram is described by the mean squared weighted deviation (MSWD). Some scatter along the best-fit line in an isochron diagram is expected and partially due to analytical errors during measurements. Isochron ages with $MSWD > 1$ usually reflect an over-dispersion of the data that cannot be explained by analytical uncertainty alone and could reflect either disturbances of the isotope system or that the samples studied are not truly cogenetic.

Samarium and Nd are both rare earth elements (REE). They are incompatible, lithophile elements, and immobile relative to other lithophile elements. Due to their incompatibility, they are relatively concentrated in crustal rocks, making them ideal candidates for studying mantle and crustal processes. However, their similar geochemical properties result in similar behaviour in geologic systems. This causes limited fractionation between Sm and Nd and can result in an imprecise isochron. Therefore, having a chemically differentiated intrusion, such as the Qullinaaraaluk intrusion, results in a more accurate age when using the ^{147}Sm - ^{143}Nd system. Additionally, due to its immobility and relatively long half-life, the ^{147}Sm - ^{143}Nd system is useful to age date ancient rocks. Its high closure temperature of 600-650°C makes the Sm-Nd system more reliable when dating metamorphosed rocks compared to other isotopic systems (e.g., Rb-Sr).

Given that Nd is more incompatible than Sm during igneous processes, the Sm/Nd composition of the source corresponds directly to its incompatible trace element enrichment. Therefore, the initial $^{143}\text{Nd}/^{144}\text{Nd}$ composition of the rocks can be combined with the isochron age to obtain information about the suite's source. This can be done by comparing the initial $^{143}\text{Nd}/^{144}\text{Nd}$ composition to that of the CHUR (DePaolo and Wasserburg, 1976) using the equation:

$$(1.2) \quad \varepsilon^{143}\text{Nd}_{(t)} = \left[\frac{\left(\frac{^{143}\text{Nd}}{^{144}\text{Nd}}\right)_{\text{sample}} - \left(\frac{^{143}\text{Nd}}{^{144}\text{Nd}}\right)_{\text{CHUR}}}{\left(\frac{^{143}\text{Nd}}{^{144}\text{Nd}}\right)_{\text{CHUR}}} \right] \times 10^4$$

Where t is the time between the sample's crystallization and the present.

The composition of the CHUR is used as the composition of the bulk silicate earth, from which all geochemical reservoirs have evolved. Negative $\varepsilon^{143}\text{Nd}$ values reflect a source that evolved with a subchondritic Sm/Nd ratio and corresponding enrichments in incompatible trace elements, while positive $\varepsilon^{143}\text{Nd}$ values reflect a source that evolved with a superchondritic Sm/Nd ratio and corresponding depletions in incompatible trace elements (Figure 1.7).

Other methods of characterizing the sources of rocks include calculating the model age of a sample, which uses equation (1.3) to determine the age at which the Sm/Nd composition of the rocks was the same as the depleted mantle:

$$(1.3) \quad T_{DM} = \frac{1}{\lambda} \ln \left(\frac{\left(\frac{^{143}\text{Nd}}{^{144}\text{Nd}}\right)_{DM} - \left(\frac{^{143}\text{Nd}}{^{144}\text{Nd}}\right)_{\text{Sample}}}{\left(\frac{^{147}\text{Sm}}{^{144}\text{Nd}}\right)_{DM} - \left(\frac{^{147}\text{Sm}}{^{144}\text{Nd}}\right)_{\text{Sample}}} + 1 \right)$$

Where T_{DM} is the model age and λ is the ^{147}Sm decay constant.

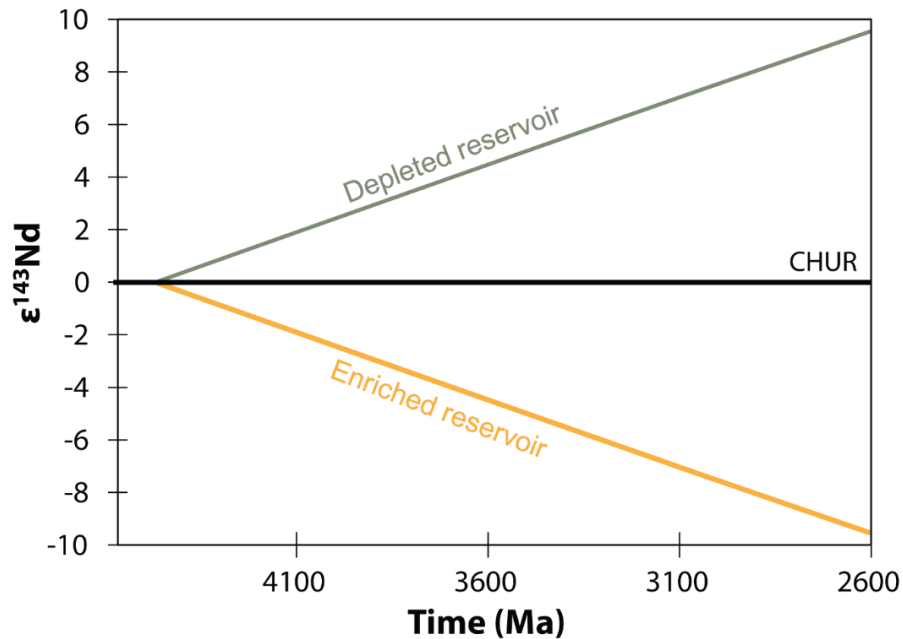


Figure 1.7: Example of evolution through time of the $\epsilon^{143}\text{Nd}$ of an incompatible trace element depleted and enriched reservoirs differentiated at 4.4 Ga.

The evolution of a source over time can also be described by its time-integrated $^{147}\text{Sm}/^{144}\text{Nd}$ ratio. This is determined using the initial $^{143}\text{Nd}/^{144}\text{Nd}$ of a source and assuming separation from CHUR at the start of the solar system 4568 Ma ago. Time-integrated $^{147}\text{Sm}/^{144}\text{Nd}$ provide information on the minimum degree of incompatible trace element enrichments or depletions of a reservoir compared to the CHUR evolution.

1.32 Short-Lived ^{146}Sm - ^{142}Nd Isotopic System

Isotopic systems are considered extinct after approximately 5 half-lives. Because the half-life of the ^{146}Sm - ^{142}Nd system is 103 Ma, it is considered extinct ~500 Ma after solar system formation (i.e., at 4.1 Ga; Figure 1.8). While the system cannot be used to age-date rocks younger than 4.1 Ga, it has proved to be a powerful tool to identify silicate differentiation during the Hadean. Resolvable variations in $^{142}\text{Nd}/^{144}\text{Nd}$ measured today must have been created by Sm/Nd fractionation and the decay of ^{146}Sm while the system

was extant (Figure 1.9). Variations in $^{142}\text{Nd}/^{144}\text{Nd}$ could also be imparted by the mixing of younger material with a Hadean-formed component (O'Neil and Carlson, 2017).

Measurements of $^{142}\text{Nd}/^{144}\text{Nd}$ are typically reported in $\mu^{142}\text{Nd}$ notation, which reflects part per million (ppm) deviations of a sample from the Nd terrestrial standard JNdi-1 (Tanaka et al., 2000):

$$(1.4) \quad \mu^{142}\text{Nd} = \left[\frac{\left(\frac{^{142}\text{Nd}}{^{144}\text{Nd}}\right)^{\text{sample}} - \left(\frac{^{142}\text{Nd}}{^{144}\text{Nd}}\right)^{\text{standard}}}{\left(\frac{^{142}\text{Nd}}{^{144}\text{Nd}}\right)^{\text{standard}}} \right] \times 10^6$$

Depleted reservoirs created in the Hadean will be characterized by positive $\mu^{142}\text{Nd}$, and enriched reservoirs created in the Hadean will be characterized by negative $\mu^{142}\text{Nd}$. This system is useful for constraining the source of ferropicrites, as models involving sources created from extraterrestrial material or from the crystallization of a Hadean magma ocean should exhibit variations in $\mu^{142}\text{Nd}$.

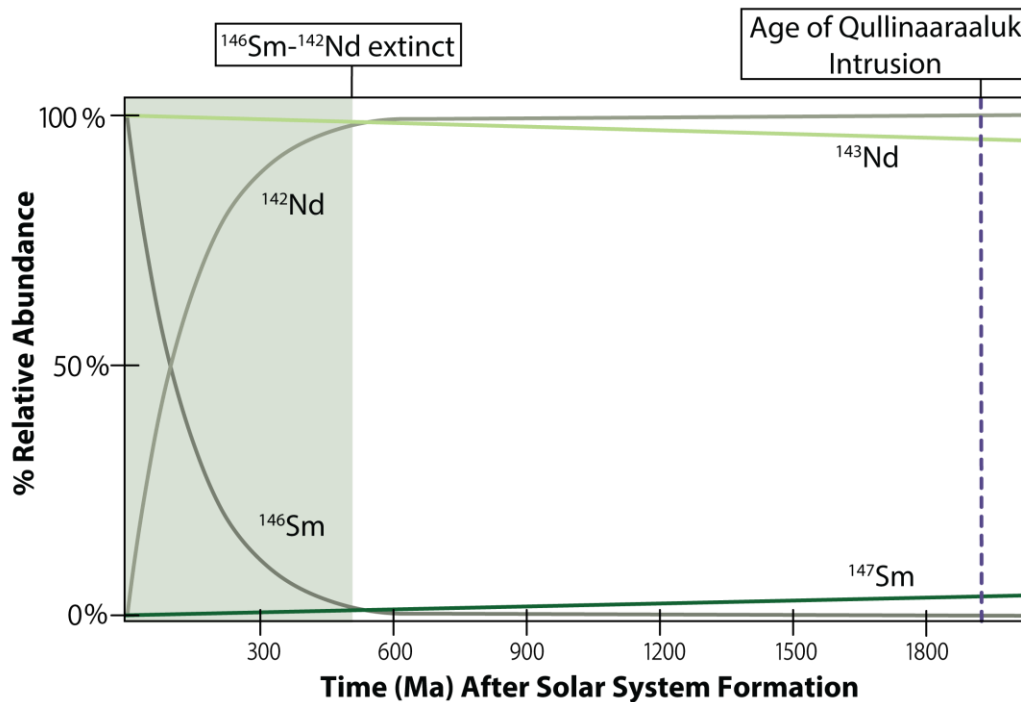


Figure 1.8: Decay of ^{146}Sm into ^{142}Nd compared to decay of ^{147}Sm into ^{143}Nd over time.

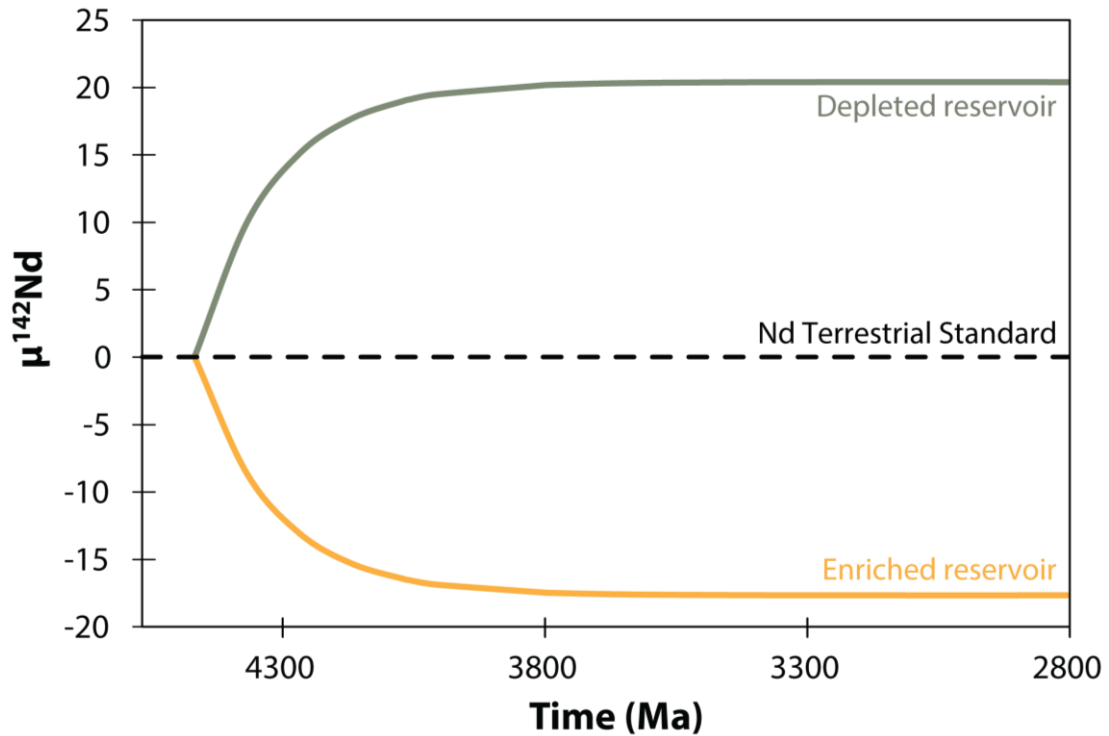


Figure 1.9: Example of the evolution through time of the $\mu^{142}\text{Nd}$ of incompatible trace element depleted and enriched reservoirs created at 4.4 Ga.

Chapter 2: Methods

2.1 Sample Collection

Rocks from the Qullinaaraaluk intrusion were sampled during in the summer of 2019. Sample collection was limited to the outcropping sections of the intrusion as it is partially covered by brush and swamp. Twenty-two samples representative of the different lithologies (harzburgite, peridotite, websterite, and gabbro-norite) in the differentiated intrusion were collected. Additionally, two samples were collected from the granitoid rocks hosting the intrusion to allow for evaluation of crustal contamination. Rocks that were close to crosscutting felsic veins or visibly weathered/altered were avoided. Sample locations of rocks collected are shown in Figure 1.5, and their GPS coordinates can be found in Appendix A, Table A1.

2.2 Petrographic Sample Preparation

Samples were prepared in Carleton University's Rock Preparation Laboratory. Rocks were cut into slabs representative of their dominant lithology and prepared as thin sections. The thin sections were examined under a transmitted light microscope to determine their mineralogy and the extent of weathering/alteration.

2.3 Sample Powder Preparation

Whole-rock powders were prepared in Carleton University's Rock Preparation Laboratory. Samples were cut into slabs using a diamond bladed rock saw, removing visible weathering and alteration. Potential metal contamination from the saw was removed by sanding the rock slabs with silicon carbide, first using a metal wheel lap and then by hand. The slabs were then cleaned in an ultrasonic bath for 15 minutes. Once dried, they were wrapped in plastic bags and broken into ~1cm pieces using a plastic hammer. The pieces were then processed through a ceramic jaw crusher, which was disassembled and thoroughly cleaned and dried between each sample. For each run, a small amount of crushed sample was used to pre-contaminate the ceramic jaws and discarded. The crushed sample was powdered in an agate ring mill. The ring mill was thoroughly cleaned between each sample and pre-contaminated with a small amount of sample before the actual run.

2.4 Major Element Analyses

The major element oxides were analysed for all 24 samples using x-ray fluorescence (XRF) spectroscopy at the X-Ray Core Facility of the University of Ottawa, Canada. The loss on ignition (LOI) content of each sample was measured by heating a known mass of sample

powder in an oven at 1070°C for 1 hour. The samples were cooled and their post-heating mass was recorded, with the difference between the masses taken as the sample's LOI. For XRF analysis, ~0.8 g of sample powder was combined with 7.2 g of 79/21 Li₂B₄O₇ (LiBO₄ flux and 1% LiBr non-wetting agent) to achieve a 1:9 ratio of sample to flux. This mixture was fused into glass discs and analyzed by a Rigaku Supermini200WDXRF spectrometer. Sample calibration curves were constructed using the geological reference materials UB-N, UM-2, MRG-1, PM-S, BCR-2, WS-E, SY-3, BHVO-2, BM, AN-G, BCR-032 and PC1016. United States Geological Survey (USGS) rock standards BHVO-2 (basalt) and GSP-2 (granodiorite) were analyzed to monitor the accuracy of the analysis for mafic and felsic samples, respectively. Major element oxides of mafic and ultramafic samples were measured with an accuracy between 0.01 wt% and 4.55 wt% (Appendix A, Table A2). Apart from TiO₂, all other major elements in the felsic rocks were measured with an accuracy between 0.06% and 2.66% (Appendix A, Table A3). The reproducibility of measurements was obtained by repeated measurement of the BHVO-2 standard, which resulted in a 2SE ≤ 0.12 wt% for all major elements (Appendix A, Table A2).

2.5 Trace Element Analyses

All 24 samples were prepared for trace element analyses at the Geochemistry Core Facility of the University of Ottawa. Sample dissolution was performed in a clean laboratory. Along with the 24 collected samples, four USGS geological reference materials, BHVO-2, BCR-2, BIR-1, and GSP-2, were dissolved and analyzed. For each sample, ~0.1 g of powder was dissolved in 1 mL of concentrated HNO₃ and 4 mL of concentrated HF. For mafic and ultramafic samples, dissolution was achieved in Savillex

Teflon beakers, sealed and heated to 120 °C for three days. The beakers were then left open at 85 °C until samples were dry. The samples were then re-dissolved in 8 mL of 6N HCl with a few drops of H₂BO₃ to fully dissolve fluorides. Beakers were sealed and heated to 120 °C for two days. Samples were dried again at 85 °C, dissolved in 5 mL of 7N HNO₃, and dried once more. The same dissolution method was followed for felsic samples, but achieved in steel jacket high-pressure Parr bombs heated to 140 °C in an oven. This guaranteed complete dissolution of refractory phases.

The day before ICP-MS analysis, samples were dissolved in 40 mL of 7N HNO₃ and heated to 125 °C overnight. The day of analysis, a 1 mL aliquot of the solution was combined with 11 mL of 0.5N HNO₃ with traces of HF, achieving a dilution factor of ~4000. The traces of HF prevent certain elements, such as the HFSE, from precipitating out of the solution. All solutions were spiked with 2 ppb of Indium (In), which was used to monitor plasma, intake flow instabilities, and element fractionation during the analysis.

The measurements were performed on an Agilent 8800 Triple Quadrupole ICP-MS at the University of Ottawa. The samples and geological reference materials were corrected for background noise by subtracting the average counts per second measured for the reagent blank. The standard BHVO-2 was used as the internal calibration material, while BCR-2, BIR-1a, and GSP-2 standards were treated as unknowns to evaluate data quality. The analytical precision of trace element analyses was estimated by the 2SD of repeated measurements of the BHVO-2, BCR-2, BIR-1a, and GSP-2 standards, which was between 1-5% for almost all REE, high field strength elements (HFSE), Sr, Y, La, Pb, and Ti, and within the range of 6-9% for Th, Tb, U, Cr, and Er (Appendix A, Table A4). The

measurement trueness was estimated using the difference between measured and accepted values for the BCR-2, BIR-1a, and GSP-2 standards. These were measured with an accuracy between <1-10% for REE, most HFSE, La, Th, Zr, Y, Cr, Sr, and Ni and 10-34% for U, Pb, Ta, Nb, Ti, and Gd.

2.6 ^{147}Sm - ^{143}Nd Isotope Analyses

A suite of thirteen samples was selected for Sm-Nd isotopic analysis. Samples that were selected exhibit minimal post-emplacement alteration (based on trace-element compositions and thin section observations) and are representative of all lithologies observed in the Qullinaaraaluk intrusion. Additionally, the two granitoid samples were analysed to assess for contamination of the Sm-Nd isotope systems.

Sample dissolution and Sm-Nd element separation took place in the clean laboratory of the Advanced Research Complex at the University of Ottawa. Enough sample powder (between 0.05 g and 0.3 g) was dissolved in order to obtain ~1000 ng of Nd. The dissolution method used is similar to the one described in detail in section 2.5. Dissolutions were performed using a 1:5 mixture of concentrated HNO_3 and HF reagents in Savillex beakers on a hotplate (for mafic and ultramafic samples) and in steel jacketed high-pressure Parr bombs in an oven (for granitoid samples). After drying, samples were re-dissolved in 6N HCl with a few drops of H_2BO_3 . Once the samples were completely dissolved in the HCl solution, an aliquot of the equivalent of ~ 300 ng of Nd was taken for the ^{147}Sm - ^{143}Nd analysis (leaving the rest of the sample, ~ 700 ng of Nd, for the $^{142}\text{Nd}/^{144}\text{Nd}$ investigations). A mixed spike of ^{150}Nd - ^{149}Sm was added to this aliquot for determination of Sm and Nd concentrations through isotope dilution. To ensure sample-

spike equilibration, the beakers with the spiked sample aliquots were sealed and heated at 125°C on a hotplate for two days and then dried at 85°C.

The procedure reported here for Sm and Nd extraction is based on the method in Pin and Zalduegui (1997) and is detailed in Appendix A, Table A5 and A6. The REE of the samples were separated using 10 mL Bio-Rad polypropylene columns filled with 2 mL 200-400 mesh AG50W-X8 cation exchange resin. In summary, the samples were dissolved in 2 mL of 2N HCl, centrifuged, and carefully loaded onto the pre-conditioned resin bed. The rock matrix elements were eluted in 2N and 2.5N HCl, and the REE fraction was collected in 6N HCl. The Sm and Nd were then separated from this REE fraction using 5 cm by 5 mm quartz columns filled with 300 mg of 50-100 µm LN-spec resin. The samples were dissolved in 0.25 mL of 0.2N HCl and carefully loaded into pre-conditioned columns. The LREE were first eluted in 0.2N HCl, followed by the collection of Nd in the same reagent. The Sm fraction was then collected in 0.5N HCL. Total chemistry blanks were 13 pg and 9 pg for Nd and Sm, respectively.

Samples were analyzed at Carleton University's Isotope Geochemistry and Geochronology Research Centre (IGGRC) using a *Thermo-Fisher Triton* Thermal Ionization Mass Spectrometer (TIMS). Samples and standards were loaded onto outgassed Re filaments and analyzed using a double-filament assembly. Measurements were performed in static mode using the cup configurations shown in Table 1 for Nd and Table 2 for Sm.

Table 1: Faraday cup configuration for Nd isotope measurements

L4	L3	L2	L1	C	H1	H2	H3	H4
-	¹⁴³ Nd	¹⁴⁴ Nd	¹⁴⁵ Nd	¹⁴⁶ Nd	¹⁴⁷ Sm	¹⁴⁸ Nd	¹⁵⁰ Sm	-

Table 2: Faraday cup configuration for Sm measurement

L4	L3	L2	L1	C	H1	H2	H3	H4
¹⁴⁶ Nd	¹⁴⁷ Sm	¹⁴⁸ Sm	¹⁴⁹ Sm	¹⁵⁰ Sm	¹⁵² Sm	¹⁵⁴ Sm	¹⁵⁵ Gd	-

Each Nd analysis is the average of 140 measurements, split into 7 blocks of 20 ratios, with an acquisition time of 8.39 seconds. Peak centre and lens focus were performed every 4th block. Baselines of 30 seconds were measured between each block. Isobaric interference of ¹⁴⁴Sm on ¹⁴⁴Nd was monitored and corrected by measuring ¹⁴⁷Sm and ¹⁵⁰Sm. ¹⁵⁵Gd and ¹⁴⁶Nd were measured to correct for isobaric interference on Sm isotopes. Neodymium isotope measurements were corrected for instrumental mass bias fractionation using exponential law and a ¹⁴⁶Nd/¹⁴⁴Nd ratio of 0.7219. The measured average of the JNdi-1 Nd standards was ¹⁴³Nd/¹⁴⁴Nd = 0.512108 ± 6 (2SD, n=4), which is within error of the reported value of 0.512115 ± 7 (Tanaka et al., 2000). Reported Nd isotope compositions were corrected for the difference between the measured and reported value of the JNdi-1. Each Sm analysis is the average of 100 measurements taken with an acquisition time of 8.39 seconds. Samarium isotope measurements were corrected for instrumental mass bias fractionation using an exponential law and a ¹⁴⁷Sm/¹⁵²Sm ratio of 0.56081.

Isochrons were constructed using IsoplotRgui version 4.3 (Vermeesch, P., 2018). Calculation of ε¹⁴³Nd used CHUR values from Bouvier et al., 2008 (¹⁴³Nd/¹⁴⁴Nd = 0.512630 and ¹⁴⁷Sm/¹⁴⁴Nd = 0.1960).

2.7 Sample Preparation and Analysis for High Precision ^{142}Nd Isotope Measurements

A goal of this research project was to measure the Nd isotopes of Neoproterozoic subalkaline ferropicrite samples to determine their $^{142}\text{Nd}/^{144}\text{Nd}$ ratio at a high precision. Due to the isobaric interference of ^{142}Ce with ^{142}Nd , completely removing Ce from Nd fractions is important for accurate measurements. This cannot be performed using typical Sm-Nd separation (like the analytical procedure described above), and thus a different procedure was followed to ensure Nd purification. The procedure reported here for Nd purification is based on the methods in Garçon et al. (2018) and Li et al. (2015) and detailed in Appendix A, Table A7-A10.

After REE extraction from the dissolved samples using 10 mL Bio-Rad polypropylene columns filled with 2mL 200-400 mesh AG50W-X8 cation exchange resin, Nd was separated from Ce using polyethylene columns made from 10 mL disposable pipettes filled with 0.5 mL of 100-150 μm LN-spec resin. The resin beds were conditioned and the samples were loaded with a $\text{HNO}_3\text{-NaBrO}_3$ solution to create an oxidizing environment. By oxidizing Ce to a tetravalent state (+4) it adsorbs to the resin while the other REEs, including Nd, in a trivalent state (+3) pass through. After two passes of the samples through this column Ce was effectively removed. The Na and Br added to the samples in this step was then removed from by passing them through 10 mL Bio-Rad columns. Total chemistry blanks yielded ~ 16 pg of Nd.

Samples were analyzed at Carleton University's IGGRC using the *Thermo-Fisher Triton* TIMS. Samples and several JNdi-1 Nd standards were loaded onto outgassed zone-

refined 99.999% Re filaments. The faraday cup configuration used is presented in Table 3. Neodymium isotope measurements were performed using two acquisition lines with ^{144}Nd and ^{146}Nd in the axial faraday cup. This configuration allowed the measurement of all Nd isotopes, obtaining the $^{142}\text{Nd}/^{144}\text{Nd}$ ratio of the samples dynamically, and measuring Ce and Sm isotopes to monitor and correct for isobaric interferences. Dynamic measurements allow us to remove amplifier gain bias and obtain sub-5 ppm measurements in the $^{142}\text{Nd}/^{144}\text{Nd}$ ratio.

Table 3: Faraday cup configuration for dynamic $^{142}\text{Nd}/^{144}\text{Nd}$ measurements

	L4	L3	L2	L1	C	H1	H2	H3	H4
Line 1	^{140}Ce	^{141}Pr	^{142}Nd	^{143}Nd	^{144}Nd	^{145}Nd	^{146}Nd	^{148}Nd	–
Line 2	^{142}Nd	^{143}Nd	^{144}Nd	^{145}Nd	^{146}Nd	^{147}Sm	^{148}Nd	^{150}Nd	–

The TIMS method used 24 blocks of 25 measurement cycles with an acquisition time of 8.39 seconds each, measuring approximately 600 ratios for each sample. In between each block a baseline of 30 seconds was measured. Peak centre and lens focus were performed every 4th block.

Isotope measurements were reduced and corrected for isobaric interferences with an in-house MATLAB program (Peters, pers comm.) by converting measurements of ^{140}Ce and ^{147}Sm to their interfering counterparts using known natural isotopic compositions. Measurements of ^{142}Ce ($\bar{x} = -0.000007 \pm 5, -0.000011 \pm 3, -0.000010 \pm 5$) and ^{144}Sm ($\bar{x} = 0.000000 \pm 1, 0.000000 \pm 1, 0.000000 \pm 1$) were within the background noise of the session. Instrumental mass bias fractionation was corrected using exponential law and a $^{146}\text{Nd}/^{144}\text{Nd}$ ratio of 0.7219. Since the $^{142}\text{Nd}/^{144}\text{Nd}$ ratio is obtained dynamically, the mass fractionation of $^{142}\text{Nd}/^{144}\text{Nd}$ ratio in line 1 was corrected using the

$^{146}\text{Nd}/^{144}\text{Nd}$ ratio of line 2 as they were measured in the same cups (L2 and C, Table 3). The mass bias fractionation was further time-resolved by interpolating the respective isotope abundances to the missing line using a cubic spline algorithm.

The Nd isotope compositions of samples were measured over three analytical sessions. The $^{142}\text{Nd}/^{144}\text{Nd}$ of samples is normalized to the average JNdi-1 values obtained from their respective analysis' session. Results from JNdi-1 measurements for the three sessions are shown in Figure 2.1 and presented in Appendix A, Table A13. The $^{142}\text{Nd}/^{144}\text{Nd}$ average for the JNdi-1 standard was 1.141836 ± 6 (2SD, n=9) for the first session, 1.141835 ± 5 (2SD, n=8) for the second session, and 1.141835 ± 3 (2SD, n=6) for the third session, which is within error of other reported values such as the 1.141832 ± 6 (2SD) of Garçon et al. (2018).

The $\mu^{145}\text{Nd}$, $\mu^{148}\text{Nd}$, and $\mu^{150}\text{Nd}$ were used to assess the accuracy of the measurements. As these are all stable Nd isotopes (i.e., not affected by radioactive decay), their ratios are expected to be uniform for terrestrial samples and the same within error for Nd standards. As such, any deviations in $\mu^{145}\text{Nd}$, $\mu^{148}\text{Nd}$, and $\mu^{150}\text{Nd}$ reflect possible issues during measurements. Results that yielded deviant $\mu^{145}\text{Nd}$, $\mu^{148}\text{Nd}$, and $\mu^{150}\text{Nd}$, representing issues with the analysis, were excluded from the average calculations (Appendix A, Figure A1, A2).

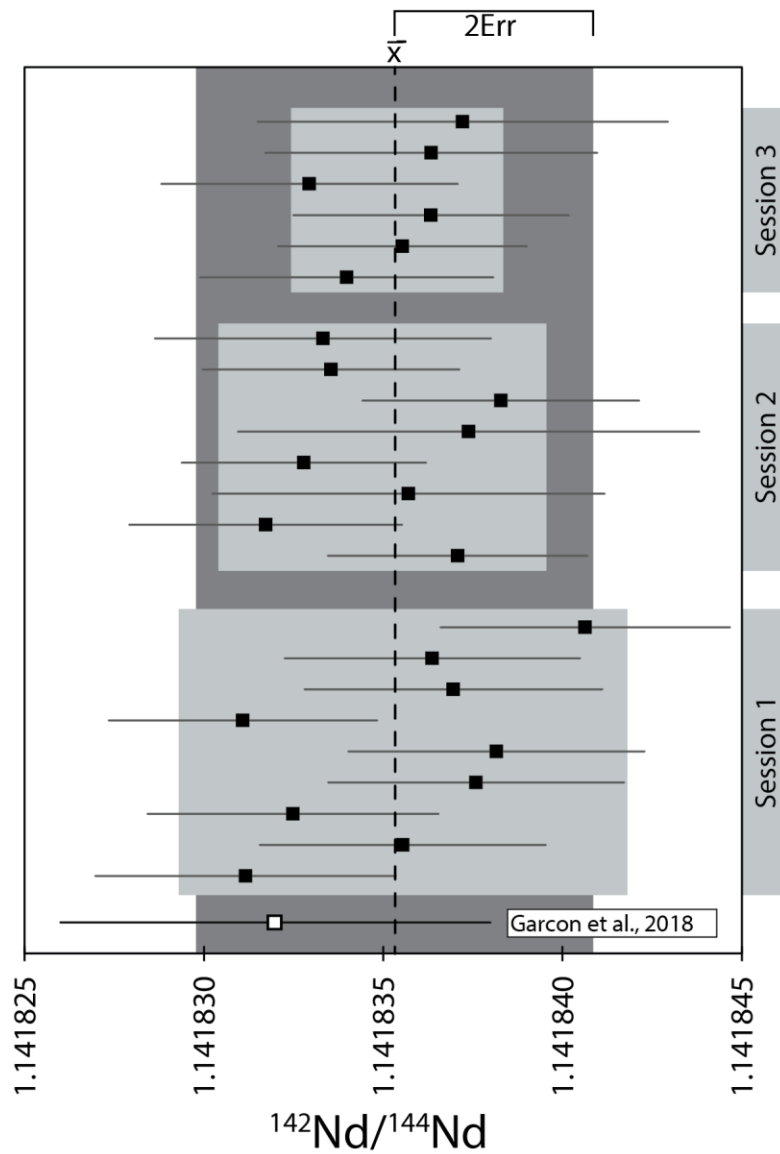


Figure 2.1: $^{142}\text{Nd}/^{144}\text{Nd}$ ratios of JNdi-1 standards measured during the three analytical sessions. The light gray boxes represent 2SD calculated for each session. The dashed line indicates average taken from all ratios. The dark gray box indicates the propagated error on the average calculated using a least squares regression. The white square indicates the reported value for the JNdi-1 standard.

3.0 Results

3.1 Petrological and Major and Trace Element Results of the Qullinaaraaluk Intrusion

The petrology of the Qullinaaraaluk intrusion was described in detail by Milidragovic et al. (2014). As it is not a focus of this study, it will only be briefly described here to allow for comparison between the chemically differentiated units of the intrusion. Thin section observations, coupled with CIPW normative mineralogy calculations and major and trace element compositions, allow samples to be divided into four lithologies: peridotite (samples QK-004, QK-009, QK-011), harzburgite (a subset of the peridotites, samples QK-010, QK-013), olivine-websterite (samples QK-001, QK-002, QK-003, QK-007, QK-008, QK-012, QK-014, QK-019, QK-020, QK-021, QK-022, QK-023) and gabbro (samples QK-005, QK-006, QK-017, QK-024). Representative thin section micrographs for each lithology are displayed in Appendix B, Figures B1-B4. Harzburgites are dominated by serpentinized olivine and orthopyroxene, with interstitial amphibole. Peridotites are dominated by serpentinized olivine, orthopyroxene, and clinopyroxene, with interstitial amphibole. Websterites have assemblages of orthopyroxene and clinopyroxene, with clinopyroxene being replaced by amphibole, and minor olivine, interstitial plagioclase, and biotite. Gabbros have assemblages of orthopyroxene, clinopyroxene, and plagioclase, with interstitial K-feldspar, biotite, amphibole, and quartz. Granodiorites contain plagioclase, quartz, K-feldspar, orthopyroxene, and amphibole. The CIPW normative mineralogy compositions of the Qullinaaraaluk samples and surrounding granitoids were calculated using major and trace element compositions (Figure 3.1). The CIPW compositions were

found to be in agreement with mineral assemblages observed in thin sections (Appendix B, Figure B1-B5).

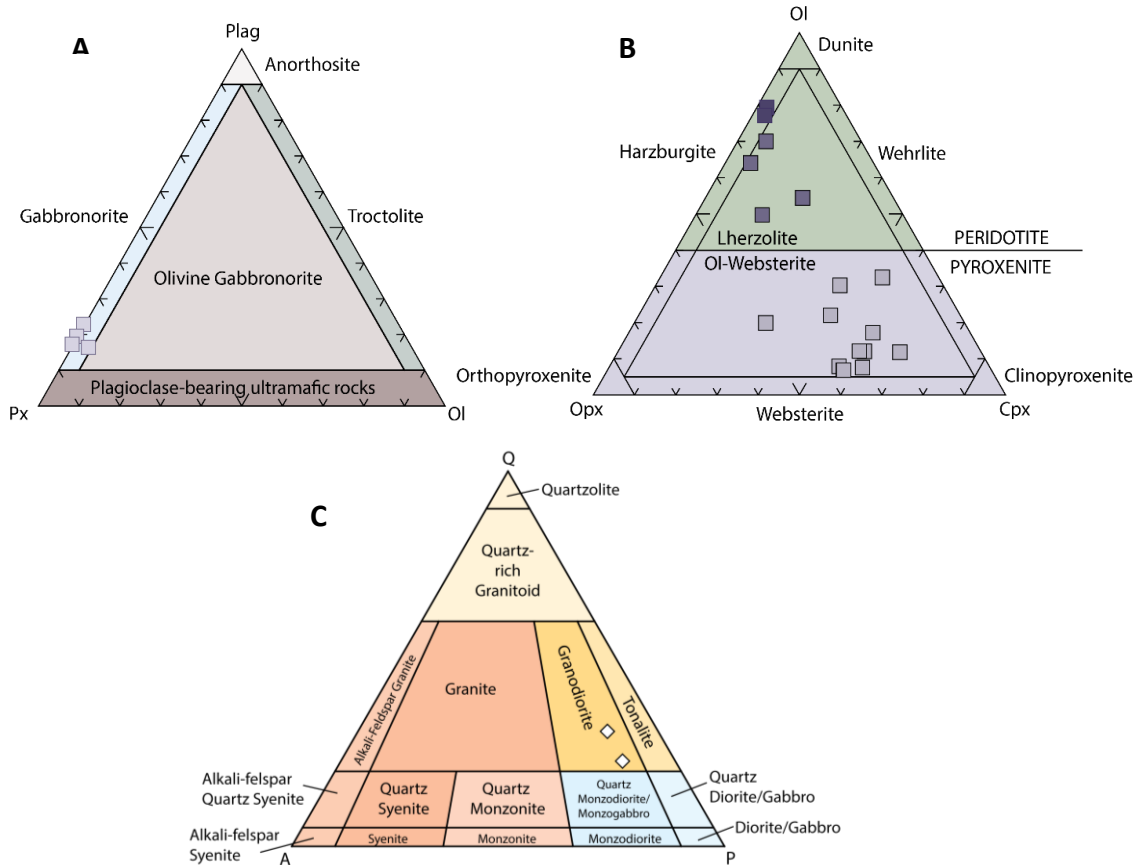


Figure 3.1: Normative mineralogy classification diagrams for mafic (a) and ultramafic (b) rocks of the Qullinaaraaluk intrusion, and (c) granodiorites surrounding the intrusion. Major element compositions used were normalized to 100%-LOI (anhydrous) for comparison.

The major and trace element compositions of samples representing the main lithologies of the Qullinaaraaluk intrusion and surrounding granodiorites are presented in Table 4. The complete geochemical data table with all analyzed samples is included in Appendix B, Table B2. Major and trace element compositions of the samples studied here are indistinguishable from the Q-suite samples studied by Milidragovic et al. (2014). Only key element abundances and abundance ratios will be detailed in this section. All samples

have undergone variable degrees of alteration as reflected by their LOI, ranging from 0.6 to 10.1 wt%. Therefore, major elements were recalculated to anhydrous abundances for comparison. Qullinaaraaluk samples have FeO_{TOT} contents ranging from 8.0 to 18.8 wt.% and MgO contents ranging from 15.1 to 36.2 wt.% (Figure 3.2). The FeO_{TOT} content is positively correlated with the MgO content. The Al_2O_3 contents ranges from 2.1 to 6.1 wt%, and the TiO_2 contents range from 0.1 to 0.3 wt%. There is a positive correlation between Al_2O_3 content and TiO_2 content (Figure 3.3).

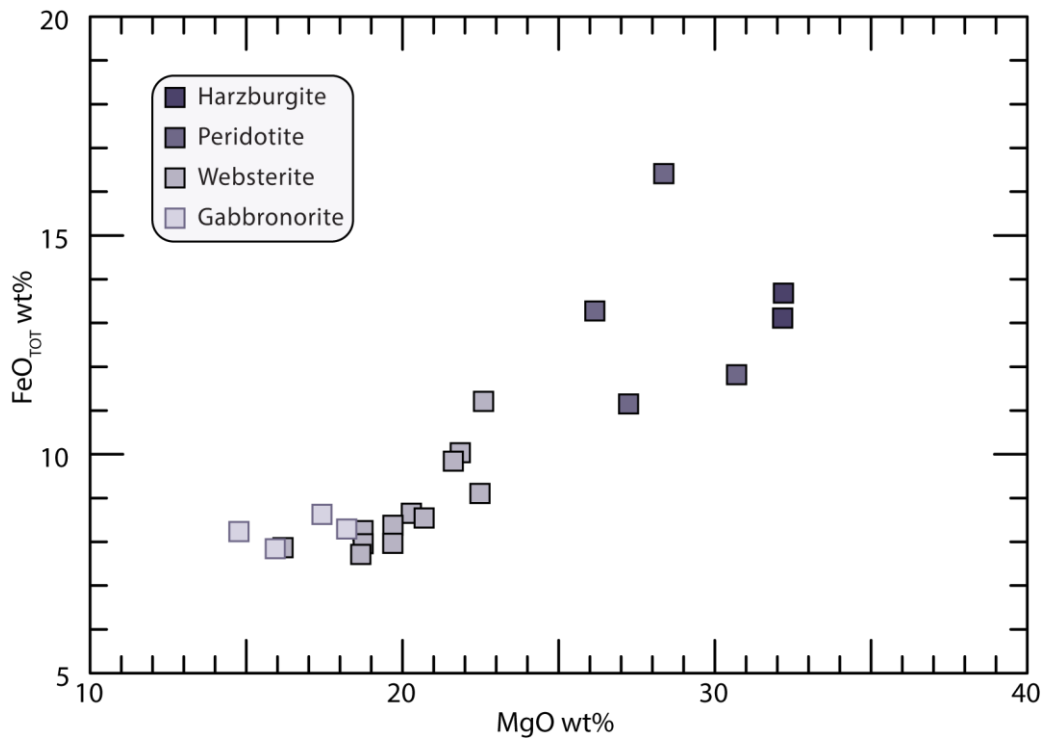


Figure 3.2: FeO_{TOT} wt% versus MgO wt% of the Qullinaaraaluk intrusion.

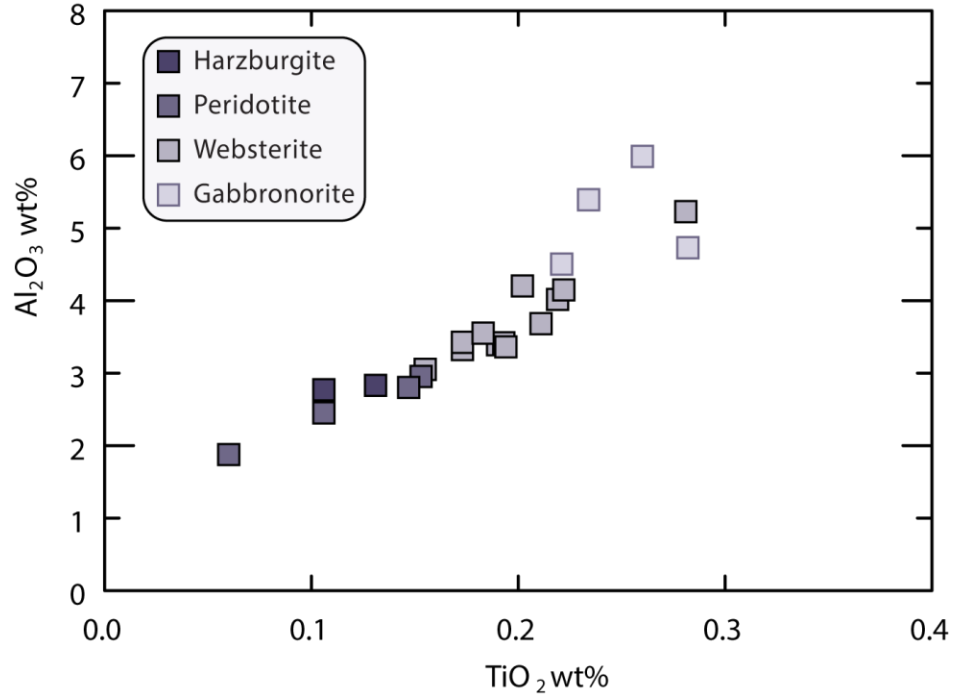


Figure 3.3: TiO_2 wt % versus Al_2O_3 wt % of the Qullinaaraaluk intrusion.

Figures 3.4 and 3.5 show the trace element abundances of the Qullinaaraaluk intrusion and granodiorites, normalized to primitive mantle (Fig 3.4) and chondrite (Fig 3.5) compositions. Generally, the harzburgite samples have the lowest trace element concentrations, followed by the peridotites, then the websterites, with the gabbronorites having the highest trace element contents. Only the incompatible elements relevant to the discussion will be detailed here. Niobium concentrations range from 0.15 to 2.27 ppm, Nd concentrations range from 2.70 to 23.08 ppm, Sm concentrations range from 0.40 to 3.41 ppm, Yb concentrations range from 0.13 to 0.82 ppm, and Sc concentrations range from 3.04 to 49.33 ppm. The Qullinaaraaluk rocks have Ni concentrations ranging from 217 to 1928 ppm, with a median concentration of 638 ppm (n=18). They have Cr concentrations ranging from 818 to 3367 ppm, with a median concentration of 818 ppm

(n=18). Excepting a few websterite samples, harzburgites and peridotites have the highest Ni concentrations, while gabbronorites have the lowest (Figure 3.6).

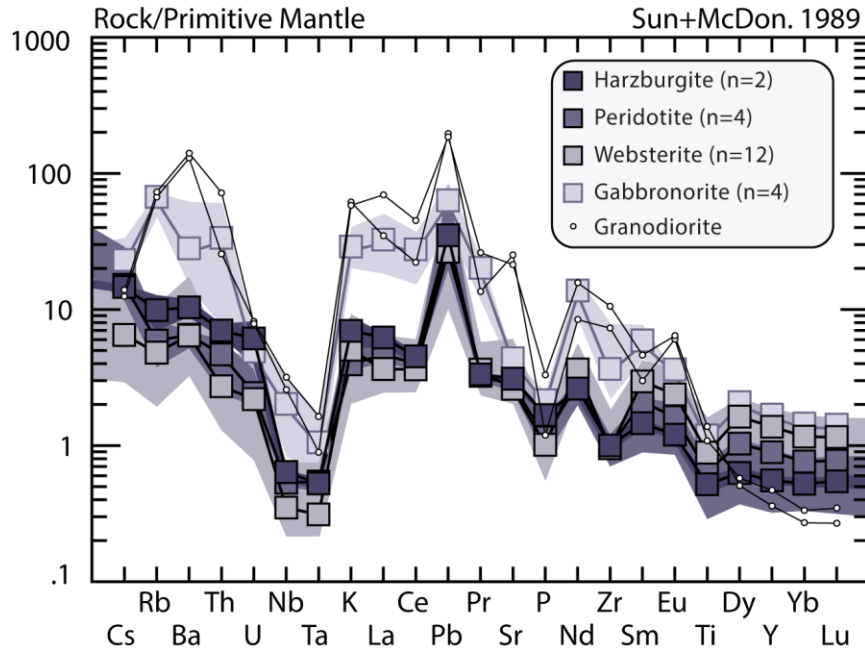


Figure 3.4 Trace element concentrations of the Qullinaaraaluk intrusion normalized to the primitive mantle. Shaded areas show the range of each lithology and boxes show median values. Primitive mantle values from Sun & McDonough (1989).

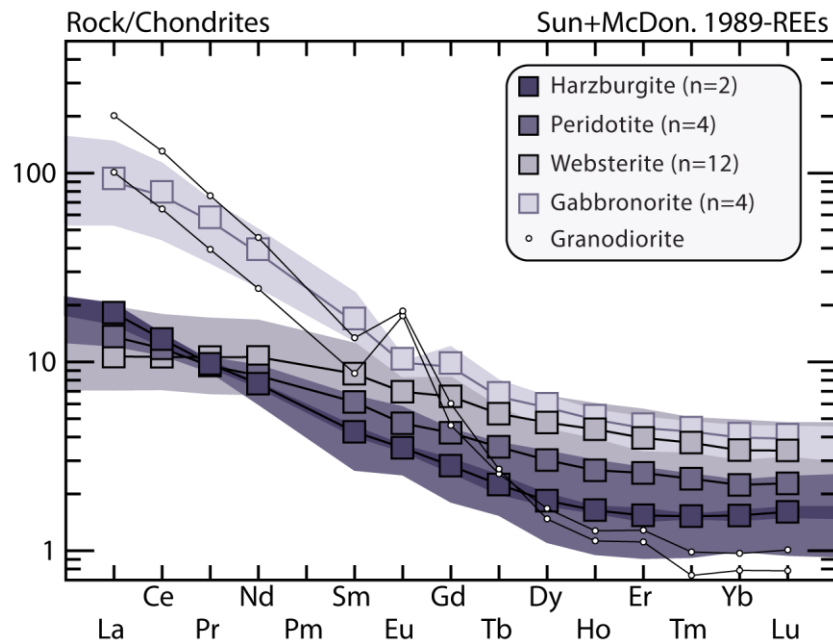


Figure 3.5: Rare earth element concentrations normalized to chondrites. Shaded areas show the range of each lithology and boxes show median values. Chondrite values from Sun & McDonough (1989).

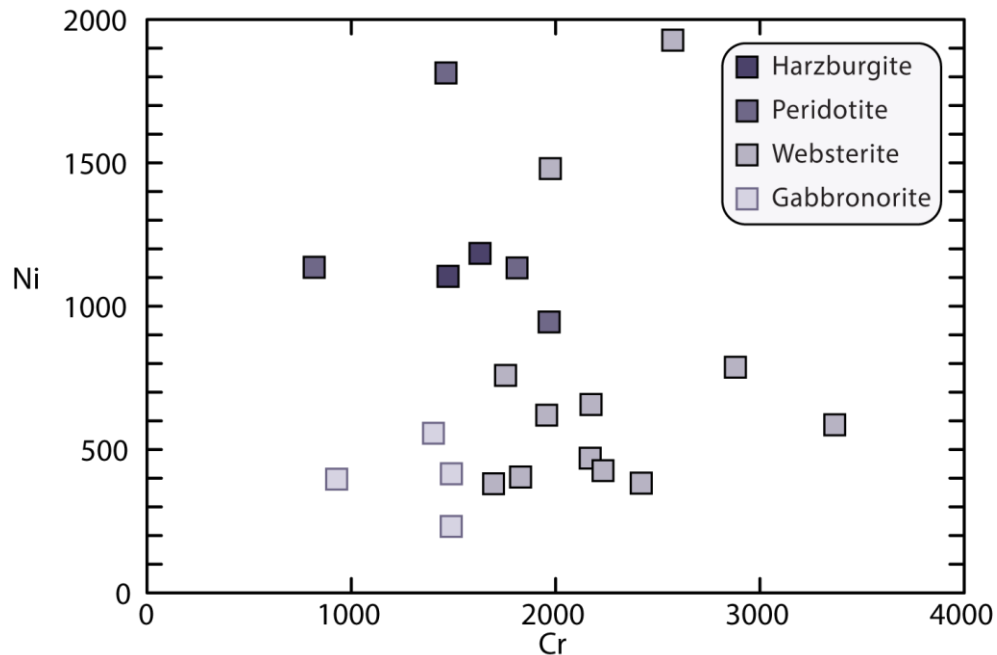


Figure 3.6: Ni versus Cr concentrations in ppm for the Qullinaaraaluk samples.

Trace element compositions of the Qullinaaraaluk samples normalized to the primitive mantle (Figure 3.4) reveal enrichments in most trace elements with some exceptions. There are notable depletions in HFSE such as Nb, Ta, Zr, and Ti. Lead is enriched in all samples relative to the similarly incompatible elements such as Ce and Pr. Compared to the other lithologies, the gabbronorites exhibit the highest enrichments in the large ion lithophile elements (LILE) Rb, Ba, Th, and Pb. The enrichment in LILE of the gabbronorites is comparable to the surrounding granodiorites, however the granodiorites are more enriched in Ba, Pb, Sr, Zr, and Eu. The Qullinaaraaluk samples have a range in Nb/Y_N from 0.18 to 1.79, with a median of 0.47 (n=18). REE concentrations of all Qullinaaraaluk samples are higher than the chondrite compositions (Figure 3.5). All samples show enrichments in LREE relative to HREE. With the exception of the gabbronorites, the La/Gd_N ratios for the samples range from 1.34 to 9.24, with a median of 2.13, and Gd/Yb_N ratios range from 1.57 to 2.10, with a median of 1.86 (n= 18, Figure

3.7). The gabbro-norites are significantly more enriched in LREE than the other lithologies, with La/Gd_N ratios ranging from 6.08 to 15.61 with a median of 8.24 ($n=4$). The granodiorites show enrichments in LREE ($\text{La}/\text{Gd}_N= 21.88, 33.52$). They have positive Eu anomalies and display fractionated HREE with a Gd/Yb_N of 4.77 and 7.56.

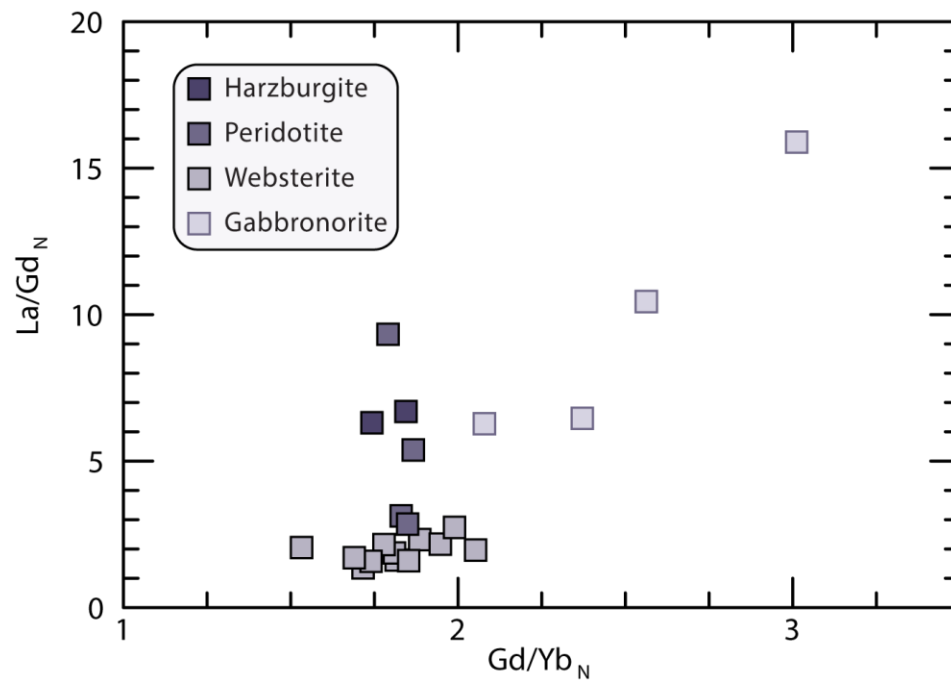


Figure 3.7: La/Gd versus Gd/Yb normalized to chondritic values for the Qullinaaraaluk samples.

Table 4: Major element oxide and trace element compositions of samples representative of each of the main lithologies of the Qullinaaraaluk intrusion

Sample Lithology	QK-013 <i>Harzburgite</i>	QK-016 <i>Peridotite</i>	QK-008 <i>Websterite</i>	QK-005 <i>Gabbronorite</i>	QK-015 <i>Granodiorite</i>
SiO₂ (wt%)	43.5	46.9	52.9	54.5	68.7
TiO₂	0.144	0.165	0.197	0.230	0.195
Al₂O₃	3.11	3.14	3.51	4.62	17.39
FeO*	15.0	14.9	8.9	8.5	1.9
MnO	0.18	0.23	0.18	0.15	0.02
MgO	35.4	29.3	21.4	18.9	0.9
CaO	2.1	4.9	12.4	11.4	4.0
Na₂O	0.30	0.38	0.43	1.04	4.95
K₂O	0.29	0.12	0.06	0.63	1.88
P₂O₅	0.04	0.02	0.02	0.05	0.03
LOI	7.01	8.38	2.01	2.26	0.84
Sc (ppm)	10.79	20.70	48.78	46.77	3.04
Ti	746	888	1040	1282	1409
Cr	1630	1463	1828	1490	16
Ni	1184	1813	404	401	16
Sr	68.0	58.8	53.1	83.7	530.0
Y	2.62	4.07	5.35	6.59	2.14
Zr	10.0	11.6	8.1	24.6	81.7
Nb	0.440	0.356	0.153	0.592	2.268
La	4.72	2.79	1.68	12.58	23.93
Ce	8.45	6.45	4.80	27.21	39.44
Pr	0.94	0.90	0.81	3.18	3.74
Nd	3.54	4.11	4.09	11.62	11.43
Sm	0.61	0.93	1.14	1.98	1.33
Eu	0.197	0.272	0.342	0.484	1.018
Gd	0.62	0.86	1.09	1.74	0.95
Tb	0.092	0.131	0.169	0.230	0.095
Dy	0.490	0.760	1.054	1.302	0.425
Ho	0.095	0.150	0.219	0.248	0.072
Er	0.270	0.423	0.555	0.676	0.213
Tm	0.039	0.061	0.083	0.097	0.025
Yb	0.271	0.375	0.513	0.595	0.165
Lu	0.042	0.057	0.077	0.090	0.026
Hf	0.300	0.333	0.316	0.831	2.304
Ta	0.020	0.019	0.009	0.025	0.067
Pb	2.56	2.33	0.72	2.73	13.93
Th	0.666	0.205	0.115	1.161	2.174
U	0.172	0.041	0.020	0.080	0.172

3.2 ^{147}Sm - ^{143}Nd Systematics

The results from ^{147}Sm - ^{143}Nd analyses for 13 Qullinaaraaluk intrusion samples and 2 granodiorite samples surrounding the intrusion are reported in Table 5 and plotted in Figure 3.8.

Qullinaaraaluk Nd concentrations were measured through isotope dilution. Excepting the gabbro-norites, Nd concentrations range from 2.63 to 4.19 ppm. The gabbro-norites range from 10.21 to 23.09 ppm. The granodiorites have Nd concentrations of 4.65 ppm and 20.31 ppm. The Qullinaaraaluk samples' $^{147}\text{Sm}/^{144}\text{Nd}$ ratios range from 0.0742 ± 0.0004 (2SE) to 0.1653 ± 0.0008 (2SE). The $^{143}\text{Nd}/^{144}\text{Nd}$ isotope compositions range from 0.510331 ± 0.000005 (2SE) to 0.512021 ± 0.000005 (2SE). All the Qullinaaraaluk samples define a $^{147}\text{Sm}/^{144}\text{Nd}$ vs. $^{143}\text{Nd}/^{144}\text{Nd}$ regression (Figure 3.8, n=13) corresponding to an isochron age of 2833 ± 56 Ma (MSWD = 9.7), with an initial $^{143}\text{Nd}/^{144}\text{Nd}$ of 0.50895 ± 0.00004 corresponding to an initial $\epsilon^{143}\text{Nd}$ value of -0.28 ± 0.08 (2S). This isochron age is older than previous estimates for other Q-Suite intrusions obtained from U-Pb on zircons from gabbro-norite units (2705 ± 1 Ma to 2718.9 ± 0.7 Ma; Simard, 2008; Milidragovic and Francis, 2014) and from a cross-cutting pegmatite (2720 ± 2 Ma; Simard, 2008).

The two granodiorite samples analyzed yield $^{147}\text{Sm}/^{144}\text{Nd}$ ratios ranging from 0.0473 ± 0.0004 (2SE) to 0.0710 ± 0.0002 (2SE) and $^{143}\text{Nd}/^{144}\text{Nd}$ ratios between 0.510041 ± 0.000005 (2SE) and 0.510266 ± 0.000004 (2SE). Using the age of 2750 Ma given for the Loups Marins suite (Simard; 2008), the initial $\epsilon^{143}\text{Nd}$ of the granodiorites is -1.87 for QK-015 and +2.15 for QK-018, with model ages (T_{DM}) of 3073 Ma and 2843 Ma, respectively.

Table 5: ^{147}Sm - ^{143}Nd analysis results

Sample	Lithology	Sm (ppm)	Nd (ppm)	$^{147}\text{Sm}/^{144}\text{Nd}$	2SE	$^{143}\text{Nd}/^{144}\text{Nd}$	2SE	ϵNd_i
QK-003	<i>Websterite</i>	1.12	4.19	0.1618	±8	0.511949	±5	-0.81
QK-004	<i>Peridotite</i>	0.51	2.78	0.1113	±6	0.511067	±5	0.44
QK-005	<i>Gabbronorite</i>	1.79	10.21	0.1058	±5	0.510918	±4	-0.47
QK-006	<i>Gabbronorite</i>	2.28	18.57	0.0742	±4	0.510331	±5	-0.39
QK-008	<i>Websterite</i>	0.94	3.45	0.1653	±8	0.512021	±5	-0.68
QK-010	<i>Harzburgite</i>	0.50	2.72	0.1121	±6	0.511071	±4	0.20
QK-012	<i>Websterite</i>	1.07	3.96	0.1629	±8	0.511983	±5	-0.52
QK-013	<i>Harzburgite</i>	0.51	2.74	0.1132	±6	0.511086	±5	0.09
QK-015	<i>Granodiorite</i>	0.55	4.65	0.0710	±4	0.510266	±4	-0.50
QK-016	<i>Peridotite</i>	0.76	3.28	0.1396	±7	0.511564	±5	-0.20
QK-017	<i>Gabbronorite</i>	3.05	23.09	0.0798	±4	0.510430	±4	-0.52
QK-018	<i>Granodiorite</i>	0.73	20.31	0.0473	±2	0.510041	±5	3.78
QK-021	<i>Websterite</i>	0.67	2.63	0.1531	±8	0.511806	±4	-0.41
QK-023	<i>Websterite</i>	0.92	3.46	0.1614	±8	0.511952	±6	-0.58
QK-024	<i>Gabbronorite</i>	2.06	12.54	0.0991	±5	0.510787	±4	-0.59

Errors given in the last decimal place. ϵNd_i were calculated using an age of 2833 Ma (obtained from the isochron in Fig. 3.8) and the CHUR values for $^{143}\text{Nd}/^{144}\text{Nd}$ and $^{147}\text{Sm}/^{144}\text{Nd}$ from Bouvier et al. (2008).

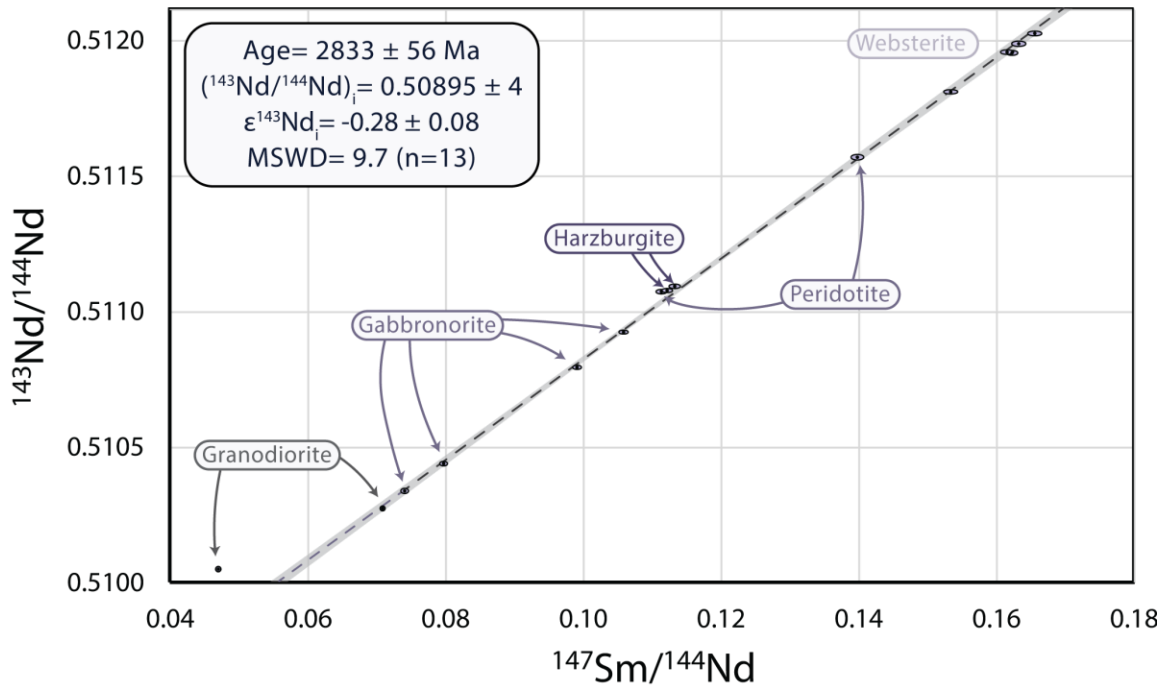


Figure 3.8: $^{147}\text{Sm}/^{144}\text{Nd}$ vs. $^{143}\text{Nd}/^{144}\text{Nd}$ plot of the Qullinaaraaluk samples. Isochron age, initial Nd isotope composition, and MSWD was obtained using Vermeesch (2018). Gray area indicates error on the line. Ellipsoids indicate 2SD error on the points, calculated by Isoplot. The 2 granodiorite samples studied here are not used in the isochron regression and are plotted for comparison.

3.3 ^{146}Sm - ^{142}Nd Systematics

Results from high precision Nd isotope analyses of 12 Qullinaaraaluk samples and the 2 granodiorites are reported in Table 6 and shown in Figure 3.9.

The $^{142}\text{Nd}/^{144}\text{Nd}$ ratios of the Qullinaaraaluk samples are reported as $\mu^{142}\text{Nd}$ values in order to identify part per million (ppm) deviations from the average Nd isotope composition of the JNd-1 Nd terrestrial standard ($\mu^{142}\text{Nd} = 0$ by definition). The $\mu^{142}\text{Nd}$ values of the Qullinaaraaluk samples range from -3.0 ± 3.9 (2SE) to 1.8 ± 5.5 (2SE), with a median value of -0.3 and an average of -0.4 ± 5.5 (2SD, n= 12). There is no discernable relationship between $\mu^{142}\text{Nd}$ variation and lithology. The $\mu^{142}\text{Nd}$ values of the

Qullinaaraaluk samples are all unresolvable from the JNdi-1 Nd terrestrial standard given the analytical precision of this study (± 4.8 ppm).

The $\mu^{142}\text{Nd}$ of the granitoids are 1.5 ± 3.5 (2SE) and 0.0 ± 3.6 (2SE). Similar to the mafic and ultramafic samples of the Qullinaaraaluk intrusion, $\mu^{142}\text{Nd}$ values of the granitoids are unresolvable from the average JNdi-1 terrestrial standard.

Table 6: ^{142}Nd Analysis Results

	Session	Sample	$^{140}\text{Ce}/^{144}\text{Nd}$ 2SE	$^{147}\text{Sm}/^{144}\text{Nd}$ 2SE	$^{142}\text{Nd}/^{144}\text{Nd}$ $\pm 2\text{SE}$	$\mu^{142}\text{Nd}$ $\pm 2\text{SE}$	$\mu^{145}\text{Nd}$ $\pm 2\text{SE}$	$\mu^{148}\text{Nd}$ $\pm 2\text{SE}$	$\mu^{150}\text{Nd}$ $\pm 2\text{SE}$
Harzburgite	1	QK-010	-0.000006 $\pm <1$	-0.000002 $\pm <1$	1.141836 4	0.2 3.1	6.7 3.6	-29.9 5.7	-42.1 7.5
	3	QK-010	-0.000006 $\pm <1$	-0.000003 $\pm <1$	1.141839 5	3.4 4.5	-8.6 4.4	2.5 7.0	-5.4 9.5
	avg	QK-010			1.141838 6	1.8 5.5			
	2	QK-013	-0.000010 ± 1	-0.000003 $\pm <1$	1.141835 4	0.0 3.8	5.9 4.3	7.9 6.2	1.4 8.8
Perid.	2	QK-004	0.000016 ± 1	-0.000002 $\pm <1$	1.141837 7	1.7 6.0	1.8 6.8	15.5 10.1	11.4 14.4
	2	QK-016	0.000023 ± 4	0.000002 ± 1	1.141834 9	-1.2 8.1	11.9 8.1	25.1 14.9	2.1 18.8
Websterite	2	QK-003	0.000011 ± 1	-0.000002 $\pm <1$	1.141834 4	-0.9 3.8	0.6 4.1	-2.1 7.4	-3.6 9.5
	2	QK-008	0.000013 ± 1	-0.000002 $\pm <1$	1.141834 4	-0.7 3.6	8.0 3.8	0.4 5.6	1.3 7.6
	2	QK-012	-0.000009 $\pm <1$	-0.000003 $\pm <1$	1.141835 4	0.1 3.6	4.8 3.9	7.5 5.8	40.1 8.2
	2	QK-023	0.000000 ± 1	-0.000003 $\pm <1$	1.141832 4	-3.0 3.9	-1.1 4.2	7.1 6.4	-4.4 8.6
	3	QK-005	0.000004 ± 1	-0.000002 ± 1	1.141832 10	-2.7 8.6	-1.0 9.7	-0.5 12.6	-1.7 18.1
Gabbro-norite	1	QK-006	-0.000007 $\pm <1$	-0.000004 $\pm <1$	1.141841 4	4.6 3.6	10.6 3.7	-33.3 6.0	-48.9 7.9
	2	QK-006	-0.000004 ± 1	-0.000003 $\pm <1$	1.141831 4	-3.6 3.6	3.7 4.3	-0.4 6.4	-9.2 8.5
	avg	QK-006			1.141836 6	0.5 5.1			
	1	QK-017_r1	0.000002 ± 1	-0.000003 $\pm <1$	1.141835 4	-0.9 3.4	-14.1 4.1	-11.0 5.8	-9.0 8.0
	1	QK-017_r2	-0.000007 $\pm <1$	-0.000003 $\pm <1$	1.141838 4	2.3 3.6	-3.0 4.0	-22.6 6.2	-40.8 8.7
	3	QK-017	-0.000001 ± 1	-0.000002 $\pm <1$	1.141827 4	-7.2 3.5	-0.6 4.0	1.3 6.2	-8.8 8.0
	avg	QK-017			1.141833 5	-1.9 4.0			
2	QK-024	0.000033 ± 1	-0.000003 $\pm <1$	1.141837 4	1.4 3.8	5.3 4.3	3.4 6.5	6.6 8.9	
Granodi.	2	QK-018	0.000046 ± 1	-0.000003 $\pm <1$	1.141835 4	0.0 3.6	13.7 3.6	5.8 6.0	12.4 8.3
	2	QK-015	-0.000005 $\pm <1$	-0.000003 $\pm <1$	1.141836 4	1.2 3.5	5.2 3.6	12.1 6.3	7.8 7.5

Errors given in the last decimal place. $\mu^{142}\text{Nd}$ values calculated using average JNdi-1 measurements for respective sessions.

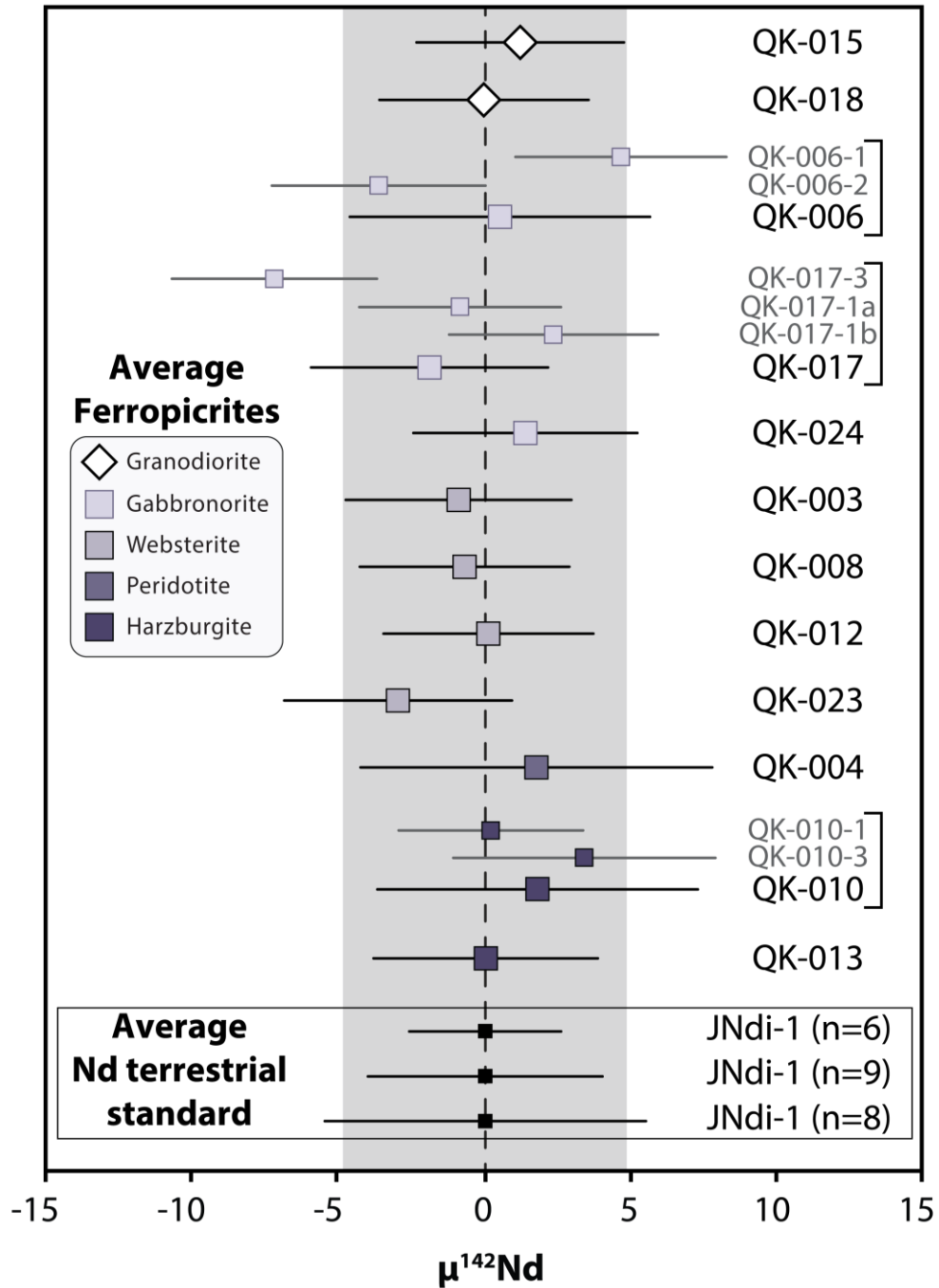


Figure 3.9: $\mu^{142}\text{Nd}$ results for the Qullinaaraaluk and granodiorite samples. Large square symbols show measurements with black error bars representing 2SD. For samples with multiple runs (indicated by brackets), small square symbols show individual runs with gray error bars representing 2SD, while large square symbols show the average of the runs with propagated error calculated from the multiple runs. Numbers next to sample names represent the measurement's session. The shaded grey area is the 4.8 ppm propagated error on the average of JNdi-1 standard measurements from all sessions. JNdi-1 errors from individual sessions are represented by the small black squares.

4.0 Discussion

4.1 The ^{147}Sm - ^{143}Nd Age and Source Composition of the Qullinaaraaluk Intrusion

The long-lived Sm-Nd radiogenic isotope system is a useful tool when studying ancient mantle-derived rocks, as it allows us to extract information on the differentiation history of the Earth's silicate reservoirs. The age obtained from a Sm-Nd isochron can be combined with initial Nd isotope compositions to determine $\epsilon^{143}\text{Nd}$ values. These provide valuable information regarding the source of rock samples, such as whether the source evolved with super, sub, or chondritic Sm/Nd ratios, and how that source compares to the evolution of the depleted mantle (DMM, DePaolo 1980). Given that Nd is more incompatible than Sm during igneous processes, source Sm/Nd ratios directly relate to the incompatible trace element enrichment of reservoirs. Therefore, assessing the reliability of the Sm-Nd isochron ages and initial Nd isotope compositions obtained from the Qullinaaraaluk intrusion is crucial when using the data to investigate the mantle source of subalkaline ferropicrites.

The Sm-Nd isochron obtained from plotting all the analyzed Qullinaaraaluk samples yields an age of 2833 ± 56 Ma (Figure 3.8). The mean squared weighted deviation (MSWD) of this isochron corresponds to 9.7. This MSWD value is higher than 1, reflecting an excess of scatter in the data that could indicate the assumptions for an isochron are not met (See section 1.31, i.e., rocks are not cogenetic, the parent/daughter ratio has been disturbed). Furthermore, the 2833 ± 56 Ma isochron age obtained is inconsistent with previous age-dating of the Q-Suite intrusions. Studies using U-Pb dating of zircons from the gabbro-norite lithology obtained ages of 2707 ± 1 Ma, 2705 ± 1 Ma (Simard,

2008), 2718.9 ± 0.7 Ma, and 2710.0 ± 0.5 Ma (Milidragovic and Francis, 2014), and U-Pb dating of a zircon in a pegmatite cross-cutting a Q-Suite intrusion obtained an age of 2720 ± 2 Ma (Simard, 2008).

For a Sm-Nd isochron to have geochronological meaning, the studied suite of rocks must be co-genetic and the ^{147}Sm - ^{143}Nd isotopic system must have remained closed since their formation. Truly co-genetic rock samples should have identical initial Nd isotope compositions at the time of formation, regardless of their trace element enrichments resulting from chemical differentiation. To assess the veracity of the Sm-Nd isochron, the initial Nd isotope compositions of the samples can be calculated at the accepted age of the intrusion and compared to their respective Nd concentrations. Figure 4.1 shows the initial $\epsilon^{143}\text{Nd}$ values for the samples calculated at 2720 Ma, used as the accepted age of the Qullinaaraaluk intrusion in Milidragovic et al. (2014), plotted against the reciprocal of their Nd concentrations. With the exception of the gabbro-norite unit, all other ultramafic and mafic samples have indistinguishable $\epsilon^{143}\text{Nd}_{2720}$ within 2SD of the average, indicating that they derived from the same source (cogenetic) and their Sm-Nd systematics have remained closed since their formation. In contrast, the gabbro-norites plot outside of the 2SD, which suggests that the ^{147}Sm - ^{143}Nd systematics of the gabbro-norites has been modified and should not be used on an isochron to determine the crystallization age of the intrusion.

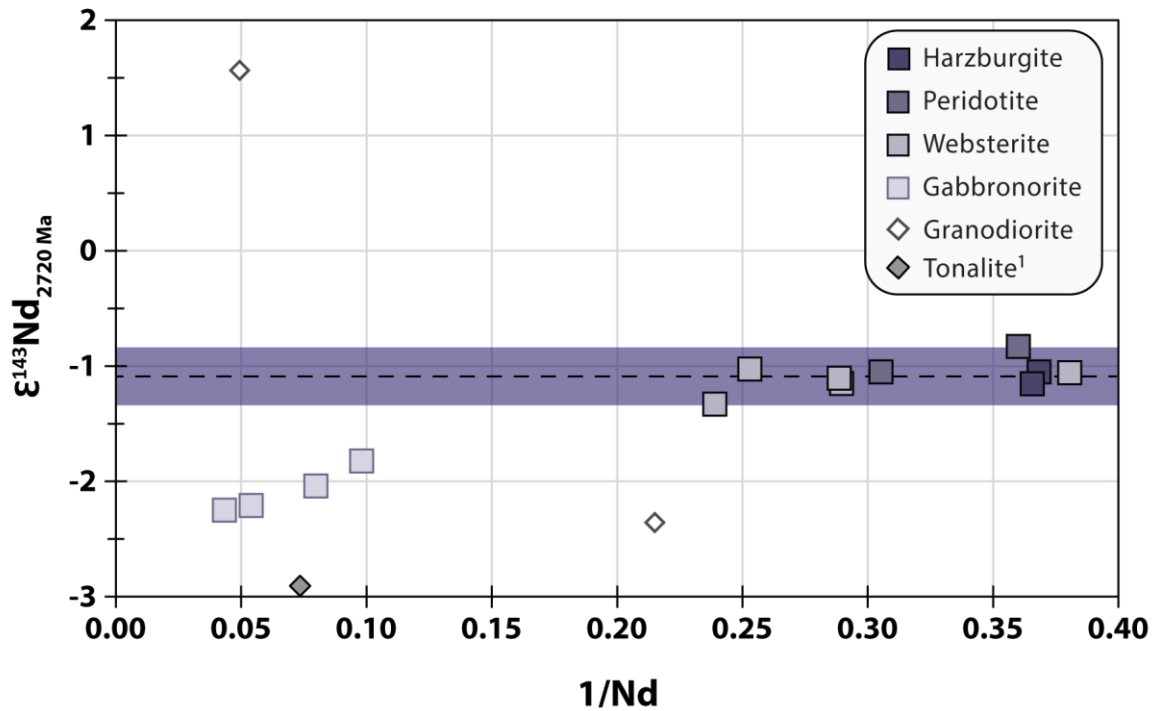


Figure 4.1: $\epsilon^{143}\text{Nd}$ calculated at 2720 Ma plotted against $1/\text{Nd}$. Age of 2720 Ma taken from Milidragovic et al. (2014). Dashed lines indicate average $\epsilon^{143}\text{Nd}$ for 2720 Ma, with the purple shaded area representing 2SD. Granodiorite and tonalite¹ plotted for comparison (O'Neil and Carlson, 2017).

The offset of the gabbronorites in Figure 4.1 could be attributed to variable contamination of the Qullinaaraaluk intrusion by the surrounding granitoids during ascent or emplacement (Milidragovic et al., 2014). When considering the initial $\epsilon^{143}\text{Nd}$ of the Qullinaaraaluk intrusion, Milidragovic et al. (2014) noted that the initial $\epsilon^{143}\text{Nd}$ decreased with increasing SiO_2 content and degree of REE fractionation, and interpreted the negative $\epsilon^{143}\text{Nd}$ to reflect contamination from the surrounding granitoid crust. Therefore, the offset of the gabbronorites could reflect greater degrees of contamination from granitoids during emplacement. The gabbronorites are found on the margins of the zoned intrusion. They are the most evolved rocks and therefore, assuming they were the last unit to crystallize, their magmas would have been in contact with the warm granitoid crust

for the longest amount of time. This could have facilitated contamination by the granitoid crust and modified their Nd isotopic composition, which would explain why the initial Nd isotopic composition of the gabbronorites is different from the other lithologies of the intrusion.

Removing the gabbronorite samples from the Sm-Nd isochron yields an age of 2706 ± 29 Ma (Figure 4.2), which is consistent with the U-Pb zircon ages obtained through U-Pb zircon dating of the Q-Suite gabbronorites (Simard, 2008; Milidragovic and Francis, 2014).

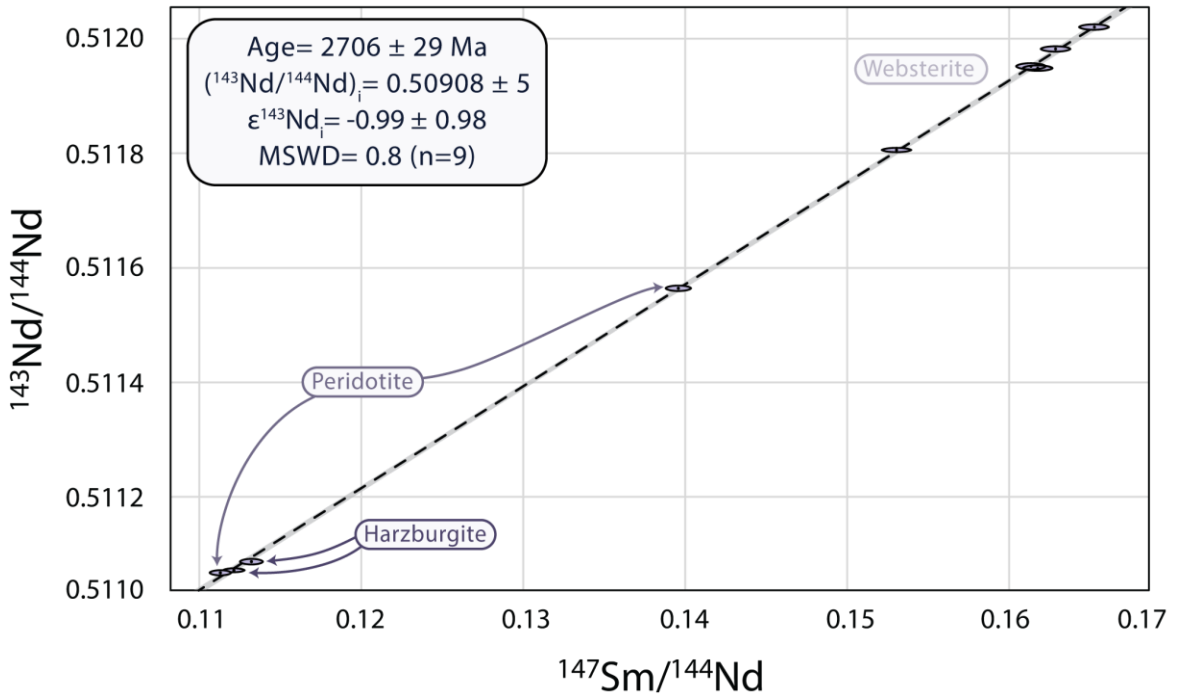


Figure 4.2: $^{147}\text{Sm}/^{144}\text{Nd}$ vs. $^{143}\text{Nd}/^{144}\text{Nd}$ isochron excluding the gabbronorites. Isochron age, initial Nd isotope composition, and MSWD was obtained using Vermeesch (2018). Gray area indicates error on the line. Ellipsoids indicate 2SD error on the points, calculated by Isoplot. Gray area indicates error on the line.

Furthermore, the MSWD of this refined isochron is 0.8, supporting the fact that the harzburgite, peridotite, and websterite samples composing this regression are co-

genetic and that their Nd isotopic composition has not been disturbed since their formation. We therefore consider this Sm-Nd isochron age to reflect the crystallization age of the Qullinaaraaluk intrusion. This new isochron age yields an the initial $^{143}\text{Nd}/^{144}\text{Nd}$ of 0.50908 ± 5 , corresponding to a $\epsilon^{143}\text{Nd}_{2706}$ of -0.99 ± 0.98 .

An $\epsilon^{143}\text{Nd}_{2706}$ of -0.99 , as suggested by the ^{147}Sm - ^{143}Nd isochron (Figure 4.2), would imply a mantle source for the Qullinaaraaluk intrusion significantly more enriched than the depleted mantle at 2.7 Ga ($\epsilon^{143}\text{Nd}_{2700} \sim +4.5$; DePaolo, 1980). However, in addition to the negative initial $\epsilon^{143}\text{Nd}$, all Qullinaaraaluk units show enrichments in LREE and Pb and depletions in Nb and Ta, which was interpreted by Milidragovic et al. (2014) to be caused by variable contamination of the entire intrusion by granitoids (Figure 3.4). The contamination of the harzburgites and peridotites was estimated by Milidragovic et al. (2014) to be the result of 3-10% infiltration of anatectic granitoid melts. Because the isochron of Figure 4.3 strongly suggests that the ^{147}Sm - ^{143}Nd system remained closed after the crystallization of the co-genetic Qullinaaraaluk rocks, we argue that contamination with felsic crust most likely occurred during the emplacement of the Qullinaaraaluk primitive magma, before its fractionation. This contaminated magma would then differentiate into the different Qullinaaraaluk units, which would still have the same initial isotopic composition at the time of their formation. By considering the Sm-Nd isotopic composition of the Qullinaaraaluk rocks to be a mix between their original composition and 3-10% of the granitoid crust, we can determine the isotopic composition of the mantle source of the Qullinaaraaluk intrusion prior to contamination. The initial Nd

isotope compositions of the mantle source of the Qullinaaraaluk intrusion prior to crustal contamination are obtained using the following equation:

$$(1.5) \quad \left(\frac{^{143}\text{Nd}}{^{144}\text{Nd}}\right)_b = \left(\frac{^{143}\text{Nd}}{^{144}\text{Nd}}\right)_{\text{Mix}} - \frac{Xa \times \left[\left(\frac{^{143}\text{Nd}}{^{144}\text{Nd}}\right)_a - \left(\frac{^{143}\text{Nd}}{^{144}\text{Nd}}\right)_b\right]}{\left(Xb \times \frac{[\text{Nd}]_b}{[\text{Nd}]_a}\right) + Xa}$$

Where 'a' represents the isotopic composition of the granitoid crust at 2706 Ma, 'b' represents the original isotopic composition of Qullinaaraaluk intrusion at 2706 Ma, 'Mix' represents the measured isotopic composition at 2706 Ma, 'X' represents the fraction of the end member in the mixture (where $Xa + Xb = 1$), and [Nd] represents the Nd concentration.

Harzburgite samples QK-004 and QK-010 along with peridotite samples QK-013 and QK-016 were chosen to represent the Qullinaaraaluk rocks, as the harzburgites and peridotites are interpreted by Milidragovic et al. (2014) to be affected by 3-10% contamination. Due to the absence of chilled margins between the intrusion and the surrounding granitoids and the similar $\epsilon^{143}\text{Nd}$ observed in the Qullinaaraaluk intrusion and granodiorites, it is probable that the isotopic composition of the granodiorites proximal to the intrusion experienced open-system behaviour with the intrusion during their emplacement. The geochemical composition of several granodiorites flanking Q-Suite intrusions were explained by binary mixing between the mafic-ultramafic intrusions and the granitoid crust (Milidragovic and Francis, 2014). Due to the high probability that the initial $\epsilon^{143}\text{Nd}$ of the surrounding granodiorites was modified during the intrusion's emplacement, a granitoid from the NESP analyzed by O'Neil and Carlson (2017) with an initial $\epsilon^{143}\text{Nd}$ of -13 (tonalite 2003031499) was selected as the potential contaminant (Appendix B, Table B3). By selecting a tonalite with a very low initial $\epsilon^{143}\text{Nd}$, which suggests a highly enriched source relative to the CHUR, we are able to consider

contamination from the most enriched material present in the region at 2.706 Ga. The resulting initial $\epsilon^{143}\text{Nd}$ following the removal of contamination are presented in Table 7.

Table 7: Initial ϵNd_i and time integrated $^{147}\text{Sm}/^{144}\text{Nd}$ calculated before and after removing 3% to 10% mixing with granitoid crust

Sample	ϵNd_i	ϵNd_i removing 3% mixing	ϵNd_i removing 10% mixing
QK-004	-0.98	-0.18	1.53
QK-010	-1.21	-0.40	1.31
QK-013	-1.31	-0.51	1.18
QK-016	-1.15	-0.47	1.01
Average	-1.16	-0.39	1.26
Time integrated $^{147}\text{Sm}/^{144}\text{Nd}$	0.1912	0.1944	0.2012

The removal of contamination increased the average initial $\epsilon^{143}\text{Nd}$ from -1.16 to -0.39 and +1.26, for respectively 3% and 10% contamination. This suggests that the Qullinaaraaluk mantle source had a slightly subchondritic to superchondritic Nd isotopic composition at the time of emplacement.

Using these initial $^{143}\text{Nd}/^{144}\text{Nd}$ values, we can estimate the time-integrated $^{147}\text{Sm}/^{144}\text{Nd}$ of the mantle reservoir to be between 0.1944 and 0.2012 (Table 7), suggesting that the mantle source of the Qullinaaraaluk magmas was more enriched in incompatible trace elements compared to the upper depleted mantle.

4.2 Constraints on the Mantle Source from the Short-lived ^{146}Sm - ^{142}Nd System

Due to the short half-life of ^{146}Sm (103 Ma), the ^{146}Sm - ^{142}Nd system is a powerful tool to trace early silicate differentiation. Any event producing Sm-Nd fractionation while ^{146}Sm was still extant (i.e., before ~4.1 Ga) creates depleted and enriched reservoirs with respectively high and low $^{142}\text{Nd}/^{144}\text{Nd}$ ratios. Goldstein and Francis (2008) proposed that the mantle source of the ferropicrites could have formed during the crystallization of a

deep Hadean magma ocean. The crystal-liquid fractionation associated with the solidification of a magma ocean would be capable of creating a reservoir of Fe-rich peridotite through an olivine floatation cumulate. A source created by such an early event would be characterized by anomalies in $\mu^{142}\text{Nd}$.

Early differentiation events have been recorded in mantle-derived rocks from SW Greenland and NE Canada, evidenced by well-resolved negative and positive ^{142}Nd anomalies of -18 to +20 ppm (e.g. O'Neil et al., 2012; Rizo et al., 2011; Morino et al., 2017). The samples from the Qullinaaraaluk intrusion analyzed here yield an average $\mu^{142}\text{Nd}$ value of -0.4, which cannot be resolved from the terrestrial Nd standard within a 5 ppm precision (Figure 3.9, average $\mu^{142}\text{Nd} = -0.4 \pm 5.5$). Our results, therefore, suggest that the mantle source of the Qullinaaraaluk ferropicrites did not record Sm/Nd fractionation during the Hadean era, which is inconsistent for a source formed during the crystallization of an early magma ocean. Therefore, the ^{142}Nd results from this thesis do not support a mantle source formed by a Hadean magma ocean.

An alternative hypothesis for the origin of the subalkaline ferropicrite source was proposed by Milidragovic et al. (2014), who observed similarities between the FeO_{TOT} and MgO contents of the parental magmas of the Q-Suite intrusion, the Martian mantle, asteroid Vesta-4, and L5 ordinary chondrites. Similarities between the mineralogy and geochemical composition of ferropicrites and shergottites (basaltic rocks composing the Martian crust) were also observed by Filiberto (2008). Milidragovic et al. (2014) and Milidragovic and Francis (2016) therefore proposed a model in which the Fe-rich peridotite mantle source of Neoproterozoic subalkaline ferropicrites could have formed from

the late-accretion of extraterrestrial material, creating an Fe-enriched domain in the upper mantle. This extraterrestrial material has $^{142}\text{Nd}/^{144}\text{Nd}$ ratios that differ from the standard terrestrial composition. Intermediate and depleted Martian shergottites are characterized by positive $\mu^{142}\text{Nd}$ values over +60, while enriched shergottites are characterized by well-resolved negative $\mu^{142}\text{Nd}$ values (Borg et al., 2016; Debaille et al., 2007; Kruijer et al., 2017). Ordinary chondrites and achondrites are characterized by negative $\mu^{142}\text{Nd}$ values (Boyet and Carlson, 2005; Andreasen and Sharma, 2006; Burkhardt et al., 2016; Saji et al., 2020; Render and Brennecka, 2020; Frossard et al., 2021). The absence of $\mu^{142}\text{Nd}$ variations in the Qullinaaraaluk intrusion suggests that its mantle source did not form from the accretion of extraterrestrial material. It should be noted, however, that $\mu^{142}\text{Nd}$ may not represent the ideal tracer of extraterrestrial material. Late accretion (sometimes referred to as the “late veneer”), as estimated by highly siderophile element abundances in the upper mantle, is thought to represent maximum ~ 0.5 wt% of the Earth’s mass (roughly the current mass of the Earth’s crust; Walker, 2009). Given the mass of late accretion, the range of $^{142}\text{Nd}/^{144}\text{Nd}$ variations of extraterrestrial materials (Figure 4.4) and the similar Nd concentrations of terrestrial rocks and the putative extraterrestrial materials, a large amount of extraterrestrial material would be required to modify the $\mu^{142}\text{Nd}$ of a terrestrial reservoir.

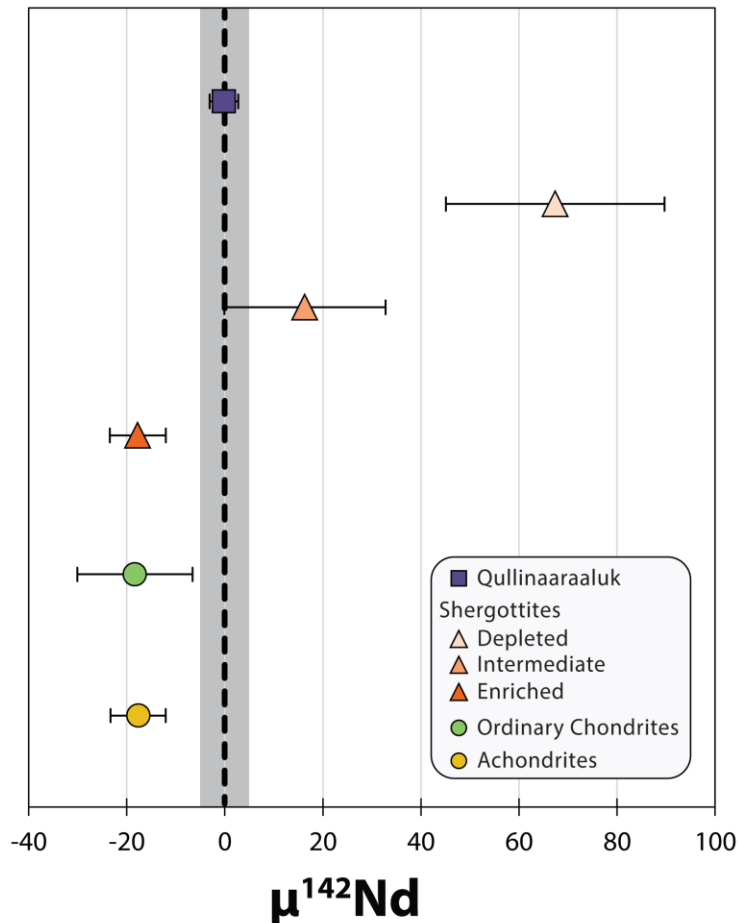


Figure 4.3: Comparison between $\mu^{142}\text{Nd}$ for Qullinaaraaluk and extraterrestrial material. Symbols represent average compositions with 2SD. Values for Shergottites from Borg et al. (2016), Debaille et al. (2007), and Kruijer et al. (2017). Values for ordinary chondrites from Boyet and Carlson (2005), and Andreasen and Sharma (2006). Values for achondrites from Burkhardt et al. (2016), Saji et al. (2020), Render and Brennecka (2020), and Frossard et al. (2021).

4.3 The Source of Neoproterozoic Ferropicrites vs. Other Contemporaneous Mantle-Derived Rocks

Ferropicrites have historically been misidentified as Fe-enriched Al-depleted komatiites, due to their high Mg content and temporal-spatial association with komatiitic rocks.

However, at a given MgO, ferropicrites are more enriched in Fe and depleted in Al than komatiites, thus demanding a separate mantle source (Stone et al., 1995). Figure 4.4

shows differences between the time-integrated $^{147}\text{Sm}/^{144}\text{Nd}$ compositions of the

Qullinaaraaluk intrusion obtained here and those previously reported for and Archean komatiites and basalts (Blicher-Toft and Puchtel, 2010). The time-integrated ^{147}Sm - ^{144}Nd ratios of the subalkaline ferropicrite source clearly differs from the source of Archean komatiites, providing geochemical evidence that ferropicrites formed from a mantle source distinct from that of the komatiites.

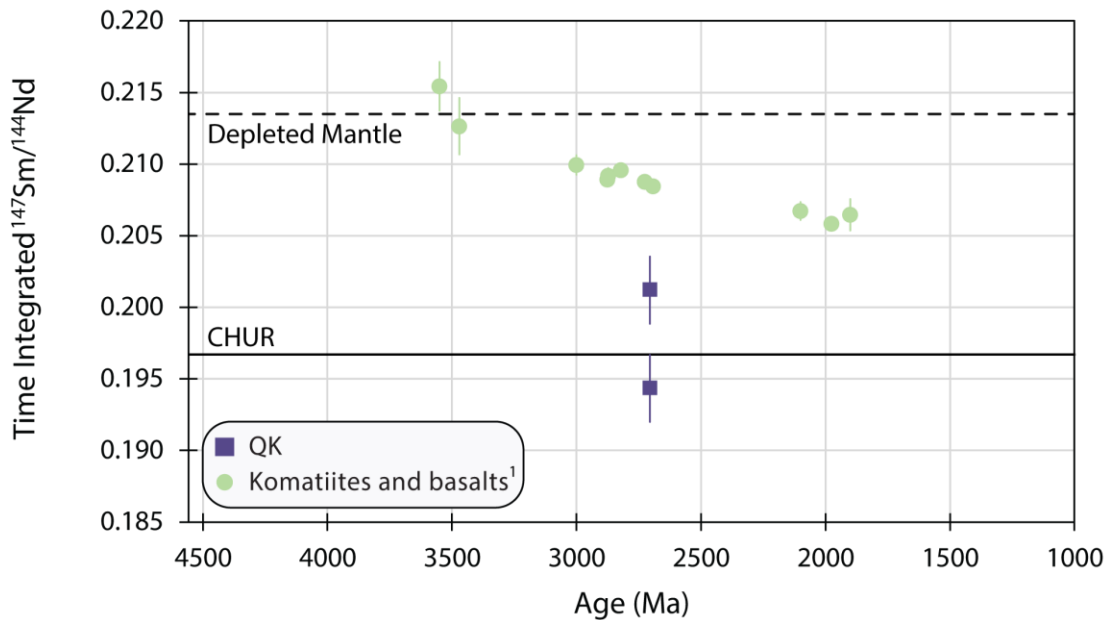


Figure 4.4: Time integrated $^{147}\text{Sm}/^{144}\text{Nd}$ plotted against age for the Qullinaaraaluk intrusion and Archean komatiites and basalts. The two data points for the Qullinaaraaluk intrusion represent the different results for removal of 3% and 10% contamination (See Table 7). Vertical error bar on the Qullinaaraaluk intrusion estimated using error from isochron (¹Blicher-Toft and Puchtel, 2010).

As discussed in Section 1.12, significant differences were identified in the geochemical characteristics of alkaline and subalkaline ferropicrites. Neoproterozoic alkaline ferropicrites have LREE enrichments, fractionated HREE profiles, low Sc contents, Ni-enrichments, and low concentrations of Al_2O_3 and Sc (Figure 1.3). These geochemical characteristics have been used to suggest derivation from a garnet-pyroxenite mantle source. Neoproterozoic subalkaline ferropicrites have parental magmas with flat to depleted

LREE, unfractionated HREE, Ni-depletions, and higher concentrations of Al_2O_3 and Sc relative to the alkaline ferropicrites (Figure 1.3). This suggests derivation from a peridotitic mantle source (Milidragovic and Francis, 2016). The results from short- and long-lived Sm-Nd isotope systems acquired here can be used to provide additional constraints on the source of subalkaline ferropicrites and better establish if it is different from the source of the alkaline ferropicrites.

To date, only 3 studies have performed ^{142}Nd analyses in ferropicrites: Landon-Browne (2019), Puchtel et al. (2018), and the study presented here. The ^{142}Nd results from these three studies are compared in Figure 4.8. While none of the ferropicrite rocks measured showed resolvable $\mu^{142}\text{Nd}$ anomalies from the terrestrial mantle, the average Qullinaaraaluk intrusion's $-0.4 \mu^{142}\text{Nd}$ seems to contrast with the consistently, slightly negative $\mu^{142}\text{Nd}$ obtained for two different suites of Neoproterozoic alkaline ferropicrites ($\mu^{142}\text{Nd} = -2.0 \pm 3.9$, Landon-Browne, 2019; $\mu^{142}\text{Nd} = -3.8 \pm 2.8$, Puchtel et al., 2018; Figure 4.5). Here we evaluate the possibility that the source of these rocks is different in terms of $\mu^{142}\text{Nd}$ and the implications of this difference.

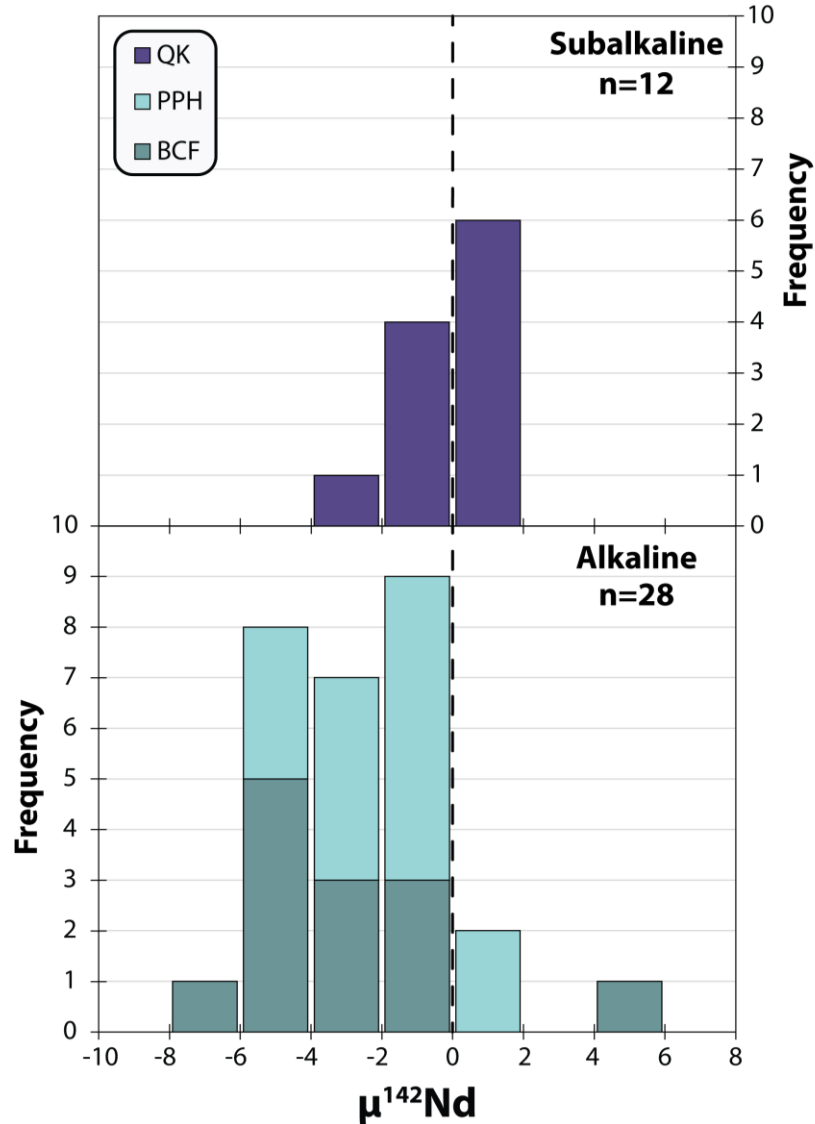


Figure 4.5: Comparison of $\mu^{142}\text{Nd}$ for subalkaline and alkaline ferropicrites. Boston Creek Ferropicrite (BCF) data from Puchtel et al., 2018. Pulpwood-Playter Harbour (PPH) data from Landon-Browne, 2019.

The initial $\epsilon^{143}\text{Nd}$ of the subalkaline ferropicrites, corrected for granitoid crustal contamination (see section 4.1), is near-chondritic and falls within error of the initial $\epsilon^{143}\text{Nd}$ of the alkaline ferropicrites ($\epsilon^{143}\text{Nd}_i = +2.3 \pm 1.0$, Landon-Browne, 2019; $\epsilon^{143}\text{Nd}_i = +2.3 \pm 1.0$, Puchtel et al., 2018; Figure 4.6). As such, both the alkaline and subalkaline Neoproterozoic ferropicrites can be considered to have chondritic to slightly superchondritic initial $\epsilon^{143}\text{Nd}$ (Figure 4.6). While the geochemical differences between alkaline and

subalkaline ferropicrites suggest they have distinct petrogeneses, the similar initial $\epsilon^{143}\text{Nd}$ values may suggest a similar mantle source. Several models have been proposed to explain the origin of the high Fe contents of ferropicrites. Only the petrogenesis models that can be evaluated by the Sm-Nd isotopic system will be discussed here, for further discussion on ferropicrites please refer to section 1.1.

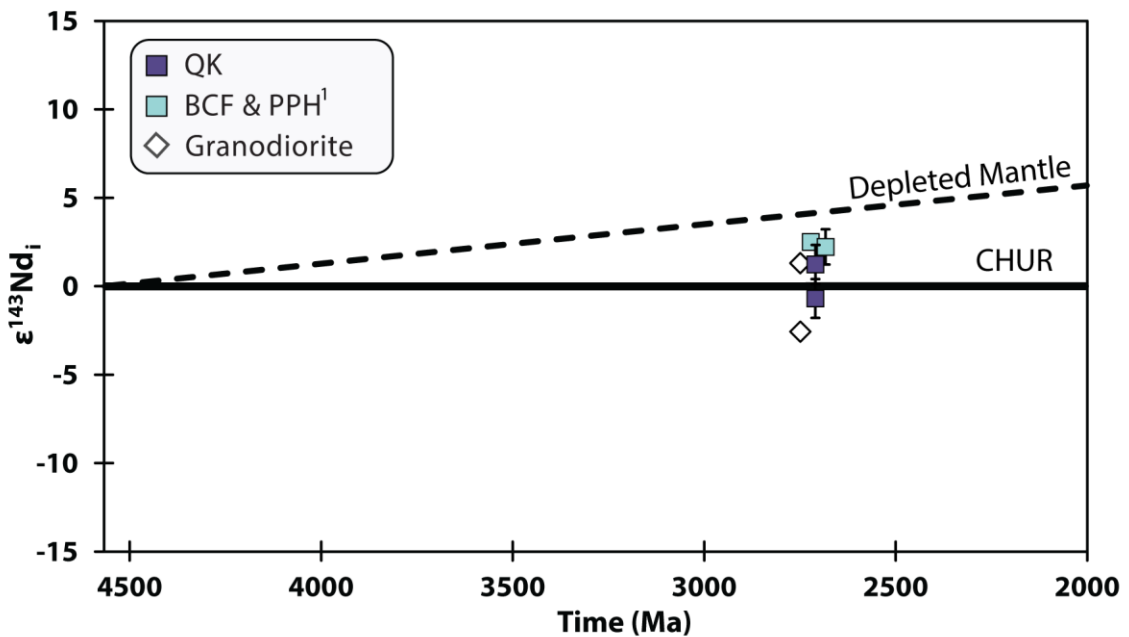


Figure 4.6: Initial $\epsilon^{143}\text{Nd}$ of harzburgite and peridotite samples corrected for contamination. Lower point represents 3% correction, upper point represents 10% correction. Vertical error bar taken from error on $\epsilon^{143}\text{Nd}$ from isochron. Granitoids and alkaline ferropicrites (BCF & PPH) plotted for comparison (¹Puchtel et al., 2018; Landon-Browne, 2019; ²O'Neil and Carlson, 2017).

Models in which ferropicrites are derived from a garnet-pyroxenite source are well-supported by geochemical and experimental data (Gibson, 2002; Tuff et al., 2005; Jennings, 2016). The garnet-pyroxenite is formed by metasomatism of mantle peridotite by rising mantle plumes with eclogitic components (Gibson, 2002; Jennings, 2016). While a garnet-bearing source cannot explain the geochemical features of subalkaline

ferropicrites (Milidragovic and Francis, 2016), experiments by Tuff et al. (2005) show that at pressures below 2 GPa the garnet-pyroxenite becomes an olivine-pyroxenite. This could theoretically produce the olivine-bearing geochemical features of the Qullinaaraaluk mantle source. In this case, Neoproterozoic alkaline and subalkaline ferropicrites could be formed from a common mantle source undergoing melting at different pressures. This model would be supported by the similar $\epsilon^{143}\text{Nd}$ values observed in the alkaline and subalkaline ferropicrites, but cannot explain the difference in $\mu^{142}\text{Nd}$ between the alkaline and subalkaline ferropicrites (Figure 4.6).

Alternatively, to explain the relationship between alkaline and subalkaline ferropicrites, Milidragovic and Francis (2016) proposed that while the source of the subalkaline ferropicrites is an Fe-rich peridotite, the source of the alkaline ferropicrites is a garnet-pyroxenite formed by the metasomatism of the Fe-rich peridotite. In this interpretation, given the superchondritic $\epsilon^{143}\text{Nd}$ of the alkaline ferropicrites indicating a long-term LREE depleted mantle reservoir (Milidragovic and Francis, 2016, Stone et al., 1995), the reservoir's enrichment in incompatible trace elements would need to occur shortly before emplacement, before their $^{143}\text{Nd}/^{144}\text{Nd}$ evolves to a lower ratio. Considering the similarities observed between the $\epsilon^{143}\text{Nd}$ of the Qullinaaraaluk intrusion and the alkaline ferropicrites, this study finds this model to be plausible. Additionally, this scenario potentially provides a process to account for the $\mu^{142}\text{Nd}$ discrepancy between the alkaline and subalkaline ferropicrites. The slightly negative $\mu^{142}\text{Nd}$ of the alkaline ferropicrites could have been imparted by the material that converted the Fe-rich peridotite to garnet-pyroxenite, explaining the absence of $\mu^{142}\text{Nd}$ anomaly in the

Qullinaaraaluk intrusion. However, this would require the material to have a low $^{142}\text{Nd}/^{144}\text{Nd}$, possibly suggesting the involvement of Hadean crust in the source of the alkaline ferropicrites. Regardless of the origin of the slight negative $\mu^{142}\text{Nd}$ values of the alkaline ferropicrites, our results show that no Hadean component or extraterrestrial material is required for the formation of the Neoproterozoic Qullinaaraaluk ferropicrites.

Chapter 5: Conclusion

The origin of the Fe-rich source of ferropicrites is still not fully resolved. The geochemical and isotopic differences between Proterozoic and Archean ferropicrites suggest that there could be several petrogenetic processes involved in the formation of these Fe-rich magmas. The mafic-ultramafic Qullinaaraaluk intrusion can provide insights into the composition and the nature of Fe-enriched mantle domains from which Neoproterozoic subalkaline ferropicrites were derived. The $^{146-147}\text{Sm}-^{142-143}\text{Nd}$ results from this study allow us to place important geochronological and isotopic constraints on the Qullinaaraaluk ferropicrites and their mantle source. The long-lived $^{147}\text{Sm}-^{143}\text{Nd}$ system confirmed the Neoproterozoic age of the intrusion with an isochron supporting a crystallization age of 2706 ± 29 Ma. Accounting for some extent of crustal contamination, the initial $\epsilon^{143}\text{Nd}$ values range between -0.39 and +1.26, suggestive of a near-chondritic mantle source. This contrasts with most other Archean mantle-derived magmas, such as komatiites and basalts, that commonly show higher initial $\epsilon^{143}\text{Nd}$ values that are similar to the depleted mantle. This supports a distinct and more enriched mantle source for the Archean subalkaline ferropicrites. Results from the short-lived $^{146}\text{Sm}-^{142}\text{Nd}$ system show that the

Qullinaaraaluk intrusion exhibits $\mu^{142}\text{Nd}$ values indistinguishable from the Nd terrestrial standards, indicating that no Hadean-formed component was included in the Qullinaaraaluk mantle source. This precludes an Fe-rich mantle source formed through the crystallization of a Hadean magma ocean or the incorporation of extraterrestrial material into the mantle source. Despite the fact that the geochemistry of alkaline and subalkaline ferropicrites suggests they were formed through distinct petrogenetic processes, the initial $\epsilon^{143}\text{Nd}$ of the subalkaline Qullinaaraaluk intrusion that is comparable to that of the southern Superior Province alkaline ferropicrites indicates that their Fe-rich mantle sources may have a similar origin. Slight unresolvable $\mu^{142}\text{Nd}$ anomalies detected in alkaline ferropicrites further suggest that although they may share a similar source, alkaline and subalkaline ferropicrites have not formed through identical processes. Based on this study, the model that best fits the Sm-Nd systematics of the Neoproterozoic ferropicrites is that of a common Fe-rich peridotite source with near-chondritic $\epsilon^{143}\text{Nd}$. Direct melting of this Fe-rich peridotite source would have created the subalkaline ferropicrites, while the metasomatization of this source, possibly by material with negative $\mu^{142}\text{Nd}$ but a similar $\epsilon^{143}\text{Nd}$ to the peridotite, would convert the peridotite to garnet-pyroxenite which would then create the alkaline Neoproterozoic ferropicrites.

While this study does not support an extraterrestrial component in the source of the Qullinaaraaluk intrusion from a ^{142}Nd perspective, further investigation into the ^{182}Hf - ^{182}W compositions of the subalkaline ferropicrites could provide clearer evidence for the involvement, or the lack thereof, of extraterrestrial material in the formation of the Qullinaaraaluk intrusion. Variations in $\mu^{182}\text{W}$ values in chondrites or the Martian mantle

are up to an order of magnitude higher than $\mu^{142}\text{Nd}$ values (e.g. Kleine et al., 2009; Kleine and Walker, 2017). Additionally, the concentration of W in chondrites is significantly higher than that of the mantle, so the input of extraterrestrial material to a terrestrial mantle reservoir would clearly be recorded by ^{182}W isotopes. High-precision ^{182}W isotopic analyses of the Qullinaaraaluk intrusion are currently in progress, and will help clarify the relationship between the mantle source of the intrusion and extraterrestrial material.

References

- Andreasen, R., & Sharma, M. (2006). Solar nebula heterogeneity in p-process samarium and neodymium isotopes. *Science*, *314*(5800), 806-809.
- Ballmer, M. D., Lourenço, D. L., Hirose, K., Caracas, R., & Nomura, R. (2017). Reconciling magma-ocean crystallization models with the present-day structure of the Earth's mantle. *Geochemistry, Geophysics, Geosystems*, *18*(7), 2785-2806.
- Bédard, J. H., & Harris, L. B. (2014). Neoproterozoic disaggregation and reassembly of the Superior craton. *Geology*, *42*(11), 951-954.
- Bédard, J. H. (2018). Stagnant lids and mantle overturns: Implications for Archean tectonics, magmagenesis, crustal growth, mantle evolution, and the start of plate tectonics. *Geoscience Frontiers*, *9*(1), 19-49.
- Blichert-Toft, J., & Puchtel, I. S. (2010). Depleted mantle sources through time: evidence from Lu–Hf and Sm–Nd isotope systematics of Archean komatiites. *Earth and Planetary Science Letters*, *297*(3-4), 598-606.
- Boily, M., Leclair, A., Maurice, C., Bédard, J. H., & David, J. (2009). Paleo-to Mesoproterozoic basement recycling and terrane definition in the Northeastern Superior Province, Québec, Canada. *Precambrian Research*, *168*(1-2), 23-44.
- Bouvier, A., Vervoort, J. D., & Patchett, P. J. (2008). The Lu–Hf and Sm–Nd isotopic composition of CHUR: constraints from unequilibrated chondrites and implications for the bulk composition of terrestrial planets. *Earth and Planetary Science Letters*, *273*(1-2), 48-57.
- Borg, L. E., Brennecka, G. A., & Symes, S. J. (2016). Accretion timescale and impact history of Mars deduced from the isotopic systematics of martian meteorites. *Geochimica et Cosmochimica Acta*, *175*, 150-167.
- Boyet, M., & Carlson, R. W. (2005). ^{142}Nd evidence for early (> 4.53 Ga) global differentiation of the silicate Earth. *Science*, *309*(5734), 576-581.
- Burkhardt, C., Borg, L. E., Brennecka, G. A., Shollenberger, Q. R., Dauphas, N., & Kleine, T. (2016). A nucleosynthetic origin for the Earth's anomalous ^{142}Nd composition. *Nature*, *537*(7620), 394-398.
- Cameron, E. M., & Baumann, A. (1972). Carbonate sedimentation during the Archean. *Chemical Geology*, *10*(1), 17-30.
- Condie, K. C., Aster, R. C., & Van Hunen, J. (2016). A great thermal divergence in the mantle beginning 2.5 Ga: Geochemical constraints from greenstone basalts and komatiites. *Geoscience Frontiers*, *7*(4), 543-553.
- Cottaar, S., & Lekic, V. (2016). Morphology of seismically slow lower-mantle structures. *Geophysical Supplements to the Monthly Notices of the Royal Astronomical Society*, *207*(2), 1122-1136.

- Debaille, V., Brandon, A. D., Yin, Q. Z., & Jacobsen, B. (2007). Coupled ^{142}Nd – ^{143}Nd evidence for a protracted magma ocean in Mars. *Nature*, *450*(7169), 525-528.
- DePaolo, D. J. (1980). Crustal growth and mantle evolution: inferences from models of element transport and Nd and Sr isotopes. *Geochimica et Cosmochimica Acta*, *44*(8), 1185-1196.
- Faure, S., Daigneault, R., & Godey, S. (2008). Upper mantle architecture of the Archean Superior Province and the implication for the dimension, orientation, metamorphism, and mineralization of the greenstone belts. In *Geological Association of Canada-Mineralogical Association of Canada Joint Annual Meeting, Program with Abstracts, Québec* (p. 55).
- Francis, D., Ludden, J., Johnstone, R., & Davis, W. (1999). Picrite evidence for more Fe in Archean mantle reservoirs. *Earth and Planetary Science Letters*, *167*(3-4), 197-213.
- Frossard, P., Guo, Z., Spencer, M., Boyet, M., & Bouvier, A. (2021). Evidence from achondrites for a temporal change in Nd nucleosynthetic anomalies within the first 1.5 million years of the inner solar system formation. *Earth and Planetary Science Letters*, *566*, 116968.
- Garçon, M., Boyet, M., Carlson, R. W., Horan, M. F., Auclair, D., & Mock, T. D. (2018). Factors influencing the precision and accuracy of Nd isotope measurements by thermal ionization mass spectrometry. *Chemical Geology*, *476*, 493-514.
- Garnero, E. J., McNamara, A. K., & Shim, S. H. (2016). Continent-sized anomalous zones with low seismic velocity at the base of Earth's mantle. *Nature Geoscience*, *9*(7), 481-489.
- Hanski, E. J., & Smolkin, V. F. (1989). Pechenga ferropicrites and other early Proterozoic picrites in the eastern part of the Baltic Shield. *Precambrian Research*, *45*(1-3), 63-82.
- Hanski, E.J., Huhma, H., Smolkin, V. F., & Vaasjoki, M.. (1990). The age of the ferropicritic volcanics and comagmatic Ni-bearing intrusions at Pechenga, Kola Peninsula, USSR. *Bull. Geol. Soc. Finl*, *62*(2), 123-133.
- Hanski, E. J., & Smolkin, V. F. (1995). Iron-and LREE-enriched mantle source for early Proterozoic intraplate magmatism as exemplified by the Pechenga ferropicrites, Kola Peninsula, Russia. *Lithos*, *34*(1-3), 107-125.
- Harris, L. B., & Bédard, J. H. (2014). Crustal evolution and deformation in a non-plate-tectonic Archean Earth: comparisons with Venus. In *Evolution of Archean crust and early life* (pp. 215-291). Springer, Dordrecht.
- Heinonen, J. S., & Luttinen, A. V. (2008). Jurassic dikes of Vestfjella, western Dronning Maud Land, Antarctica: Geochemical tracing of ferropicrite sources. *Lithos*, *105*(3-4), 347-364.
- Herzberg, C., Condie, K., & Korenaga, J. (2010). Thermal history of the Earth and its petrological expression. *Earth and Planetary Science Letters*, *292*(1-2), 79-88.

- He, D., Liu, Y., Chen, C., Foley, S. F., & Ducea, M. N. (2020). Oxidization of the mantle caused by sediment recycling may contribute to the formation of iron-rich mantle melts. *Science Bulletin*, *65*(7), 519-521.
- Jackson, C. R., Bennett, N. R., Du, Z., Cottrell, E., & Fei, Y. (2018). Early episodes of high-pressure core formation preserved in plume mantle. *Nature*, *553*(7689), 491-495.
- Jakobsen, J. K., Veksler, I. V., Tegner, C., & Brooks, C. K. (2005). Immiscible iron-and silica-rich melts in basalt petrogenesis documented in the Skaergaard intrusion. *Geology*, *33*(11), 885-888.
- Jennings, E. S., Holland, T. J., Shorttle, O., Maclennan, J., & Gibson, S. A. (2016). The composition of melts from a heterogeneous mantle and the origin of ferropicrite: application of a thermodynamic model. *Journal of Petrology*, *57*(11-12), 2289-2310.
- Jochum, K. P., Willbold, M., Raczek, I., Stoll, B., & Herwig, K. (2005). Chemical Characterisation of the USGS Reference Glasses GSA-1G, GSC-1G, GSD-1G, GSE-1G, BCR-2G, BHVO-2G and BIR-1G Using EPMA, ID-TIMS, ID-ICP-MS and LA-ICP-MS. *Geostandards and Geoanalytical Research*, *29*(3), 285-302.
- Jochum, K. P., Weis, U., Schwager, B., Stoll, B., Wilson, S. A., Haug, G. H., ... & Enzweiler, J. (2016). Reference values following ISO guidelines for frequently requested rock reference materials. *Geostandards and Geoanalytical Research*, *40*(3), 333-350.
- Kellogg, L. H., Hager, B. H., & van der Hilst, R. D. (1999). Compositional stratification in the deep mantle. *Science*, *283*(5409), 1881-1884.
- Kitayama, Y. C., & Francis, D. (2014). Iron-rich alkaline magmatism in the Archean Wawa greenstone belts (Ontario, Canada). *Precambrian Research*, *252*, 53-70.
- Kleine, T., Touboul, M., Bourdon, B., Nimmo, F., Mezger, K., Palme, H., ... & Halliday, A. N. (2009). Hf–W chronology of the accretion and early evolution of asteroids and terrestrial planets. *Geochimica et Cosmochimica Acta*, *73*(17), 5150-5188.
- Kleine, T., & Walker, R. J. (2017). Tungsten isotopes in planets. *Annual review of earth and planetary sciences*, *45*, 389-417.
- Kruijer, T. S., Kleine, T., Borg, L. E., Brennecka, G. A., Irving, A. J., Bischoff, A., & Agee, C. B. (2017). The early differentiation of Mars inferred from Hf–W chronometry. *Earth and Planetary Science Letters*, *474*, 345-354.
- Labrosse, S., Hernlund, J. W., & Coltice, N. (2007). A crystallizing dense magma ocean at the base of the Earth's mantle. *Nature*, *450*(7171), 866-869.
- Landon-Browne, A. (2019). Combined Short-lived (^{182}W , ^{142}Nd) and Long-Lived (^{147}Sm - ^{143}Nd) Isotope Study on Rocks from the Pulpwood-Playter Harbour Sequence (Wawa Subprovince): Constraints on the Mantle Source of Neoproterozoic Ferropicrites. *Masters Thesis, Ottawa University*, 128 p.
- Li, Z., Chen, B., Wei, C., Wang, C., & Han, W. (2015). Provenance and tectonic setting of the Paleoproterozoic metasedimentary rocks from the Liaohe Group, Jiao-Liao-Ji Belt,

- North China Craton: insights from detrital zircon U–Pb geochronology, whole-rock Sm–Nd isotopes, and geochemistry. *Journal of Asian Earth Sciences*, 111, 711–732.
- Gibson, S. A., Thompson, R. N., & Dickin, A. P. (2000). Ferropicrites: geochemical evidence for Fe-rich streaks in upwelling mantle plumes. *Earth and Planetary Science Letters*, 174(3–4), 355–374.
- Gibson, S. A. (2002). Major element heterogeneity in Archean to Recent mantle plume starting-heads. *Earth and Planetary Science Letters*, 195(1–2), 59–74.
- Goldstein, S. B., & Francis, D. (2008). The petrogenesis and mantle source of Archean ferropicrites from the Western Superior Province, Ontario, Canada. *Journal of Petrology*, 49(10), 1729–1753.
- Gosselin, C., Simard, M., & David, J. (2002). *Geology of the Lacs Des Loups Marins (34A)*. Géologie Québec [Ressources naturelles].
- Green, J. C., & Schulz, K. J. (1977). Iron-rich basaltic komatiites in the early Precambrian Vermilion District, Minnesota. *Canadian Journal of Earth Sciences*, 14(10), 2181–2192.
- Herzberg, C., Condie, K., & Korenaga, J. (2010). Thermal history of the Earth and its petrological expression. *Earth and Planetary Science Letters*, 292(1–2), 79–88.
- Kitayama, Y. C., & Francis, D. (2014). Iron-rich alkaline magmatism in the Archean Wawa greenstone belts (Ontario, Canada). *Precambrian Research*, 252, 53–70.
- Leclair, A. (2008). Contexte géologique régional du nord-est de la Province du Supérieur. *Synthese du Nord-Est de la Province du Supérieur*. *Ministère de Ressources Naturelles et de la Faune, MM2008-2*, 13–22.
- Maurice, C., David, J., Bédard, J. H., & Francis, D. (2009). Evidence for a widespread mafic cover sequence and its implications for continental growth in the Northeastern Superior Province. *Precambrian Research*, 168(1–2), 45–65.
- Milidragovic, D., & Francis, D. (2014). Ferropicrite-driven reworking of the Ungava craton and the genesis of Neoarchean pyroxene-granitoids. *Earth and Planetary Science Letters*, 386, 138–148.
- Milidragovic, D., Francis, D., Weis, D., & Constantin, M. (2014). Neoarchean (c. 2.7 Ga) Plutons of the Ungava Craton, Québec, Canada: Parental Magma Compositions and Implications for Fe-rich Mantle Source Regions. *Journal of Petrology*, 55(12), 2481–2512.
- Milidragovic, D., & Francis, D. (2016). Ca. 2.7 Ga ferropicritic magmatism: A record of Fe-rich heterogeneities during Neoarchean global mantle melting. *Geochimica et Cosmochimica Acta*, 185, 44–63.
- Morino, P., Caro, G., Reisberg, L., & Schumacher, A. (2017). Chemical stratification in the post-magma ocean Earth inferred from coupled 146,147 Sm–142,143 Nd systematics in ultramafic rocks of the Saglek block (3.25–3.9 Ga; northern Labrador, Canada). *Earth and Planetary Science Letters*, 463, 136–150.

- O'Neil, J., Carlson, R. W., Paquette, J. L., & Francis, D. (2012). Formation age and metamorphic history of the Nuvvuagittuq Greenstone Belt. *Precambrian Research*, 220, 23-44.
- O'Neil, J., & Carlson, R. W. (2017). Building Archean cratons from Hadean mafic crust. *Science*, 355(6330), 1199-1202.
- Percival, J. A., & Card, K. D. (1994). Geology of Lac Minto-Rivière aux Feuilles, Québec, Map1854A. *Geological Survey of Canada, Ottawa*.
- Percival, J. A., & Mortensen, J. K. (2002). Water-deficient calc-alkaline plutonic rocks of northeastern Superior Province, Canada: significance of charnockitic magmatism. *Journal of Petrology*, 43(9), 1617-1650.
- Peters, D. (2022). Iterative and time-resolved data reduction for short-lived Nd isotope data acquired by TIMS. *Personal communication*.
- Pin, C., & Zalduegui, J. S. (1997). Sequential separation of light rare-earth elements, thorium and uranium by miniaturized extraction chromatography: application to isotopic analyses of silicate rocks. *Analytica Chimica Acta*, 339(1-2), 79-89.
- Puchtel, I. S., Blichert-Toft, J., Touboul, M., & Walker, R. J. (2018). 182W and HSE constraints from 2.7 Ga komatiites on the heterogeneous nature of the Archean mantle. *Geochimica et Cosmochimica Acta*, 228, 1-26.
- Render, J., & Brennecka, G. A. (2021). Isotopic signatures as tools to reconstruct the primordial architecture of the Solar System. *Earth and Planetary Science Letters*, 555, 116705.
- Rizo, H., Boyet, M., Blichert-Toft, J., & Rosing, M. (2011). Combined Nd and Hf isotope evidence for deep-seated source of Isua lavas. *Earth and Planetary Science Letters*, 312(3-4), 267-279.
- Saji, N. S., Wielandt, D., Holst, J. C., & Bizzarro, M. (2020). Solar system Nd isotope heterogeneity: Insights into nucleosynthetic components and protoplanetary disk evolution. *Geochimica et Cosmochimica Acta*, 281, 135-148.
- Schulz K. J. (1982) Magnesian basalts from the Archean terrains of Minnesota. In Komatiites (eds. N. T. Arndt and E. G. Nisbet). *George Allen & Unwin*, London, pp. 171–186.
- Simard, M. (2008). Stratigraphie et géochronologie du nord-est de la Province du Supérieur. *Synthèse du Nord-Est de la Province du Supérieur. Ministère des Ressources naturelles, Québec*, 23-86.
- Stone, W. E., Crocket, J. H., Dickin, A. P., & Fleet, M. E. (1995). Origin of Archean ferropicrites: geochemical constraints from the Boston Creek Flow, Abitibi greenstone belt, Ontario, Canada. *Chemical Geology*, 121(1-4), 51-71.

- Sun, S. S., & McDonough, W. F. (1989). Chemical and isotopic systematics of oceanic basalts: implications for mantle composition and processes. *Geological Society, London, Special Publications*, 42(1), 313-345.
- Tanaka, T., Togashi, S., Kamioka, H., Amakawa, H., Kagami, H., Hamamoto, T., & Kunimaru, T. (2000). JNdi-1: a neodymium isotopic reference in consistency with LaJolla neodymium. *Chemical Geology*, 168(3-4), 279-281.
- Tuff, J., Takahashi, E., & Gibson, S. A. (2005). Experimental constraints on the role of garnet pyroxenite in the genesis of high-Fe mantle plume derived melts. *Journal of Petrology*, 46(10), 2023-2058.
- Walker, R. J. (2009). Highly siderophile elements in the Earth, Moon and Mars: update and implications for planetary accretion and differentiation. *Geochemistry*, 69(2), 101-125.
- Waterton, P., Mungall, J., & Pearson, D. G. (2021). The komatiite-mantle platinum-group element paradox. *Geochimica et Cosmochimica Acta*, 313, 214-242.
- Wilson, M. (1989). *Igneous Petrogenesis: A Global Tectonic Approach*. Unwin Hyman. London.
- Wilson S.A. (1997). Data compilation for USGS reference material BHVO-2, Hawaiian Basalt, U.S. *Geological Survey Open-File Report*.
- Wilson S.A. (1998). Data compilation for USGS reference material GSP-2, Granodiorite, Silver Plume, Colorado, U.S. *Geological Survey Open-File Report*.
- Van Kranendonk M. J., Altermann W., Beard B. L., Hoffman P. F., Johnson C. M., Kasting J. F., Melezhik V. A., Nutman A.P., Papineau D. and Pirajno F. (2012). *The Geologic Time Scale 2012 2-Volume Set*. Elsevier.
- Vermeesch, P. (2018). IsoplotR: A free and open toolbox for geochronology. *Geoscience Frontiers*, 9(5), 1479-1493.
- Zhang, J., Liu, Y., Ling, W., & Gao, S. (2017). Pressure-dependent compatibility of iron in garnet: Insights into the origin of ferropicritic melt. *Geochimica et Cosmochimica Acta*, 197, 356-377.

Appendix A

Table A1: Sample numbers, lithologies, and GPS coordinates.

Sample	Lithology	UTM Zone	Easting	Northing
QK-001	Websterite	18V	359171	6460745
QK-002	Websterite	18V	359211	6460756
QK-003	Websterite	18V	359188	6460763
QK-004	Peridotite	18V	359152	6460831
QK-005	Gabbronorite	18V	359141	6460821
QK-006	Gabbronorite	18V	359140	6460805
QK-007	Websterite	18V	359154	6460801
QK-008	Websterite	18V	359162	6460798
QK-009	Peridotite	18V	359177	6460799
QK-010	Harzburgite	18V	359181	6460800
QK-011	Peridotite	18V	359197	6460808
QK-012	Websterite	18V	359174	6460790
QK-013	Harzburgite	18V	359185	6460786
QK-014	Websterite	18V	359150	6460757
QK-015	Granodiorite	18V	359132	6460804
QK-016	Peridotite	18V	359212	6460793
QK-017	Gabbronorite	18V	359345	6460591
QK-018	Granodiorite	18V	359347	6460597
QK-019	Websterite	18V	359294	6460576
QK-020	Websterite	18V	359305	6460585
QK-021	Websterite	18V	359326	6460596
QK-022	Websterite	18V	359330	6460599
QK-023	Websterite	18V	359475	6460415
QK-024	Gabbronorite	18V	359431	6460494

Table A2: Comparison of average measured values for mafic standard BHVO-2 to the certified standard values (Wilson, 1997).

Element (wt%)	Measured BHVO-2 values (\bar{x})	$\pm 2SE$	Certified BHVO-2 values	Accuracy (wt %)
Na ₂ O	2.25	0.02	2.22	1.13
MgO	7.17	0.14	7.22	0.64
Al ₂ O ₃	13.5	0.02	13.5	0.01
SiO ₂	49.4	0.06	49.9	1.02
P ₂ O ₅	0.28	0.01	0.27	2.10
K ₂ O	0.51	0.01	0.52	2.24
CaO	11.3	0.03	11.4	0.93
TiO ₂	2.72	0.02	2.60	4.55
Fe ₂ O ₃	12.2	0.05	12.3	0.59

Table A3: Comparison of measured values for felsic standard GSP-2 to the certified standard values (Wilson, 1997).

Element (wt. %)	Measured GSP-2 values	Certified GSP-2 values	Accuracy (Wt %)
Na₂O	2.71	2.78	2.66
MgO	0.97	0.96	0.83
Al₂O₃	14.9	14.9	0.06
SiO₂	66.8	66.6	0.26
P₂O₅	0.29	0.29	0.69
K₂O	5.44	5.39	0.85
CaO	2.13	2.10	1.29
TiO₂	0.58	0.66	12.7
Fe₂O₃	4.92	4.90	0.41

Table A4: Analytical results for standards BHVO-2, BCR-2, BIR-1A and GSP-2

	BHVO-2	BCR-2				BIR-1a				GSP-2			
	$\pm 2SD$ (ppm)	Certified Value (ppm)	Average (ppm)	$\pm 2SD$	Relative Error (%)	Certified Value (ppm)	Average (ppm)	$\pm 2SD$	Relative Error (%)	Certified Value (ppm)	Average (ppm)	$\pm 2SD$	Relative Error (%)
Sc	2	33.5	34.2	3	2	43.2	43.2	4	<1	6.20	6.76	3	9
Ti	5	13579	13933	3	3	5747	6482	4	13	4157	4085	3	2
Cr	6	15.9	14.9	5	6	393	390	3	1	23.0	20.9	5	9
Ni	4	12.6	11.9	5	6	169	175	4	3	17.0	17.0	5	<1
Sr	1	337	345	4	2	109	110	4	1	259	238	4	8
Y	2	36.1	36.7	4	2	15.6	15.6	2	<1	28.0	26.9	4	4
Zr	1	187	190	2	2	14.8	14.0	2	6	550	576	2	5
Nb	2	12.4	12.6	3	1	0.553	0.743	5	34	27.0	26.5	3	2
La	2	25.1	25.7	4	3	0.627	0.601	2	4	197	196	4	1
Ce	2	53.1	54.7	4	3	1.92	1.89	3	1	498	462	4	7
Pr	2	6.83	7.02	4	3	0.372	0.370	2	1	60.0	59.4	4	1
Nd	2	28.3	29.1	3	3	2.40	2.34	2	2	224	209	3	7
Sm	2	6.55	6.65	5	2	1.11	1.09	3	2	27.0	26.4	5	2
Eu	1	1.99	2.14	2	7	0.520	0.510	3	2	2.40	2.61	2	9
Gd	2	6.81	7.05	2	4	1.81	1.79	3	1	12.2	14.5	2	19
Tb	6	1.08	1.09	4	1	0.362	0.363	8	<1	1.40	1.44	4	3
Dy	1	6.42	6.46	4	1	2.54	2.54	5	<1	6.00	5.90	4	2
Ho	4	1.31	1.32	5	1	0.572	0.575	3	1	0.990	0.968	5	2
Er	7	3.67	3.75	7	2	1.68	1.74	7	3	2.50	2.51	7	1
Tm	4	0.534	0.535	2	<1	0.256	0.251	4	2	0.310	0.290	2	6
Yb	4	3.39	3.38	4	<1	1.63	1.61	3	1	1.77	1.73	4	3
Lu	3	0.505	0.506	1	<1	0.248	0.246	3	1	0.250	0.236	1	6
Hf	2	4.97	5.03	3	1	0.582	0.593	1	2	14.0	14.9	3	6
Ta	3	0.785	0.775	4	1	0.0414	0.0526	5	27	0.875	0.855	4	2
Pb	5	10.6	11.4	4	8	3.04	3.51	4	15	44.0	54.6	4	24
Th	5	5.83	6.07	4	4	0.0328	0.0297	7	9	121	114	4	6
U	3	1.68	1.69	5	1	0.0105	0.0100	9	5	2.78	2.46	5	11

BHVO-2, BCR-2, BIR-1A certified values from Jochum et al. (2016) and GSP-2 certified values from Wilson (1998)

Table A5: Column chromatography procedure for the separation of REE for ^{147}Sm - ^{143}Nd and ^{142}Nd analysis using 10 mL Bio-Rad columns filled with 2mL 200-400 mesh AG50W-X8 cation exchange resin.

Acid	Volume	Description
2N HCl	2 x 10 mL	Conditioning
2N HCl	2 mL	Load Sample
2N HCl	2 x 1 mL	Rinse
2N HCl	2 x 8 mL	Discard
2.5N HCl	10 mL	Discard
6N HCl	10 mL	Collect REE
6N HCl	2 x 10 mL	Resin cleaning
H ₂ O	10 mL	Resin cleaning
6N HCl	10 mL	Resin cleaning
H ₂ O	10 mL	Resin Cleaning

Table A6: Column chromatography procedure for the separation of Sm and Nd for ^{147}Sm - ^{143}Nd analysis using 5 cm long x 5 mm diameter quartz columns filled with 300 mg 50-100 μm LN-spec resin.

Acid	Volume	Description
0.2N HCl	3 mL	Conditioning
0.2N HCl	0.25 mL	Load Sample
0.2N HCl	0.25 mL	Rinse
0.2N HCl	4.5 mL	Discard
0.2N HCl	5.5 mL	Collect Nd
0.5N HCl	1.25 mL	Rinse
0.5N HCl	2.5 mL	Collect Sm
6N HCl	10 mL	Resin Cleaning
0.2N HCl	6 mL	Resin Cleaning

Table A7: Nd yields for both analytical sessions

Sample	Session 1			Session 2		
	Theoretical Nd (ng)	Measured Nd (ng)	Yield %	Theoretical Nd (ng)	Measured Nd (ng)	Yield %
QK-003	661	214	32	786	511	65
QK-004	740	238	32	704	534	76
QK-005	817	280	34	705	641	91
QK-006	748	462	62	703	660	94
QK-008	671	398	59	703	521	74
QK-010	784	611	78	725	559	77
QK-012	1120	214	19	722	546	76
QK-013	702	159	23	703	554	79
QK-015	388	129	33	741	812	110
QK-016	717	71	10	719	174	24
QK-017	809	831	103	715	605	85
QK-018	502	114	23	775	435	56
QK-021	685	151	22	707	435	61
QK-023	674	98	15	723	513	71
QK-024	1127	183	16	704	636	90

Due the poor yields, only QK-006, QK-010, and QK-017 were analyzed for ^{142}Nd from the first session. During the second session all samples were analyzed.

Table A8: Modified column chromatography procedure for the separation of REE for the second ^{142}Nd analytical session using 10 mL Bio-Rad columns filled with 2mL 200-400 mesh AG50W-X8 cation exchange resin.

Acid	Volume	Description
2N HCl	10 mL	Conditioning
2N HCl	5 mL	Conditioning
2.5N HCl	2 mL	Load Sample
2.5N HCl	1 mL	Rinse
2.5N HCl	4 mL	Discard
2.5N HCl	9 mL	Discard
6N HCl	2 x 6 mL	Collect REE
6N HCl	2 x 10 mL	Resin cleaning
H ₂ O	10 mL	Resin cleaning
6N HCl	10 mL	Resin cleaning
H ₂ O	10 mL	Resin Cleaning

Table A9: Column chromatography procedure for the removal of Ce for ¹⁴²Nd analysis using 0.5 mL of 100-150 μm LN-spec resin in polyethylene columns made from 10 mL disposable pipettes.

Acid	Volume	Description
H ₂ O	1 reservoir	Resin Cleaning
0.5N HCl	1 reservoir	Resin Cleaning
H ₂ O	1 reservoir	Resin Cleaning
10N HNO ₃	2 mL	Resin Cleaning
10N HNO ₃	2 mL	Resin Cleaning
10N HNO ₃	2 mL	Resin Cleaning
10N HNO ₃ + 20mM NaBrO ₃	2 mL	Conditioning
10N HNO₃ + 20mM NaBrO₃	0.1 mL	Load & Collect
10N HNO₃ + 20mM NaBrO₃	1 mL	Elute & Collect
10N HNO₃ + 20mM NaBrO₃	5 mL	Elute & Collect
Dry sample		
H ₂ O	2 mL	Resin Cleaning
0.5N HCl	1 reservoir	Resin Cleaning
H ₂ O	1 reservoir	Resin Cleaning
10N HNO ₃	2 mL	Resin Cleaning
10N HNO ₃	2 mL	Resin Cleaning
10N HNO ₃	2 mL	Resin Cleaning
10N HNO ₃ + 20mM NaBrO ₃	2 mL	Conditioning
10N HNO₃ + 20mM NaBrO₃	0.4mL	Load & Collect
10N HNO₃ + 20mM NaBrO₃	1 mL	Elute & Collect
10N HNO₃ + 20mM NaBrO₃	5 mL	Elute & Collect
H ₂ O	2 mL	Resin Cleaning
6N HCl	5 mL	Resin Cleaning
0.2N HCl	2 mL	Resin Cleaning

Table A10: Column chromatography procedure for the removal of Na and Br for ¹⁴²Nd analysis using 10 mL Bio-Rad columns filled with 2mL 200-400 mesh AG50W-X8 cation exchange resin columns.

Acid	Volume	Description
2.5N HCl	10 mL	Conditioning
2.5N HCl	1 mL	Load
2.5N HCl	1 mL	Rinse
2.5N HCl	4mL	Rinse
2.5N HCl	9 mL	Rinse
6N HCl	6 mL	Collect Nd
6N HCl	6 mL	Collect Nd
6N HCl	1 reservoir	Resin Cleaning
6N HCl	1 reservoir	Resin Cleaning
H ₂ O	1 reservoir	Resin Cleaning
6N HCl	1 reservoir	Resin Cleaning

Table A11: Column chromatography procedure used in the first session for the removal of Sm for ^{142}Nd analysis using 20-50 μm LN-spec resin in Teflon columns (12 cm length, 0.4 cm diameter)

Acid	Volume	Description
0.2N HCl	3 mL	Conditioning
0.2N HCl	50 μL	Load
0.2N HCl	100 μL	Rinse
0.2N HCl	100 μL	Rinse
0.2N HCl	11 mL	Rinse
0.2N HCl	9 mL	Collect Nd
6N HCl	10 mL	Resin Cleaning
6N HCl	10 mL	Resin Cleaning
0.2N HCl	3 mL	Resin Cleaning

Table A12: Column chromatography procedure used in the second session for the removal of Sm for ^{142}Nd analysis using 20-50 μm LN-spec resin in Teflon columns (14 cm length, 0.4 cm diameter)

Acid	Volume	Description
0.2N HCl	3 mL	Conditioning
0.2N HCl	50 μL	Load
0.2N HCl	100 μL	Rinse
0.2N HCl	100 μL	Rinse
0.2N HCl	8 mL	Rinse
0.2N HCl	12 mL	Collect Nd
6N HCl	10 mL	Resin Cleaning
6N HCl	10 mL	Resin Cleaning
0.2N HCl	3 mL	Resin Cleaning

Table A13: Summary of JNdi-1 analyses

Session	Sample	$^{140}\text{Ce}/^{144}\text{Nd}$	2SE	$^{147}\text{Sm}/^{144}\text{Nd}$	2SE	$^{142}\text{Nd}/^{144}\text{Nd}$	2SE	$\mu^{142}\text{Nd}$	$\pm 2\text{SE}$
1	Jndi-1	-0.000009	$\pm < 1$	-0.000001	$\pm < 1$	1.141831	± 4	-3.8	3.7
	Jndi-1	-0.000009	$\pm < 1$	0.000001	$\pm < 1$	1.141836	± 4	0.0	3.5
	Jndi-1	-0.000008	$\pm < 1$	0.000001	$\pm < 1$	1.141832	± 4	-2.7	3.6
	Jndi-1	-0.000004	± 1	0.000000	$\pm < 1$	1.141838	± 4	1.8	3.6
	Jndi-1	-0.000003	± 1	0.000000	$\pm < 1$	1.141838	± 4	2.3	3.6
	Jndi-1	-0.000006	$\pm < 1$	0.000000	$\pm < 1$	1.141831	± 4	-3.9	3.3
	Jndi-1	-0.000010	$\pm < 1$	0.000001	$\pm < 1$	1.141837	± 4	1.2	3.6
	Jndi-1	-0.000007	± 1	0.000000	$\pm < 1$	1.141836	± 4	0.7	3.6
	Jndi-1	-0.000004	± 1	-0.000001	$\pm < 1$	1.141841	± 4	4.4	3.5
		AVERAGE	-0.000007	± 2	0.000000	$\pm < 1$	1.141836	± 2	0.0
2	Jndi-1	-0.000010	$\pm < 1$	0.000000	$\pm < 1$	1.141837	± 4	1.5	3.2
	Jndi-1	-0.000010	$\pm < 1$	0.000000	$\pm < 1$	1.141832	± 4	-3.2	3.3
	Jndi-1	-0.000014	$\pm < 1$	0.000001	$\pm < 1$	1.141836	± 5	0.3	4.8
	Jndi-1	-0.000010	$\pm < 1$	0.000000	$\pm < 1$	1.141833	± 3	-2.3	3.0
	Jndi-1	-0.000012	$\pm < 1$	0.000001	$\pm < 1$	1.141837	± 6	1.7	5.6
	Jndi-1	-0.000010	$\pm < 1$	0.000000	$\pm < 1$	1.141838	± 4	2.5	3.4
	Jndi-1	-0.000009	$\pm < 1$	0.000000	$\pm < 1$	1.141834	± 4	-1.6	3.1
	Jndi-1	-0.000013	$\pm < 1$	0.000001	$\pm < 1$	1.141833	± 5	-1.8	4.1
		AVERAGE	-0.000011	± 1	0.000000	$\pm < 1$	1.141835	± 2	-0.4
3	Jndi-1	-0.000012	$\pm < 1$	0.000000	$\pm < 1$	1.141834	± 4	-1.2	3.6
	Jndi-1	-0.000005	$\pm < 1$	0.000000	$\pm < 1$	1.141836	± 3	0.1	3.0
	Jndi-1	-0.000011	$\pm < 1$	-0.000001	$\pm < 1$	1.141836	± 4	0.8	3.4
	Jndi-1	-0.000008	$\pm < 1$	0.000000	$\pm < 1$	1.141833	± 4	-2.1	3.6
	Jndi-1	-0.000013	$\pm < 1$	0.000000	$\pm < 1$	1.141836	± 5	0.8	4.1
	Jndi-1	-0.000013	$\pm < 1$	0.000001	$\pm < 1$	1.141837	± 6	1.6	5.0
		AVERAGE	-0.000010	± 2	0.000000	$\pm < 1$	1.141835	± 1	0.0

Table A13 Continued

Session	Sample	$^{145}\text{Nd}/^{144}\text{Nd}$	2SE	$\mu^{145}\text{Nd}$	$\pm 2\text{SE}$	$^{148}\text{Nd}/^{144}\text{Nd}$	2SE	$\mu^{148}\text{Nd}$	$\pm 2\text{SE}$	$^{150}\text{Nd}/^{144}\text{Nd}$	2SE	$\mu^{150}\text{Nd}$	$\pm 2\text{SE}$
1	Jndi-1	0.348408	± 1	-3.4	3.6	0.2415851	± 1	14.9	6.0	0.236460	± 2	31.3	8.2
	Jndi-1	0.348408	± 1	-1.4	3.6	0.2415781	± 2	-14.4	6.3	0.236449	± 2	-16.5	8.1
	Jndi-1	0.348408	± 1	-2.5	3.7	0.2415774	± 2	-17.0	6.4	0.236447	± 2	-21.5	8.4
	Jndi-1	0.348409	± 1	1.3	3.8	0.2415795	± 1	-8.5	6.1	0.236450	± 2	-10.8	8.8
	Jndi-1	0.348408	± 1	-2.3	3.4	0.2415758	± 1	-23.8	5.8	0.236441	± 2	-48.3	7.6
	Jndi-1	0.348408	± 1	-3.3	3.1	0.2415801	± 1	-5.9	5.9	0.236449	± 2	-14.6	7.8
	Jndi-1	0.348407	± 1	-4.6	3.4	0.2415865	± 1	20.5	6.1	0.236463	± 2	45.2	8.1
	Jndi-1	0.348405	± 1	-11.1	3.6	0.2415875	± 1	24.8	6.1	0.236466	± 2	55.3	8.2
	Jndi-1	0.348405	± 1	-12.1	3.3	0.2415901	± 1	35.6	6.0	0.236467	± 2	60.6	7.9
	AVERAGE	0.348409	± 2	0.0	20.1	0.2415815	± 3	0.0	43.5	0.236452	± 6	0.0	79.1
2	Jndi-1	0.348407	± 1	7.4	3.0	0.2415846	± 1	6.3	5.3	0.236469	± 2	20.5	7.1
	Jndi-1	0.348407	± 1	5.4	2.9	0.2415861	± 1	12.6	5.5	0.236468	± 2	19.3	7.5
	Jndi-1	0.348403	± 2	-4.0	5.0	0.2415831	± 2	-0.1	7.1	0.236463	± 3	-5.6	10.7
	Jndi-1	0.348403	± 1	-4.2	3.3	0.2415782	± 1	-20.4	5.6	0.236458	± 2	-24.7	7.9
	Jndi-1	0.348402	± 2	-8.5	5.8	0.2415821	± 2	-4.0	8.8	0.236463	± 3	-4.7	13.3
	Jndi-1	0.348406	± 1	3.8	3.1	0.2415835	± 1	1.7	5.3	0.236464	± 2	-1.7	7.9
	Jndi-1	0.348403	± 1	-5.5	3.1	0.2415801	± 1	-12.6	5.1	0.236463	± 2	-3.9	6.8
	Jndi-1	0.348404	± 1	-1.7	4.1	0.2415808	± 2	-9.7	7.7	0.236464	± 3	1.0	10.7
	AVERAGE	0.348405	± 1	-0.9	10.7	0.2415823	± 2	-3.3	20.0	0.236464	± 2	0.0	27.1
3	Jndi-1	0.348404	± 1	-1.5	3.5	0.2415826	± 2	-2.3	6.4	0.236466	± 2	7.4	8.9
	Jndi-1	0.348406	± 1	3.3	3.0	0.2415822	± 1	-3.8	5.3	0.236461	± 2	-13.6	7.5
	Jndi-1	0.348404	± 1	-2.2	3.7	0.2415834	± 2	1.4	6.3	0.236467	± 2	14.2	8.7
	Jndi-1	0.348406	± 1	2.6	3.5	0.2415819	± 2	-5.0	6.4	0.236461	± 2	-13.2	8.9
	Jndi-1	0.348404	± 1	-3.3	3.4	0.2415824	± 2	-3.0	6.4	0.236467	± 2	11.2	8.0
	Jndi-1	0.348406	± 2	2.8	4.5	0.2415835	± 2	1.5	8.1	0.236462	± 3	-6.6	11.0
	AVERAGE	0.348405	± 1	0.0	4.9	0.2415831	± 2	0.0	19.0	0.236464	± 3	0.0	36.9

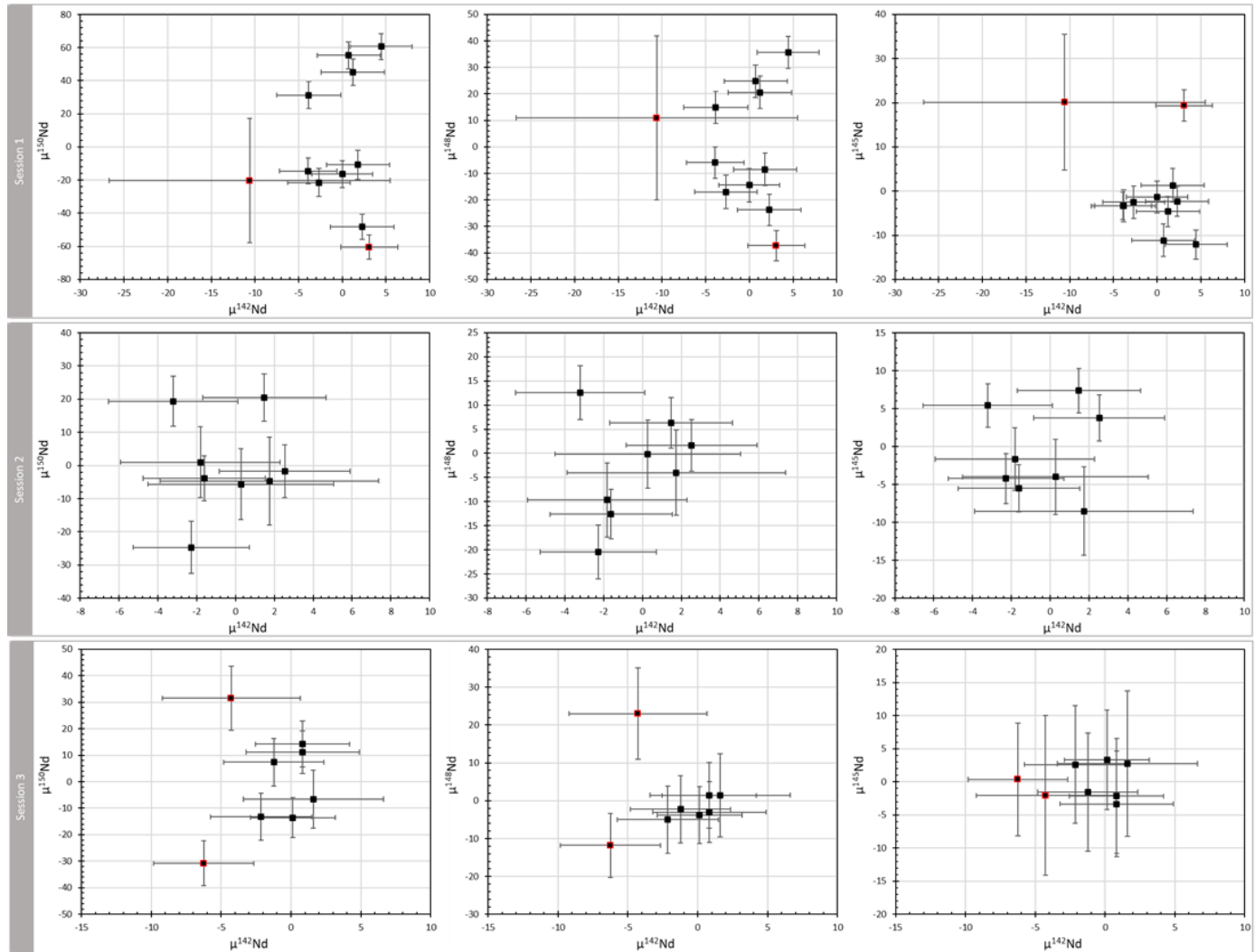


Figure A1: Comparison of $\mu^{142}\text{Nd}$ with $\mu^{150}\text{Nd}$, $\mu^{148}\text{Nd}$, and $\mu^{145}\text{Nd}$ of JNdi-1 standards. Samples outlined in red were considered deviant, and therefore excluded from the average calculations.

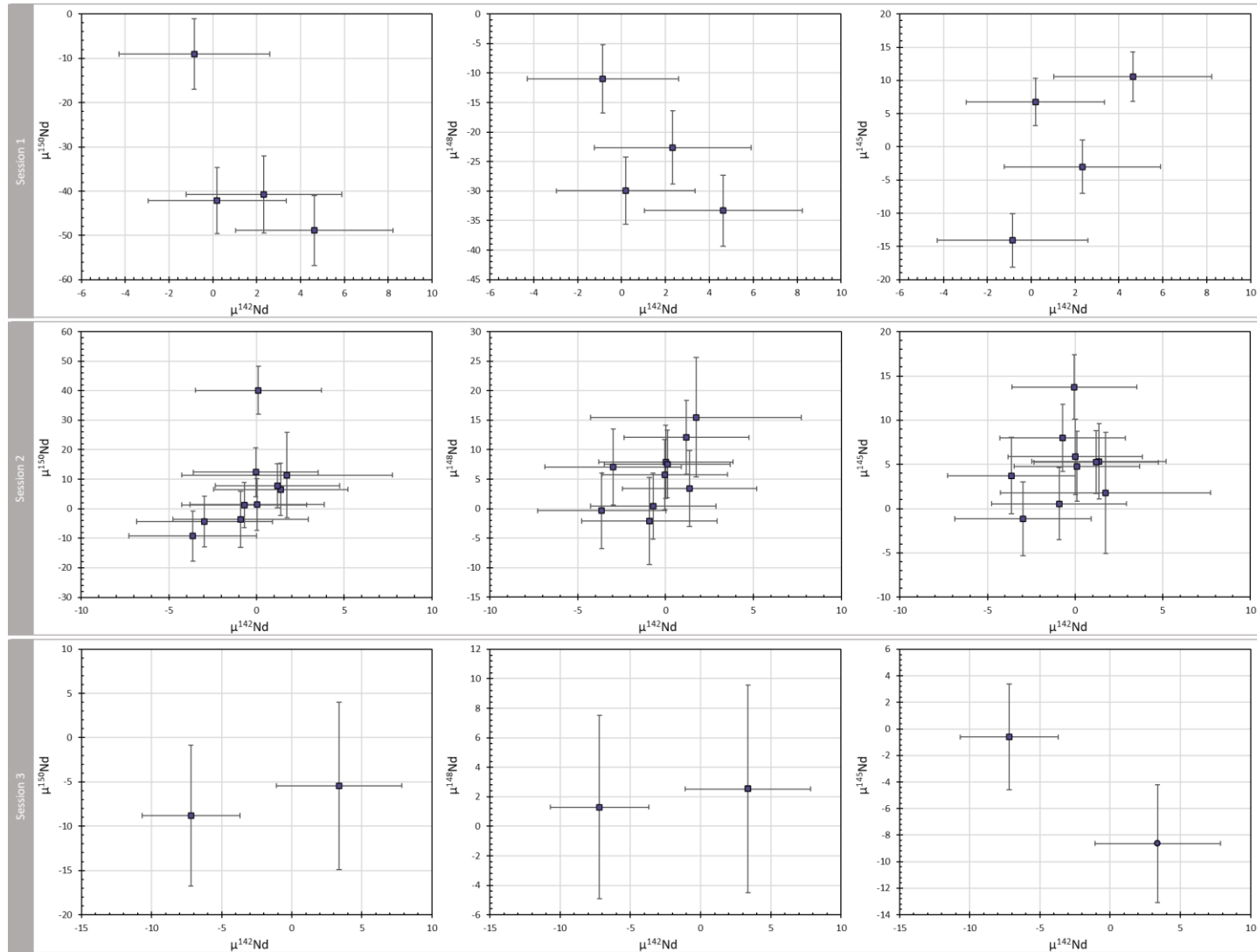


Figure A2: Comparison of $\mu^{142}\text{Nd}$ with $\mu^{150}\text{Nd}$, $\mu^{148}\text{Nd}$, and $\mu^{145}\text{Nd}$ of samples.

Appendix B

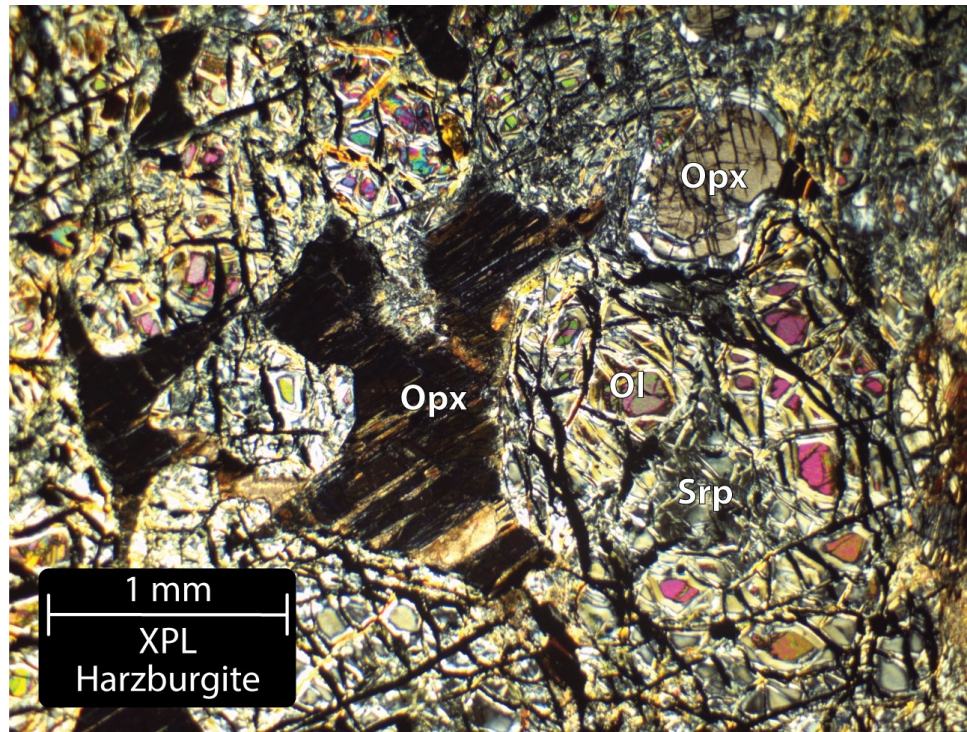


Figure B1: XPL photomicrograph of harzburgite QK-010. Magnification 2.5x.

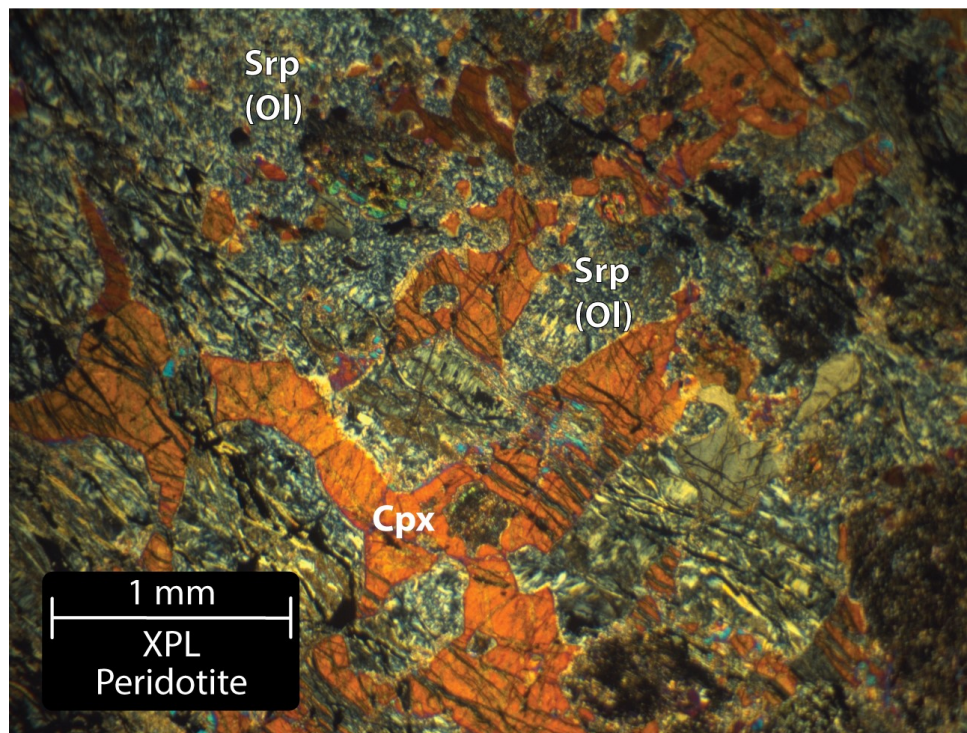


Figure B2: XPL photomicrograph of peridotite QK-016. Magnification 2.5x.

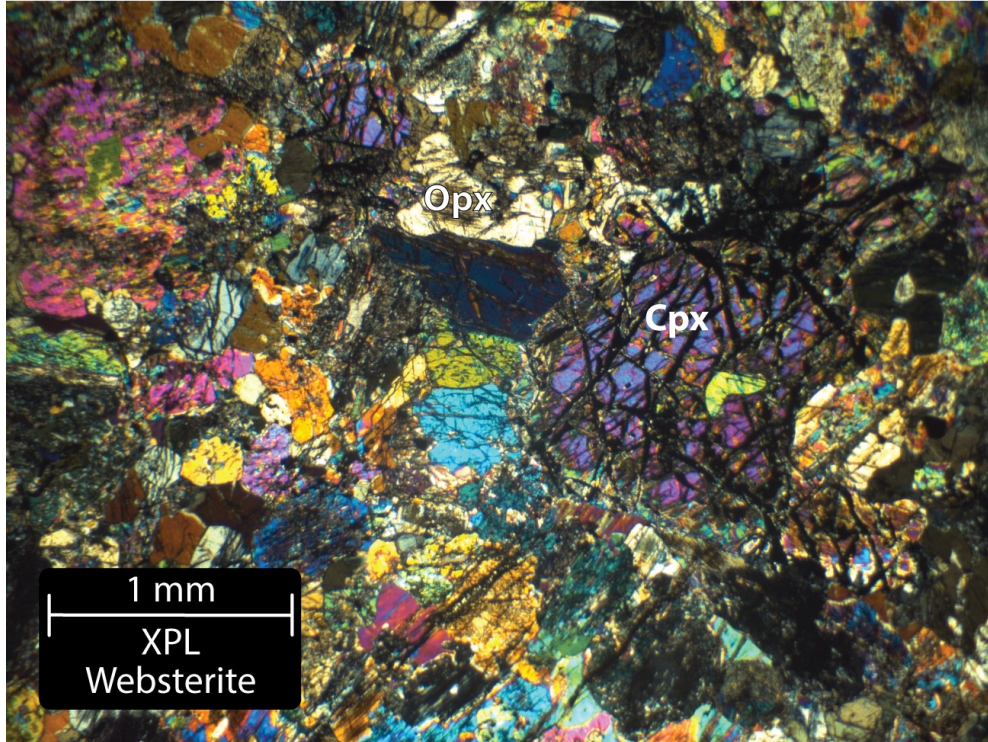


Figure B3: XPL photomicrograph of websterite QK-019. Magnification 2.5x.

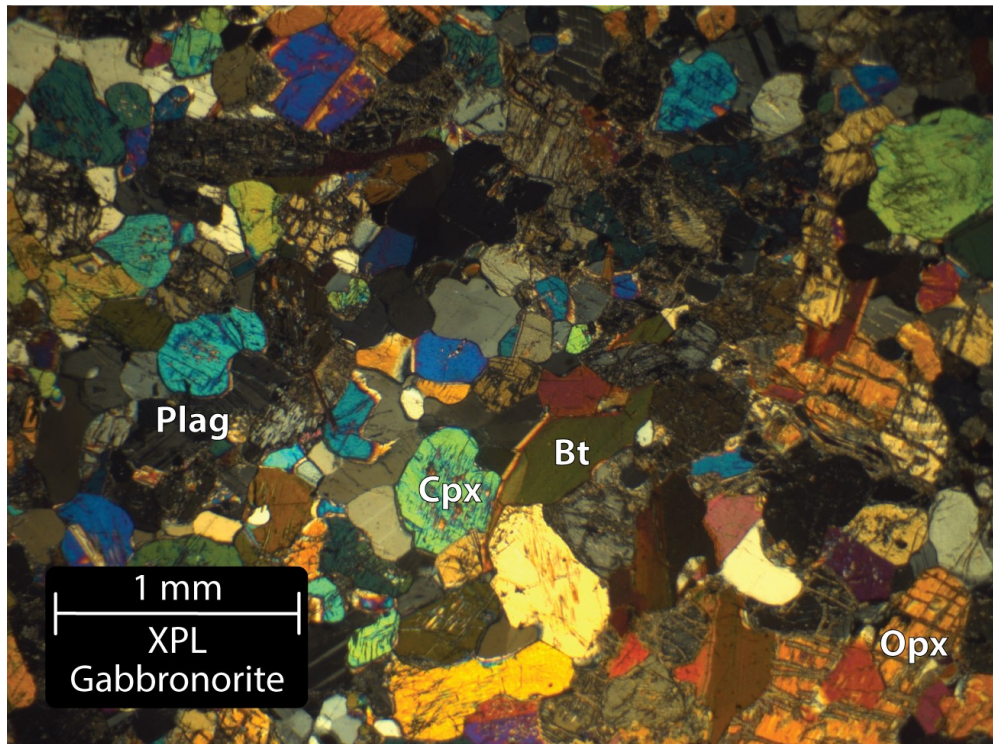


Figure B4: PPL (left) and XPL (right) photomicrograph of gabbronorite QK-024. Magnification 2.5x.

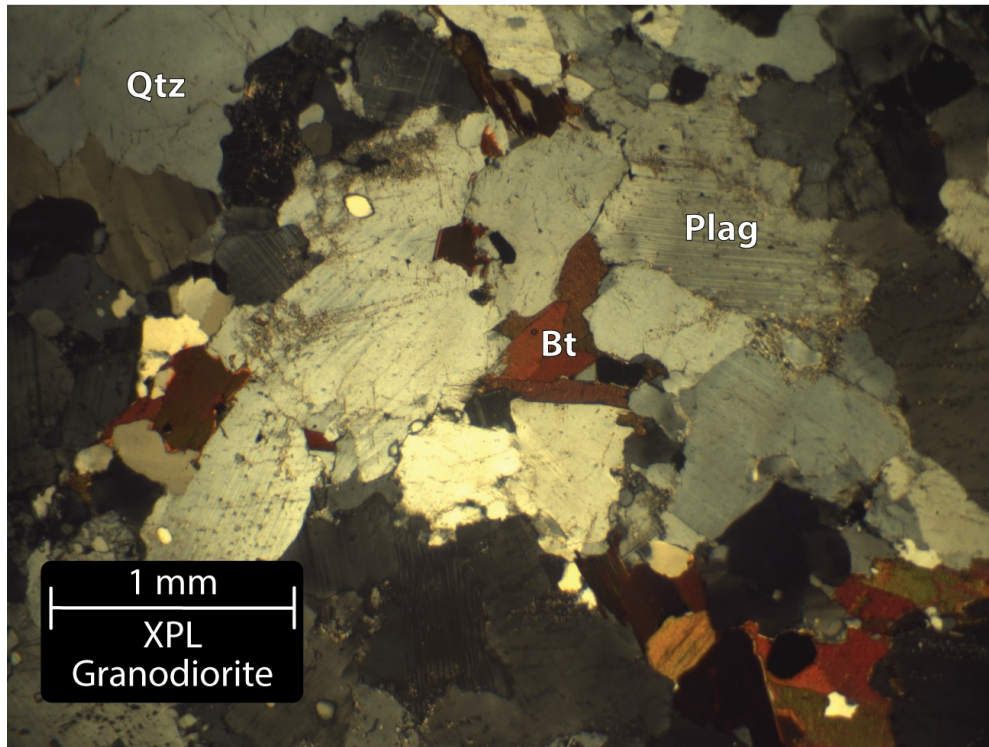


Figure B5: XPL photomicrograph of granodiorite QK-015. Magnification 5x.

Table B1: Major element oxide and trace element compositions of the Qullinaaraaluk intrusion

Sample Litho.	QK-001 <i>Web.</i>	QK-002 <i>Web.</i>	QK-003 <i>Web.</i>	QK-004 <i>Perid.</i>	QK-005 <i>Gabbron.</i>	QK-006 <i>Gabbron.</i>	QK-007 <i>Web.</i>
SiO₂ (wt%)	53.1	49.9	52.3	45.6	54.5	58.1	53.2
TiO₂	0.208	0.233	0.216	0.120	0.230	0.240	0.227
Al₂O₃	4.34	4.27	3.76	2.78	4.62	5.48	4.24
FeO*	8.0	10.5	8.6	13.4	8.5	8.0	8.4
MnO	0.172	0.179	0.178	0.143	0.149	0.134	0.179
MgO	19.3	23.0	20.1	34.8	18.9	16.3	19.2
CaO	13.7	11.1	14.1	2.6	11.4	9.2	13.7
Na₂O	0.966	0.657	0.535	0.344	1.044	1.244	0.675
K₂O	0.247	0.170	0.165	0.135	0.630	1.246	0.156
P₂O₅	0.034	0.039	0.022	0.028	0.047	0.044	0.023
LOI	1.66	3.65	0.55	10.08	2.26	1.17	0.79
Sc (ppm)	49.33	40.20	25.66	12.82	46.77	37.87	48.90
Ti	1190	1186	1200	593	1282	1372	2091
Cr	2169	1975	2173	1812	1490	1403	1697
Ni	470	1480	657	1134	401	542	380
Sr	95.3	83.9	44.9	57.7	83.7	91.5	89.1
Y	6.26	6.33	6.36	2.39	6.59	5.75	6.40
Zr	14.1	13.6	11.6	10.9	24.6	37.3	12.8
Nb	0.389	0.375	0.332	0.432	0.592	1.394	0.535
La	3.54	4.56	2.51	3.46	12.58	34.66	2.93
Ce	8.17	10.65	6.44	7.28	27.21	65.78	7.34
Pr	1.16	1.45	1.00	0.90	3.18	6.48	1.11
Nd	5.54	6.50	4.91	3.48	11.62	20.69	5.35
Sm	1.40	1.46	1.31	0.64	1.98	2.59	1.38
Eu	0.427	0.423	0.399	0.257	0.484	0.571	0.431
Gd	1.34	1.46	1.35	0.56	1.74	1.93	1.38
Tb	0.201	0.197	0.203	0.078	0.230	0.220	0.196
Dy	1.20	1.19	1.23	0.44	1.30	1.14	1.22
Ho	0.243	0.246	0.250	0.091	0.248	0.225	0.249
Er	0.659	0.648	0.677	0.255	0.676	0.559	0.690
Tm	0.094	0.091	0.097	0.036	0.097	0.084	0.100
Yb	0.573	0.594	0.604	0.245	0.595	0.518	0.616
Lu	0.088	0.085	0.090	0.038	0.090	0.081	0.089
Hf	0.461	0.464	0.437	0.335	0.831	1.185	0.451
Ta	0.021	0.021	0.015	0.022	0.025	0.037	0.028
Pb	2.51	4.97	1.41	1.39	2.73	5.82	1.97
Th	0.413	0.417	0.261	0.397	1.161	5.114	0.199
U	0.072	0.057	0.043	0.051	0.080	0.112	0.032

Table 5: Continued

Sample Litho.	QK-009 <i>Perid.</i>	QK-010 <i>Harz.</i>	QK-011 <i>Perid.</i>	QK-012 <i>Web.</i>	QK-013 <i>Harz.</i>	QK-014 <i>Web.</i>	QK-015 <i>Granodi.</i>
SiO₂ (wt%)	43.4	43.1	46.7	51.5	43.5	53.0	68.7
TiO₂	0.069	0.119	0.169	0.198	0.144	0.201	0.195
Al₂O₃	2.14	3.12	3.27	3.50	3.11	3.48	17.39
FeO*	18.8	14.8	12.3	8.9	15.0	8.2	1.9
MnO	0.290	0.164	0.152	0.182	0.182	0.181	0.024
MgO	32.4	36.2	30.2	20.8	35.4	19.4	0.9
CaO	2.5	2.0	6.5	14.4	2.1	14.7	4.0
Na₂O	0.270	0.293	0.459	0.481	0.301	0.530	4.953
K₂O	0.163	0.180	0.155	0.082	0.285	0.157	1.880
P₂O₅	0.037	0.041	0.024	0.030	0.041	0.012	0.026
LOI	10.07	9.27	7.80	0.72	7.01	2.00	0.84
Sc (ppm)	9.84	8.42	25.17	39.31	10.79	30.61	3.04
Ti	375	603	983	1115	746	1154	1409
Cr	818	1473	1969	1956	1630	2419	16
Ni	1135	1104	945	620	1184	383	16
Sr	63.3	62.5	53.0	70.1	68.0	42.7	530.0
Y	1.46	2.42	4.23	5.98	2.62	6.43	2.14
Zr	7.9	12.4	13.1	9.8	10.0	9.2	81.7
Nb	0.410	0.470	0.380	0.225	0.440	0.195	2.268
La	3.85	3.83	3.19	2.36	4.72	3.62	23.93
Ce	7.28	7.58	7.14	6.08	8.45	10.37	39.44
Pr	0.81	0.90	0.98	0.97	0.94	1.50	3.74
Nd	2.70	3.54	4.41	4.85	3.54	6.58	11.43
Sm	0.40	0.68	1.00	1.29	0.61	1.55	1.33
Eu	0.142	0.206	0.330	0.392	0.197	0.404	1.018
Gd	0.36	0.53	0.89	1.29	0.62	1.47	0.95
Tb	0.056	0.074	0.137	0.198	0.092	0.220	0.095
Dy	0.27	0.44	0.83	1.22	0.49	1.25	0.43
Ho	0.052	0.089	0.168	0.251	0.095	0.247	0.072
Er	0.146	0.234	0.449	0.632	0.270	0.716	0.213
Tm	0.023	0.038	0.064	0.097	0.039	0.099	0.025
Yb	0.163	0.247	0.395	0.564	0.271	0.610	0.165
Lu	0.023	0.038	0.062	0.081	0.042	0.093	0.026
Hf	0.213	0.335	0.428	0.370	0.300	0.370	2.304
Ta	0.023	0.023	0.022	0.012	0.020	0.009	0.067
Pb	5.72	2.41	2.11	1.88	2.56	0.85	13.93
Th	0.426	0.525	0.507	0.232	0.666	0.187	2.174
U	0.076	0.085	0.068	0.046	0.172	0.097	0.172

Table 5: Continued

Sample Litho.	QK-016 <i>Perid.</i>	QK-017 <i>Gabbron.</i>	QK-018 <i>Granodi.</i>	QK-019 <i>Web.</i>	QK-020 <i>Web.</i>	QK-021 <i>Web.</i>	QK-022 <i>Web.</i>
SiO₂ (wt%)	46.9	57.0	71.0	49.4	53.1	51.2	52.4
TiO₂	0.165	0.290	0.246	0.163	0.180	0.183	0.291
Al₂O₃	3.14	4.81	15.69	3.22	3.47	3.62	5.42
FeO*	14.9	8.8	2.3	9.6	8.3	11.9	8.2
MnO	0.234	0.161	0.018	0.174	0.172	0.196	0.170
MgO	29.3	17.9	1.0	23.7	20.5	23.9	16.8
CaO	4.9	9.0	3.7	13.2	13.5	8.5	15.5
Na₂O	0.380	1.069	4.255	0.464	0.501	0.432	0.969
K₂O	0.122	0.881	1.781	0.089	0.142	0.133	0.290
P₂O₅	0.020	0.056	0.073	0.028	0.023	0.025	0.037
LOI	8.38	1.51	0.96	3.49	2.36	2.92	2.06
Sc (ppm)	20.70	33.81	3.04	20.99	31.28	21.64	30.66
Ti	888	1672	1789	842	936	911	1660
Cr	1463	928	12	3367	2880	2573	2233
Ni	1813	382	9	586	787	1928	426
Sr	58.8	71.9	451.0	70.5	54.3	55.0	127.8
Y	4.07	8.35	1.64	4.53	4.81	4.00	8.52
Zr	11.6	87.8	118.3	10.4	9.1	8.4	20.3
Nb	0.356	2.261	1.838	0.229	0.196	0.249	0.480
La	2.79	28.60	47.77	2.24	1.95	1.86	4.42
Ce	6.45	59.44	79.96	5.45	4.84	4.37	10.70
Pr	0.90	6.59	7.21	0.80	0.75	0.65	1.59
Nd	4.11	23.08	21.27	3.92	3.77	3.13	7.62
Sm	0.93	3.41	2.05	0.96	1.00	0.78	1.88
Eu	0.272	0.571	1.078	0.324	0.315	0.256	0.611
Gd	0.86	2.43	1.24	1.00	1.00	0.80	1.80
Tb	0.131	0.294	0.101	0.136	0.136	0.120	0.260
Dy	0.76	1.64	0.37	0.84	0.92	0.74	1.64
Ho	0.150	0.306	0.064	0.172	0.186	0.156	0.334
Er	0.423	0.831	0.184	0.460	0.504	0.409	0.911
Tm	0.061	0.121	0.019	0.070	0.072	0.064	0.127
Yb	0.375	0.767	0.134	0.394	0.481	0.422	0.821
Lu	0.057	0.114	0.020	0.063	0.068	0.062	0.119
Hf	0.333	2.447	2.813	0.338	0.311	0.285	0.692
Ta	0.019	0.069	0.036	0.014	0.011	0.013	0.030
Pb	2.33	4.68	13.18	1.29	1.49	3.24	2.90
Th	0.205	4.184	6.110	0.205	0.110	0.167	0.402
U	0.041	0.143	0.165	0.029	0.016	0.054	0.072

Table 5 Continued

Sample Litho.	QK-023 Web.	QK-024 Gabbron.
SiO₂ (wt%)	50.6	55.5
TiO₂	0.190	0.266
Al₂O₃	3.68	6.07
FeO*	10.4	8.3
MnO	0.180	0.157
MgO	22.7	15.1
CaO	11.7	12.1
Na₂O	0.394	1.618
K₂O	0.101	0.798
P₂O₅	0.016	0.026
LOI	1.78	0.84
Sc (ppm)	26.96	20.05
Ti	1043	1521
Cr	1755	1490
Ni	759	217
Sr	48.6	89.7
Y	5.21	7.81
Zr	10.7	39.4
Nb	0.200	1.309
La	2.01	13.40
Ce	5.25	32.65
Pr	0.83	4.00
Nd	4.12	14.22
Sm	1.07	2.33
Eu	0.353	0.569
Gd	1.11	1.91
Tb	0.155	0.255
Dy	1.01	1.58
Ho	0.207	0.309
Er	0.526	0.787
Tm	0.082	0.119
Yb	0.519	0.744
Lu	0.075	0.107
Hf	0.387	1.434
Ta	0.010	0.043
Pb	0.91	3.76
Th	0.239	0.631
U	0.035	0.069

Table B3: Nd concentration and Isotopic Composition of tonalite 2003031499 analyzed by O'Neil and Carlson (2017)

Sample	2003031499
Litho	<i>Tonalite</i>
Easting	407561
Northing	6585298
Nd (ppm)	5.60
¹⁴⁷ Sm/ ¹⁴⁴ Sm	0.1047
¹⁴³ Nd/ ¹⁴⁴ Nd	0.510306 ± 4
¹⁴³ Nd/ ¹⁴⁴ Nd ₂₇₀₆	0.508381